

# Development and Application of a III-V Surface Electron Microscope

---

Changxi Zheng  
BSc, MEng



School of Physics, Monash University

November 26, 2012



## Notice 1

*Under the Copyright Act 1968, this thesis must be used only under the normal conditions of scholarly fair dealing. In particular no results or conclusions should be extracted from it, nor should it be copied or closely paraphrased in whole or in part without the written consent of the author. Proper written acknowledgement should be made for any assistance obtained from this thesis.*

## Notice 2

*I certify that I have made all reasonable efforts to secure copyright permissions for third-party content included in this thesis and have not knowingly added copyright content to my work without the owner's permission.*

---

# Contents

<b>Contents</b>	<b>ii</b>
<b>Abstract</b>	<b>iii</b>
<b>General Declaration</b>	<b>iv</b>
<b>Acknowledgements</b>	<b>vii</b>
<b>1 Introduction and overview</b>	<b>1</b>
1.1 Growth and applications of GaAs	1
1.2 Motivation for the development of III-V LEEM	4
1.3 III-V LEEM	5
1.4 Understanding MEM image contrast in the III-V LEEM	8
1.5 Applications of III-V LEEM	10
<b>2 Ga droplet surface dynamics during Langmuir evaporation of GaAs</b>	<b>13</b>
<b>3 Laplacian image contrast in mirror electron microscopy</b>	<b>33</b>
<b>4 Caustic imaging of gallium droplets using mirror electron microscopy</b>	<b>57</b>
<b>5 Electron caustic lithography</b>	<b>83</b>
<b>6 Congruent evaporation temperature of GaAs(001) controlled by As flux</b>	<b>97</b>
<b>7 Asymmetric coalescence of reactively wetting droplets</b>	<b>109</b>
<b>8 Relief of surface stress at steps during displacive adsorption of As on Si(111)</b>	<b>121</b>
<b>9 Conclusions and future work</b>	<b>135</b>
<b>Bibliography</b>	<b>137</b>

---

## Abstract

GaAs based communication and optoelectronic devices are widely used in our daily lives. Applications range from mobile phones and satellite communications to laser pointers, printers, barcode readers and DVD players. The components making up these devices are composed of thin layers of III-V semiconductor material, the thicknesses of which must be finely controlled. This is achieved by growing such layers via molecular beam epitaxy (MBE) with atomic layer precision. In addition to current technologies, the long-term research objective in III-V materials is to utilise variants of MBE to fabricate new quantum structures of nanoscale dimensions for new device applications. However, despite this current and future technological importance, the real-space imaging of III-V MBE surface growth dynamics is restricted by the presence of large incident As flux which restricts the use of conventional imaging techniques. To address this issue, the main goal of this thesis is therefore to develop a unique surface electron microscope to study the surface dynamics of III-V materials in real-time during MBE growth.

The thesis begins with the design and development of a III-V low energy electron microscope (LEEM). The incorporation of III-V MBE and a high As flux, in particular, required numerous modifications to a commercial LEEM instrument (Elmitec LEEM III). These are described in detail in Chapter 2.

Following the development of the LEEM it is important to understand the contrast associated with quantum structure formation. With this in mind, theories of mirror electron microscopy (MEM) were developed and experimentally verified using Ga droplets and their associated surface trails as convenient test objects. This work resulted in the development of the Laplacian and caustic theories of MEM imaging which is fully described in Chapters 3, 4 and 5.

Finally, based on the advances in instrumental development and imaging, proof-of-principle applications were undertaken to confirm that III-V and other materials could be investigated under high As flux. These included the control of the GaAs (001) congruent evaporation temperature by As flux (Chapter 6), the asymmetric coalescence of Ga droplets during Langmuir evaporation (Chapter 7), and the dynamic behaviour of As on Si(111) at high temperatures (Chapter 8).

---

## General Declaration

## PART A: General Declaration

Monash University  
Monash Research Graduate School

**Declaration for thesis based or partially based on conjointly published or unpublished work**

### General Declaration

In accordance with Monash University Doctorate Regulation 17/ Doctor of Philosophy and Master of Philosophy (MPhil) regulations the following declarations are made:

I hereby declare that this thesis contains no material which has been accepted for the award of any other degree or diploma at any university or equivalent institution and that, to the best of my knowledge and belief, this thesis contains no material previously published or written by another person, except where due reference is made in the text of the thesis.

This thesis includes eight original papers published in peer reviewed journals. The core theme of the thesis is developing and applying a unique III-V surface electron microscopy. The ideas, development and writing up of all the papers in the thesis were the principal responsibility of myself, the candidate, working within the School of Physics, Monash University under the supervision of David Jesson and Wenxin Tang.

The inclusion of co-authors reflects the fact that the work came from active collaboration between researchers and acknowledges input into team-based research.

In the case of chapters 2-8 my contribution to the work involved the following:

*[If this is a laboratory-based discipline, a paragraph outlining the assistance given during the experiments, the nature of the experiments and an attribution to the contributors could follow.]*

Thesis chapter	Publication title	Publication status*	Nature and extent of candidate's contribution
2	Ga droplet surface dynamics during Langmuir evaporation of GaAs	Published	Co-implementation and co-development of the III-V LEEM, co-performed the positioning nanostructures experiments, provided the technical expertise, co-wrote the paper
3	Laplacian image contrast in mirror electron microscopy	Published	Designed and performed the AFM and MEM experiments and co-wrote the paper
4	Caustic imaging of gallium droplets using mirror electron microscopy	Published	Designed and performed the AFM and MEM experiments and co-wrote the paper
5	Electron caustic lithography	Published	Designed and performed the FIB and MEM experiments, provided technical expertise and co-wrote the paper

6	Congruent evaporation temperature of GaAs(001) controlled by As flux	Published	Co-performed the experiments, co-wrote the paper
7	Asymmetric coalescence of reactively wetting droplets	Published	Designed and performed the experiments, co-developed the model used in the paper, and co-wrote the paper
8	Relief of surface stress at steps during displacive adsorption of As on Si(111)	Published	Designed and performed the experiments, co-developed the model used in the paper, co-wrote the paper

[ \* For example, 'published' / 'in press' / 'accepted' / 'returned for revision' ]

I have / have not (circle that which applies) renumbered sections of submitted or published papers in order to generate a consistent presentation within the thesis.

**Signed:** .....

**Date:** .....

---

## Acknowledgements

I gratefully appreciate the support and assistance of my supervisors Professor David Jesson and Dr. Wenxin Tang, whose profound knowledge, wisdom, inspiration and patience have made these past years at Monash highly rewarding. I am also grateful to them for helping me settle down in Melbourne.

I would like to acknowledge my colleague Mr. Zhenyu Zhou for his assistance in my project, his friendship and warm welcome to me in Melbourne. I appreciate Dr. Shane Kennedy's excellent theoretical contributions to microscopy image contrast, many useful discussions, and his help with my English. I acknowledge my collaborators Dr. Jing Fu and Dr. Wenhui Duan for their generous assistance with experiments and simulations. I would like to express my gratitude to Mr. Lin Qiu for his help in obtaining scanning electron microscopy images and his enthusiasm for inviting me and my wife to travel around Melbourne.

Also, many thanks to the staff and fellow postgraduate students in School of Physics. Especially, I would like to thank Mr. Rod Mackie for technical support, Mrs. Jean Pettigrew for her assistance with paper work, and Dr. Gary Ruben for his thesis template and help in Python programming.

Finally, I want to acknowledge the support and patience of my family, whose sacrifice, encouragement and love have made this project possible.



---

# Introduction and overview

## 1.1 Growth and applications of GaAs

### 1.1.1 Applications of GaAs

Gallium Arsenide (GaAs) is widely used in everyday applications ranging from satellite communications and cell phones to car collision warning radar and TV tuners. Compared with other semiconductor materials such as Si, GaAs has several superior properties. In particular, its direct bandgap allows it to be used to manufacture high efficiency lasers for DVD technology, barcode readers, printers and laser pointers. Furthermore, GaAs has a higher saturated electron velocity and a higher electron mobility which have led to the development of high frequency electronics for radar systems and microwave equipment. The fundamental components underlying these applications are composed of epilayers of III-V semiconductor materials on a GaAs(001) surface.

In addition to current technologies, there is a rising interest in the growth of novel structures such as quantum dots (QDs) and quantum rings (QRs) on GaAs(001) (Joyce and Vvedensky, 2004; Watanabe et al., 2000; Mano et al., 2005; Somaschini et al., 2009; Lee et al., 2009). These structures are regarded as promising building blocks for a new generation of electronics including quantum dot lasers. Additionally, quantum structures open up new possibilities for investigating fundamental physics like the Aharonov-Bohm effect (Fuhrer et al., 2001; Bayer et al., 2003; Fomin et al., 2007) and the Rashba spin-orbit interaction (Kuan et al., 2007; Lucignano et al., 2007). Therefore, understanding how to fabricate high quality quantum structures has received intensive interest from both industrial and scientific communities.

### 1.1.2 MBE growth on GaAs(001)

Molecular beam epitaxy (MBE) (see, for example, Cho and Arthur (1975)) has been the technique of choice for growing epitaxial layers on GaAs surfaces (Davey and Pankey, 1968; Arthur and LePore, 1969; Cho, 1971). This is because MBE provides very precise control of deposition fluxes and growth temperature. MBE

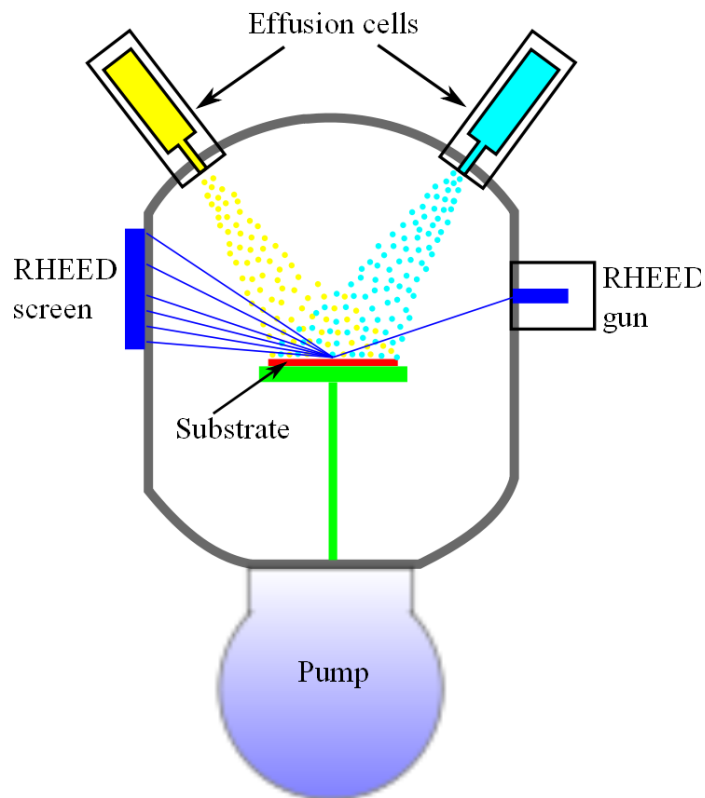


Figure 1.1: Diagram of a typical MBE system growth chamber containing effusion cells for the source materials. Techniques such as RHEED typically monitor the surface during growth.

is conceptually quite simple: molecular beams of material such as Ga and As are evaporated from Knudsen effusion cells and deposited on the atomically flat surface at a certain temperature. The surface structures and the deposition thickness are monitored in real-time using characterization techniques such as reflection high energy electron diffraction (RHEED) (Neave et al., 1983; Hove et al., 1983; Joyce et al., 1986; Stroscio et al., 1993; Horio et al., 1996), see Fig. 1.1. The deposition species impinge on the surface and undergo a variety of fundamental processes including surface diffusion, nucleation and/or step attachment depending on the deposition conditions (Voigtländer, 2001; Mutaftschiev, 2001; Barth et al., 2005). A large variety of structures including atomically flat surfaces (homoepitaxy), epitaxial layers of a different material (heteroepitaxy), QDs and QRs can be fabricated by varying the growth conditions or by using variants of MBE such as droplet epitaxy (Joyce and Vvedensky, 2004; Ohtake, 2008; Tersoff et al., 1996; Moison et al., 1994; Mano et al., 2005; Somaschini et al., 2009; Barth et al., 2005). Fig. 1.2 illustrates some of these structures. Understanding the basic physical processes underpinning the formation of these structures is of critical importance to tailor their properties for potential device applications.

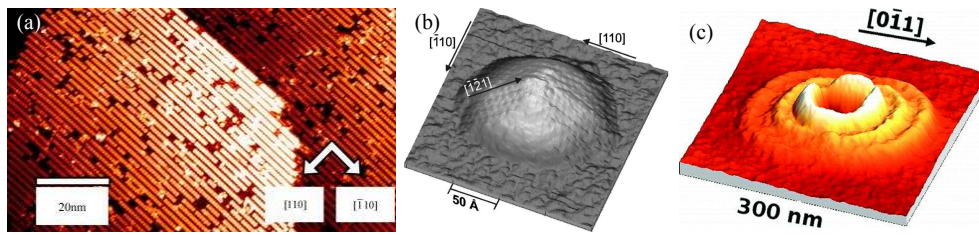


Figure 1.2: (a) STM image of a GaAs(001) sample grown by homoepitaxy showing a  $(2 \times 4)$  surface reconstruction (Bastiman et al., 2009). (b) STM image of an InAs QD grown on GaAs(001) by heteroepitaxy (Márquez et al., 2001). (c) AFM image of multiple concentric quantum rings grown by droplet epitaxy (Somaschini et al., 2009).

### 1.1.3 Homoepitaxy

Homoepitaxy is one of the most common epitaxial processes conducted in MBE, the aim being to produce an atomically flat surface for the subsequent growth of heteroepitaxial layers or quantum structures (Xue et al., 1997; Joyce and Vvedensky, 2004; Ohtake, 2008). Fig. 1.2(a) is a scanning tunneling microscopy (STM) image of a GaAs(001) layer grown by homoepitaxy (Bastiman et al., 2009). This so-called buffer layer is normally achieved by the deposition of Ga and As species at 580-620 °C after thermal cleaning of a GaAs(001) substrate (Smith et al., 1991). The quality of the homoepitaxial layer is affected by a number of factors including the relative amounts of Ga and As, the deposition rate, and the growth temperature. Varying the growth conditions leads to the formation of a wide variety of surface reconstructions ranging from the most As-rich  $c(4 \times 4)$ , through  $(2 \times 4)$ ,  $(6 \times 6)$  and  $c(8 \times 2)$ , to the Ga-rich  $(4 \times 6)$  (Joyce and Vvedensky, 2004; Xue et al., 1997; Ohtake, 2008; LaBella et al., 2005). These reconstructions influence both the quality of the buffer layer and the growth of subsequent epilayers (Avery et al., 1997; Kneedler et al., 1997). The prevailing opinion is that the best quality of GaAs buffer layer is obtained under the conditions when the surface forms  $\beta 2(2 \times 4)$  (Xue et al., 1997). Therefore, understanding the phase transition dynamics of GaAs(001) during homoepitaxy is important to improve material quality.

### 1.1.4 Heteroepitaxy

Heteroepitaxy on GaAs (001) frequently involves the deposition of alloy layers with the same crystalline structure but different composition for various device applications (Liu et al., 1999; Kirstaedter et al., 1994; Choquette et al., 2000; Loss and DiVincenzo, 1998; Miller et al., 1984; Leonard et al., 1993; Finley et al., 1998). The differing composition gives rise to different lattice parameters and misfit strain in the deposited layers. AlGaAs, for example, is associated with low misfit strain whereas InGaAs layers have much greater lattice mismatch. In the latter case, the large misfit (up

to 7% for InAs) gives rise to the possibility of strain induced 3D island formation which relieves misfit strain in the deposited layer (Grundmann et al., 1995a; Priester and Lannoo, 1995; Chen and Washburn, 1996; Shchukin and Bimberg, 1999). Such dislocation free 3D islands, or so-called quantum dots, can be subsequently buried by the deposition of a capping layer and used for device applications including novel laser systems (Kirstaedter et al., 1994; Landin et al., 1998; Marzin et al., 1994; Grundmann et al., 1995b). However, the performance of quantum dot devices requires narrow size distributions and spatial ordering for some applications (Xie et al., 1995; Yamaguchi et al., 2000) which necessitates a detailed knowledge of quantum dot formation.

The study of quantum dot formation in real-time has, however, remained elusive due to the significant As flux during InAs growth which limits the application of standard imaging methods. It is known that InAs grows via the Stranski-Krastanov growth mode (Yamaguchi et al., 2000; Solomon et al., 1996; Ledentsov et al., 1996) in which layer-by-layer growth is followed by QD formation at a so-called critical thickness (Heitz et al., 1997; Tu and Tersoff, 2004; Jesson et al., 2004). The transition from layer by layer to 3D growth occurs rapidly with an incremental deposition of less than 0.1 ML of InAs. Critical dynamic factors such as surface segregation, dot nucleation dynamics and the role of shape transformations during self-assembly are therefore incompletely understood.

### 1.1.5 Droplet epitaxy

Droplet epitaxy is a variant of MBE and is regarded as one of the most promising techniques to prepare exotic quantum nanostructures for a new generation of electronic devices. The technique uses an external As flux to solidify pre-deposited Ga droplets which are around 50 nm in diameter. The nanostructures prepared by droplet epitaxy range from QDs, single quantum rings, double quantum rings, concentric multiple quantum rings (Fig. 1.2(c)), quantum discs and nanoholes dependent on different growth conditions (Mano et al., 2005; Watanabe et al., 2000; Somaschini et al., 2009, 2011*a,b*; Wang et al., 2006, 2007). These structures have distinguishing optoelectronic signatures (Mano et al., 2005; Kuroda et al., 2005; Abbarchi et al., 2009). Controlling the formation of these structures therefore requires an understanding of droplet crystallisation under As flux.

## 1.2 Motivation for the development of III-V LEEM

As discussed above, the key areas of III-V homo-, hetero- and droplet epitaxy would all greatly benefit from real-time imaging of the important growth mechanisms. However, this presents a significant experimental challenge due to the presence of significant As flux (up to  $10^{-5}$  Torr). This limits the application of traditional surface microscopies such as STM (Pashley et al., 1988; Biegelsen et al., 1990; LaBella et al., 1999; Xue

et al., 1995; Ohtake et al., 2002) and atomic force microscopy (AFM) (Kolodziej et al., 2003, 2007; Apostolopoulos et al., 2000) due to interference with and shielding by the tip. The lack of dynamic studies in III-V MBE provides motivation for the development of a III-V surface electron microscope capable of providing new insights into surface phase transformations, QD self-assembly and droplet crystallisation which is the chief research goal of this thesis. Achieving this goal involved three broad stages:

- (i) The basic design and development of the III-V low energy electron microscopy (LEEM) system. The instrument combines III-V MBE with a commercially available LEEM (Elmitec GmbH). Although LEEM has been widely used to study the surfaces of metals and semiconductors over the past three decades, the incorporation of III-V MBE requires significant modifications to cope with the high As flux (chapter 2).
- (ii) Following the establishment of III-V LEEM, the second stage of the thesis is to understand the imaging of 3D structures in the system. Electron microscopy images can be non-intuitive and it is therefore important to investigate contrast mechanisms as a basis for the future study of MBE growth. Experiments were therefore undertaken on Ga droplets and their trails at different microscope defocus settings to obtain a comprehensive data set for subsequent image interpretation. This facilitated the development of caustic and Laplacian theories of mirror electron microscopy (MEM) imaging (chapters 3, 4, 5).
- (iii) Finally, proof of principle applications were undertaken to show that the III-V LEEM could indeed image under high As flux and/or during As evaporation. These studies involved the measurement of the congruent evaporation temperature of GaAs (001) as a function of As incident flux, the asymmetric coalescence of Ga droplets during Langmuir evaporation of GaAs (001) and high temperature studies of As adsorption dynamics on Si (001) (chapters 6, 7, 8).

## 1.3 III-V LEEM

### 1.3.1 Conventional LEEM

Compared with STM, AFM and scanning electron microscopy (SEM), LEEM is characterized by its large field of view and fast imaging rate, which makes it well suited for studying surface dynamics (Bauer, 1994; Phaneuf and Schmid, 2003; Bauer, 2007; Altman, 2010). Over the years, LEEM has been used to study a large variety of surfaces including those of metals (Altman and Bauer, 1996; Pelhos et al., 1999; Altman et al., 1998; Gabaly et al., 2007; Ondrejcek et al., 2005a,b) and semiconductors (Tromp and Hannon, 2002; Hannon and Tromp, 2003). Recently, there is a growing interest in compounds such as  $\text{TiO}_2(110)$  (McCarty and Bartelt, 2003),  $\text{SiC}(0001)$

(Hannon and Tromp, 2008) and GaP(111) (Hilner et al., 2009). The information obtained from these surfaces includes phase transformation dynamics (Telieps and Bauer, 1985; Hannon and Tromp, 2003), surface chemical potentials of adatoms (Theis et al., 1995; Tromp and Mankos, 1998), step dynamics (Bartelt et al., 1994; McCarty et al., 2001; Ondrejcek et al., 2005a,b), surface stress (Hannon et al., 2001, 2002), nucleation and growth of thin films (Tromp and Reuter, 1992; Phaneuf et al., 1997; Sutter et al., 2008), self-organization (Plass et al., 2001; Schmidt et al., 2007), faceting (Ross et al., 1999; Tang et al., 2002), and surface chemical reactions (Schmidt et al., 2000).

The power of LEEM to study surface dynamics originates from its use of low energy electrons for imaging (typically  $\leq 10$  eV). Low energy electrons at a normal incident angle have excellent reflectivity and are well suited for imaging surface dynamics (Bauer, 1998). Fig. 1.3 schematically indicates the electron optical configuration of a LEEM. A coherent electron beam is emitted from Schottky field emitter which is then accelerated to high energy (usually 20 keV), focused by a series of electromagnetic lenses (CL1, CL2, CL3) and deflected by a magnetic prism towards the cathode immersion lens, also called the objective lens (Fig. 1.3 inset). A strong electric field is applied between the sample and the cathode immersion lens which decelerates the incident electrons to the low energy range required for reflection by the sample. The reflected electrons are then reaccelerated by the electric field and deflected by the magnetic prism into the imaging part of the column and then finally focused on the channel plate by the projector lens system where the image is recorded by a CCD camera. An electron diffraction pattern is formed at the back focal plane of the immersion lens, which is shown in Fig. 1.3 inset. However, this is usually imaged in a conjugate plane in the imaging column as shown.

Utilizing such low energy electrons for imaging provides LEEM with strong image intensity to probe the surface, and gives rise to numerous types of image contrast. The image contrast can generally be divided into three categories: reflectivity contrast, diffraction contrast and phase contrast. Reflectivity contrast arises from the difference in electron reflectivity between different surface phases. Diffraction contrast occurs by selecting particular imaging beams associated with diffraction spots in the back focal plane (see Fig. 1.3 inset). This contrast is useful for surface phase transition studies. If the (00) electron beam is selected, bright field imaging is obtained (Fig. 1.4 (a)). Dark field images are formed by selecting any other diffracted electron beams rather than the (00) beam (Fig. 1.4 (b)). In dark field mode, specific phases on the surface can be imaged by selecting a diffraction spot which is associated with the surface periodicity of the phase. While the lateral resolution limit of LEEM is about 4 nm, the vertical resolution can reach atomic scale for the phase contrast imaging of surface steps (Mundschau et al., 1989). In LEEM, phase contrast can be further divided into two categories: quantum size phase contrast and step phase contrast. As its name implies, quantum size contrast originates from the interference between electrons

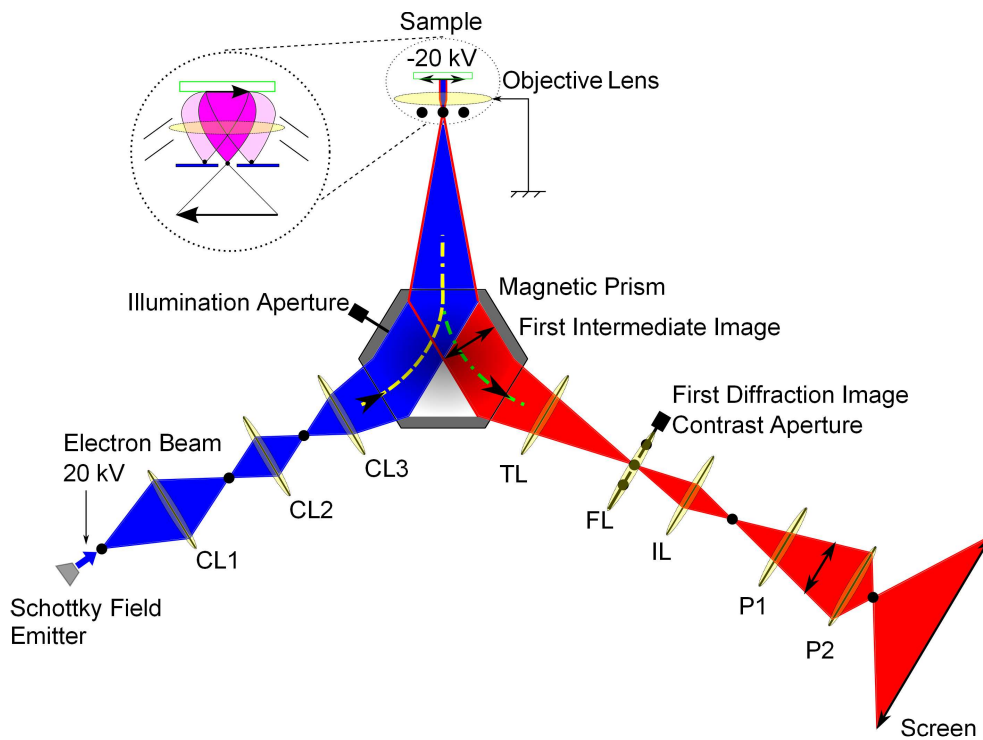


Figure 1.3: Schematic of LEEM optics. The inset shows in schematic form how the objective lens forms an image and a diffraction pattern in the back focal plane.

reflected from the surface of a deposited film and the interface between the substrate and film (shown in Fig. 1.4 (c)) (Altman et al., 2001). Step phase contrast arises from the phase difference of electrons reflected from upper and lower terraces at a step, shown in Fig. 1.4 (d) (Chung and Altman, 1998; Kennedy et al., 2009).

A further complementary technique to the various LEEM imaging modes is that of MEM in which the sample surface is held at slightly more negative potential than the electron source. The incident electrons therefore turn-around before reaching the sample and image contrast results from spatial and/or temporal variations in the near-surface electric field. Such variations may result from surface topography, work function or potential variations across the sample (Nepijko et al., 2001a; Dupuy et al., 1984; Nepijko and Schönhense, 2010). This mode is particularly powerful for imaging 3D objects such as Ga droplets and is used extensively in this thesis.

### 1.3.2 Development of the III-V LEEM (Paper 1)

Although LEEM has been widely used to study surface dynamics, little work has focused on real-time studies of III-V materials. This is mainly because the use of high As flux during MBE growth affects the surface imaging. In chapter 2, we demonstrate how III-V MBE can be incorporated into a LEEM instrument. The system is based on a commercial LEEM instrument (Elmitec LEEM III). However, the incorporation of

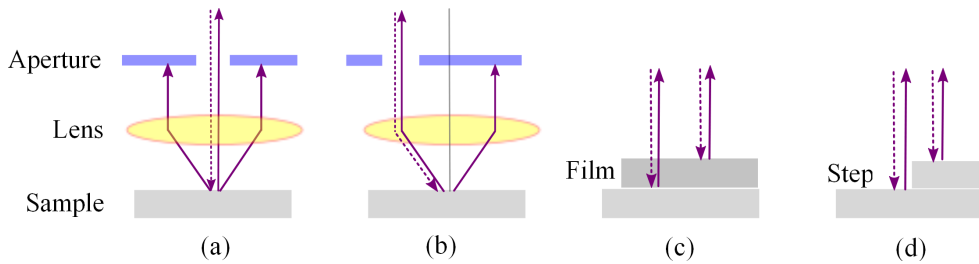


Figure 1.4: Schematic description of contrast mechanism in LEEM: (a) bright field, (b) dark field, (c) quantum size phase contrast, (d) step contrast.

III-V MBE requires numerous modifications including the installation of an internal cooling shroud to limit the build-up of As background pressure, multiple deposition sources with smart design to collimate the deposition beam, magnetic shielding to screen the electron beam from stray fields originating from the MBE sources, a hydrogen atom beam source for surface cleaning at lower temperature (Sugaya and Kawabe, 1991; Tschersich et al., 2008), and an infrared pyrometer for surface temperature measurement. The development of III-V LEEM opens up the possibility of real-time imaging of GaAs surfaces at growth temperature under high As flux.

## 1.4 Understanding MEM image contrast in the III-V LEEM

As discussed in 1.3, the MEM imaging mode is well suited for imaging 3D objects such as droplets on surfaces. It is therefore important to understand the image contrast in detail as a precursor to studying III-V growth mechanisms such as crystallisation during droplet epitaxy. Here we study MEM images of Ga droplets and their trails resulting from motion (Tersoff et al., 2009; Hilner et al., 2009) as a function of microscope defocus. These respectively represent significant and shallow perturbations in surface morphology. The data set is the basis for the development of the Laplacian and caustic imaging theories of LEEM contrast as discussed in sections 1.4.1 and 1.4.2 respectively.

### 1.4.1 Laplacian theory of MEM image contrast (Papers 2, 3)

A large amount of work has been devoted to studying MEM image contrast. Although some approaches are based on wave mechanics (Hermans and Petterson, 1970; Kennedy et al., 2006), the vast majority utilise geometrical ray-tracing techniques (Luk'yanov et al., 1974; Someya and Kobayashi, 1974; Rempfer and Griffith, 1992; Godehardt, 1995). Based on the latter approach, a geometrical theory of MEM contrast has been developed in which images are interpreted as a transverse redistribution of electron current density on an imaging screen (Nepijko and Sedov, 1997). This has

the advantage that for special cases, the transverse shifts can be evaluated analytically which provides important insight into the contrast mechanisms (Nepijko and Sedov, 1997; Nepijko et al., 2001a). However, there is no direct way of intuitively interpreting MEM contrast from a given general specimen.

In Chapter 3 we address this issue by approximating the geometrical theory for the case where surface topography is slowly varying and/or small microscope defocus. We show that the image contrast can be interpreted in terms of the Laplacian of a blurred-surface height function so that the contrast can be intuitively linked to surface features. This is confirmed by the MEM imaging of a Ga trail profile on GaAs (001) which has also been characterised by AFM. The Laplacian theory of MEM contrast is applicable to a wide range of practical imaging situations and is largely independent of specimen illumination details (Kennedy et al., 2011).

#### **1.4.2 Caustic imaging theory of MEM (Paper 4)**

Although the Laplacian imaging theory is simple and intuitive, it is only valid for surface features with slowly varying height profiles. For large variations in surface height, the electron trajectories can deviate so much that very strong image contrast can be produced, including caustics. In Chapter 4 we present a general ray based method of interpreting MEM image contrast using a family or envelope of incident electron rays traced through the electric field close to the specimen surface. Images are then interpreted as caustics in the virtual image plane of the objective lens. To confirm the approach, an experimental through focus series of MEM images of a Ga droplet is compared with image simulations and the optimum defocus condition is established to image droplets in dynamical studies (Tersoff et al., 2009, 2010). A method is developed to utilise caustics to determine the droplet contact angle and the result is in excellent agreement with ex situ AFM measurements.

#### **1.4.3 Electron caustic lithography (Paper 5)**

As seen in 1.4.2, electron caustics are created naturally in MEM. As caustics are regions of very high intensity, reflected electron caustics projected onto a resist-coated wafer would apply a high electron dose to the resist producing a strong response. In Chapter 5 we therefore consider the use of such caustics as a basis for maskless electron beam lithography.

To explore the range of caustics available, we utilise an array of circular micro holes in GaAs (001) fabricated by focussed ion beam (FIB) milling (Fig. 1.5) as a caustic mirror (CAM). Line and fold caustics are experimentally produced in the LEEM which is in excellent agreement with the predictions of caustic imaging theory. It is feasible to tailor specific CAMs by conventional lithography techniques to produce a variety of projected caustics, including curved lines and junctions, with contributions from both surface topography and potential variations.

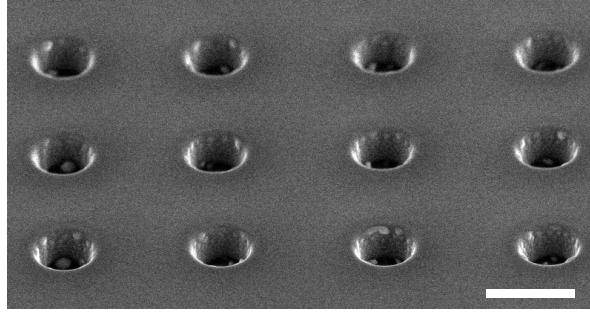


Figure 1.5: SEM image of an array of holes milled by FIB. The scale marker is 1  $\mu\text{m}$  across.

## 1.5 Applications of III-V LEEM

The development of III-V LEEM and our new understanding of image contrast establish a foundation for the study of surface dynamics involving As surface species in real-time. In the following sections we describe three real-time experiments which confirm the potential of III-V LEEM to study critical topics in III-V MBE and As surface dynamics.

### 1.5.1 Controlling the congruent evaporation temperature (Paper 6)

When a GaAs wafer is heated up in a vacuum, the surface undergoes evaporation by decomposing into Ga and As. Such so-called Langmuir evaporation has been intensively studied over the years due both to its scientific and technological importance (Foxon et al., 1973; Arthur, 1967; Goldstein et al., 1976). The congruent evaporation temperature ( $T_c$ ) is critical to understanding the physics of Langmuir evaporation. Below  $T_c$ , Ga and As evaporate at the same rate and preserve chemical stoichiometry. By increasing the evaporation temperature, the chemical stoichiometry of the surface changes accompanied with an increase of Ga chemical potential ( $\mu_{Ga}$ ) (Tersoff et al., 1997). At  $T_c$ ,  $\mu_{Ga}$  reaches the Ga liquidus value ( $\mu_L$ ). Therefore, above  $T_c$ , As preferentially leaves the surface leading to the formation of Ga droplets (Zinke-Allmang et al., 1992; Lowes and Zinke-Allmang, 1993). In addition to droplet formation,  $T_c$  has recently been found to play an important role in droplet motion on GaAs(001) (Tersoff et al., 2009). It is also important for surface cleaning (Isomura et al., 2007) and defining the upper bound in temperature for MBE growth (Tsao, 1993). Consequently, it is important to establish how  $T_c$  varies as a function of experimental conditions.

In Chapter 6 we describe how  $T_c$  can be directly controlled by varying As deposition flux. The III-V LEEM is used to image the stability of Ga droplets which defines a sensitive measure of  $T_c$ . This study provides a means of investigating the

decomposition of III-V materials as well as elucidating the role of As flux during surface preparation and MBE growth.

### **1.5.2 Asymmetric coalescence of Ga droplets (Paper 7)**

The spreading of molten metal droplets at high temperatures, is accompanied by chemical reactions or interdiffusion at the solid-liquid interface which may deform the contact-line structure via mass-transport (Chatain and Carter, 2004; Warren et al., 1998). Such reactive wetting is of appreciable technological importance (Braun et al., 1995; Ambrose et al., 1992, 1993). Compared with non-reactive droplets at ambient temperatures (Narhe et al., 2004), coalescence between reactive droplets is poorly understood. In Chapter 7 we use the III-V LEEM to study the coalescence dynamics of Ga-rich droplets during high temperature annealing. Such droplets readily etch the GaAs surface (Lowes and Zinke-Allmang, 1993) and are consequently a model reactive system. Surprisingly, the coalescence dynamics is observed to be highly asymmetric involving the motion of one reactive droplet relative to the other. Using AFM and selective etching a ridge is identified in the vicinity of the contact line which pins the motion of droplets, giving rise to the asymmetric coalescence phenomena which is described by a simple geometrical model.

### **1.5.3 Dynamics of As on Si(111) (Paper 8)**

The development of III-V LEEM also facilitates the study of As surface dynamics in technologically important systems such as Si. Indeed, As deposition on Si has received considerable attention over the years since it represents the initial stage of GaAs growth on Si and the resulting As-terminated surface is extremely resistant to contamination (Olmstead et al., 1986; Copel et al., 1988; Becker et al., 1988; Zinke-Allmang et al., 1988). In Chapter 8, As adsorption on Si (111) is studied at high temperature to reduce the As surface chemical potential and identify preferential regions of As incorporation. This is seen to occur preferentially in the vicinity of steps which is attributed to a reduction in surface stress associated with  $(1 \times 1)$  As:Si(111) regions. Cycling the incident As flux on and off creates surface roughening and an increased step density which enhances As coverage due to surface stress relief at steps.



---

## Ga droplet surface dynamics during Langmuir evaporation of GaAs

This chapter is an author generated post print of the article

W. X. Tang, C. X. Zheng, Z. Y. Zhou, D. E. Jesson and J. Tersoff, *Ga droplet surface dynamics during Langmuir evaporation of GaAs*, IBM J. Res. & Dev., 55 (2011) 10:1-10:7, available electronically at [http://ieeexplore.ieee.org/xpl/freeabs\\_all.jsp?arnumber=5985561&abstractAccess=no&userType=inst](http://ieeexplore.ieee.org/xpl/freeabs_all.jsp?arnumber=5985561&abstractAccess=no&userType=inst).

## Declaration for Thesis Chapter “Ga droplet surface dynamics during Langmuir evaporation of GaAs”

Declaration by candidate

For this chapter, the nature and extent of my contribution to the work was the following:

Nature of contribution	Extent of contribution(%)
Co-implementation and co-development of the III-V LEEM, co-performed the positioning nanostructures experiments, provided the technical expertise, co-wrote the paper.	20

The following co-authors contributed to the work. Co-authors who are students at Monash University must also indicate the extent of their contribution in percentage terms

Name	Extent of contribution(%)	Nature of contribution
Wen-XinTang (first author)		Co-implementation and co-development of the III-V LEEM, supervised the positioning nanostructures experiments, performed all the other experiments, co-wrote the paper.
Zhenyu Zhou	20	Co-implementation and co-development of the III-V LEEM, co-performed the positioning nanostructures experiments, provided the technical expertise, co-wrote the paper.
David Jesson		Designed and developed the III-V LEEM system, performed droplet coalescence experiments, coordinated the experiment and theoretical studies, co-wrote the paper.
Jerry Tersoff		Co-developed the models.

Candidate's  
signature

	Date 24-08-12
---	------------------

Declaration by co-authors

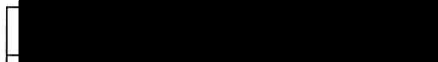
The undersigned hereby certify that:

- (1) they meet the criteria for authorship in that they have participated in the conception, execution, or interpretation, of at least that part of the publication in their field of expertise;
- (2) they take public responsibility for their part of the publication, except for the responsible author who accepts overall responsibility for the publication;
- (3) there are no other authors of the publication according to these criteria;
- (4) potential conflicts of interest have been disclosed to (a) granting bodies, (b) the editor or publisher of journals or other publications, and (c) the head of the responsible academic unit; and
- (5) the original data are stored at the following location(s) and will be held for at least five years from the date indicated below:

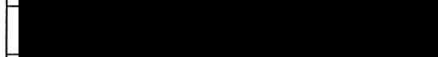
Location(s)

School of Physics, Monash University, Clayton

Signature 1

	Date 21-08-12
---	------------------

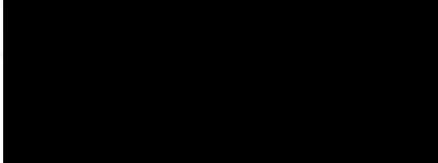
Signature 2

	24-08-2012
---	------------

Signature 3

	21-08-12
---	----------

Signature 4

	24/08/12
---	----------

# Ga droplet surface dynamics during Langmuir evaporation of GaAs

W. X. Tang, C. X. Zheng, Z. Y. Zhou, D. E. Jesson and J. Tersoff

**Abstract:** We describe the design and application of a low energy electron microscope (LEEM) dedicated to the study of III-V materials. Recent studies of Langmuir (free) evaporation of GaAs (001) have been reviewed. Running Ga droplets are observed and the motion is predicted and shown to slow and stop near a characteristic temperature. Striking bursts of “daughter” droplet nucleation accompany the coalescence of large “parent” droplets. These observations imply that evaporation and surface morphology are intimately connected, suggesting a new approach for the self-assembly and positioning of nanostructures on patterned surfaces.

## Introduction

GaAs based devices play a central role in radiofrequency communications technology and optoelectronics. Applications range from mobile phones and wireless networks to laser pointers and DVD players. GaAs high electron mobility transistors and III-V based laser diodes can be viewed as the major components underlying modern communications and optoelectronics. Such structures are composed of thin layers of III-V semiconductor materials, which are grown by molecular beam epitaxy (MBE) with atomic layer precision. Given the technological importance of III-V MBE growth, the real-space imaging of surface growth dynamics is highly desirable. However, this has remained elusive largely because any imaging method must be compatible with the incident As flux, which is a characteristic of III-V MBE.

In parallel with advancing current technologies, longer term objectives in III-V research are to move beyond the constraints of conventional

lithography and fabricate new quantum structures using variants of MBE. Quantum dots, double dots, rings, double rings, molecules and rods have now been assembled [1-4] with potential applications including novel lasers, electron-spin memory and quantum computing. However, a significant limitation in the realisation of new quantum structures is our inability to observe how they form in real time and hence understand how to tailor their characteristics. Just like interfaces grown by MBE, quantum structures are usually created under an As flux at elevated temperatures, and thus, imaging how they form under real growth conditions is highly desirable.

To facilitate imaging of technologically important interface and quantum structure formation under an As flux, we have developed a surface electron microscope integrated with a III-V MBE system. In this paper, we describe the basic design of this III-V low energy electron microscope (LEEM). Applications of III-V LEEM to the study of Langmuir (free) evaporation of GaAs into a vacuum are then reviewed, revealing the unexpected and striking motion of Ga droplets [5] and how decomposition is controlled by surface morphology during evaporation [6].

### **III-V LEEM system**

The basic instrument consists of an Elmitec LEEM III configuration, which incorporates a Schottky field emission electron source for enhanced brightness and beam coherence compared with the conventional LaB<sub>6</sub> gun. Incorporation of III-V MBE required significant modifications, including installation of multiple deposition sources, dedicated equipment for surface cleaning, and an internal cooling shroud to limit the buildup of As background pressure [7]. Figure 1(a) contains an overview of our instrument. A cross-section of the basic LEEM system and the specimen region are shown in Figures 1(b) and (c), respectively.

The system is equipped with Ga and In effusion cells with integrated cooling shrouds and shutters and a metal valve As cracker source (MBE-

Komponenten). Since Ga and In are liquids at high temperature, it is necessary to mount the effusion cells in a face-up configuration [they are located underneath the instrument in Figure 1(a)]. Dual filaments are used to heat the crucibles to minimise droplet formation via condensation near the orifice to improve flux reproducibility. Both sources are equipped with automatic shutters. In order to reduce material deposition in the objective lens region, a pyrolytic boron nitride cap with a small orifice, together with additional Ta shielding, ensures a well-collimated evaporation beam. The Ga source is backed up by an uninterruptible power supply system to maintain the source temperature at 50 °C and prevent cracking of the crucible in the event of a power failure.

The As cracker source consists of a 300-mL As reservoir, which is heated to evaporate the As. A cracking zone on top of the reservoir can be used to convert naturally sublimated  $As_4$  into  $As_2$  if required. An integrated all-metal valve between the reservoir and cracking zone provides precise control of the As flux, which is important for dynamic imaging experiments. The reservoir and cracker temperature gradient is computer controlled during heating and cooling to reduce stress on the valve.

During III-V MBE, it is necessary to reduce the background As pressure resulting from high molecular  $As_4$  or  $As_2$  flux. Our III-V LEEM system therefore incorporates a cooling shroud for this purpose, which prevents discharge between the specimen and objective lens. The Cu shroud design is shown in Figure 1(c). Liquid nitrogen (LN) is supplied via a vacuum feed through to achieve thermal insulation. Small apertures in the shroud allow Ga, In and As fluxes to impinge on the centre of the sample. The background pressure is reduced by nearly 4 orders of magnitude when the shroud is in operation, which provides suitable conditions for imaging. However, following long time exposure to the As flux, the objective lens surface must be cleaned to reduce the probability of discharge. Magnetic shielding surrounds the cathode and anode regions in Figure 1(c) to screen

the electron beam from stray fields originating from the MBE sources. An atomic hydrogen source (AHS) [8] is used for *in situ* surface cleaning of GaAs wafers. The AHS is effective at removing the surface oxide layer and surface impurities such as carbon. Several imaging modes such as LEEM and photoemission electron microscopy (PEEM) are applied in this paper [9-11].

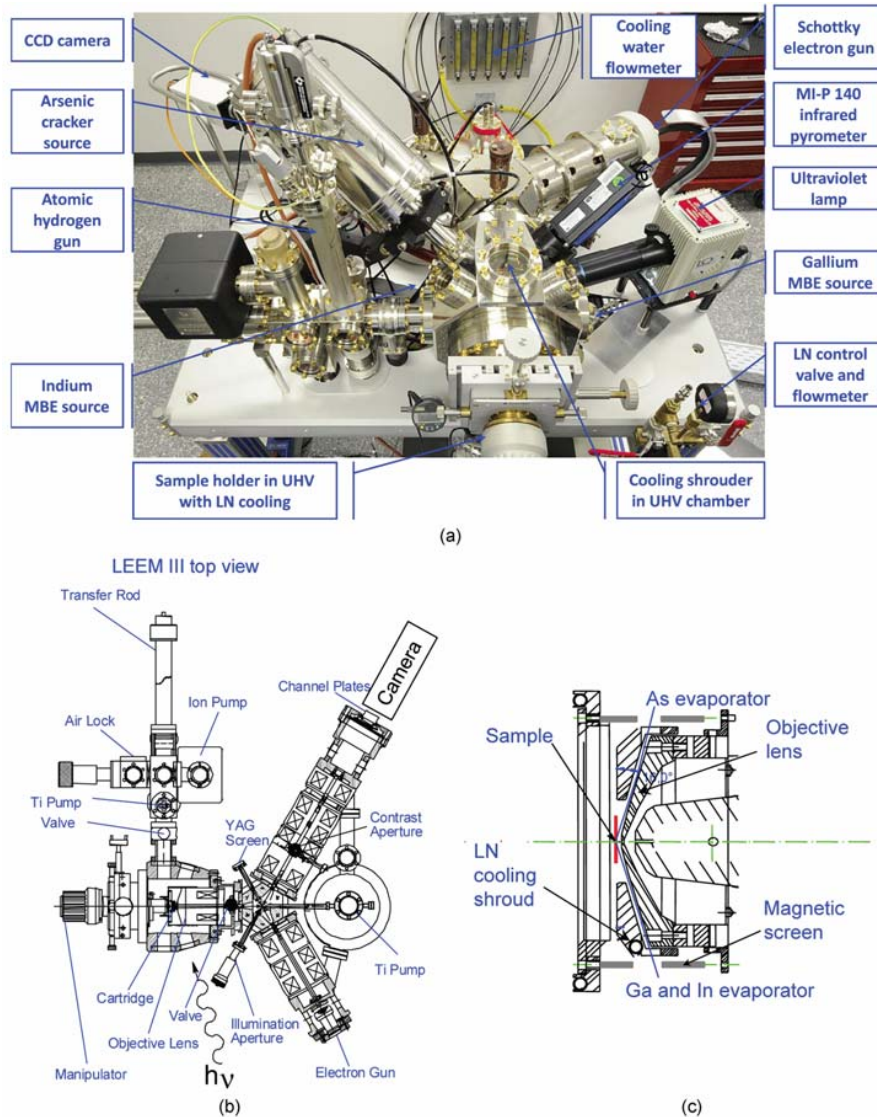


Figure 1 (a) Image of the III-V LEEM system [7]. (b) Cross section of the III-V LEEM instrument. (c) Enlarged view of the objective lens area showing the location of the cooling shroud and access for the MBE sources. (CCD: charge-coupled devices; YAG: yttrium-aluminium garnet.)

## Langmuir evaporation of GaAs

Langmuir (free) evaporation of GaAs (001) into a vacuum has been studied for many decades [12-15]. When heated, GaAs decomposes, and As and Ga fluxes evaporate from the surface. Below congruent evaporation temperature  $T_c$ , the fluxes are equal, preserving the compound stoichiometry. However, above  $T_c$ , As more readily evaporates, leaving behind Ga-rich droplets on the surface [16-19]. There has been a resurgence of interest in such droplets in the area of droplet epitaxy, where they are recrystallised under the As flux to generate GaAs quantum structures. Such structures can now be formed in different geometries, including dots, rings, and multirings with varied potential applications [20-22].

The formation and behaviour of Ga droplets can be imaged by heating an epitaxy-ready (epi-ready) GaAs substrate above  $T_c \sim 625$  °C [15] in the III-V LEEM. An undoped GaAs(001)  $\pm 0.1^\circ$  epi-ready wafer was initially degassed at 300 °C under ultrahigh vacuum for 24 hours in the LEEM system. This was followed by high-temperature flashing up to 600 °C and annealing at 580 °C for 2 hours to remove the surface oxide. Ga droplets were produced by annealing above  $T_c$ . The growth rate of the droplets is strongly dependent on annealing temperature, and this could be used to control their size. The base pressure of the system is below  $2 \times 10^{-10}$  torr, and typical pressures observed during imaging at the annealing temperature of 630 °C are approximately  $1 \times 10^{-9}$  torr with LN cooling of the internal shroud.

Mirror electron microscopy (MEM), in which the specimen potential is adjusted so that electrons turn around just before the surface, is an ideal imaging mode for studying droplets [5,6, 23-26]. A droplet distorts the uniform electric field between the planar sample surface and the objective anode, which significantly redistributes electron intensity. This can cause families of electron rays to overlap, creating strong caustic features in the

image. For a large negative defocus range of the objective lens, droplets appear as dark circles enclosed by a bright caustic ring [see Figure 2(a)]. It should be noted that the caustic ring diameter in Figure 2(a) is larger than the actual perimeter of the droplet so that the droplet size is enlarged in MEM. This contrast can be understood and quantified from a numerical evaluation of classical electron ray trajectories [25].

### Running Ga droplets

The most striking observation in the III-V LEEM is that Ga droplets spontaneously “run” across the surface during annealing. Even after evaporation of many hundreds of monolayers of the crystal, the motion continues. Despite many studies of GaAs Langmuir evaporation over the years [12-17], to our knowledge, Ga droplet dynamics had not been previously observed, illustrating the advantages of *in situ* real-time imaging.

MEM images taken from movies of Ga droplet motion at three different temperatures are shown in Figure 2(a). The epi-ready surface is associated with slight roughness, and as the droplets move, they leave behind a smooth trail. The motion has a stick-slip character. It occurs preferentially along the [110] direction but equally in both directions, ruling out thermal gradient effects. It can be noted in Figure 2(a) that the size of the moving droplets decreases for  $T < T_c$  and increases for  $T > T_c$ . At  $T_c$  the droplet size remains stable, and surprisingly, there is a temperature range of approximately 20 °C about  $T_c$  in which the droplets do not move. To further explore the relationship between motion and temperature, we adjusted the temperature to the desired  $T$  and measured the droplet velocity averaged over many minutes. The results are shown in Figure 2(b). Away from  $T_c$ , the average droplet velocity increases with either increasing or decreasing temperature. This unusual temperature dependence suggests that the motion is intimately linked to  $T_c$ .

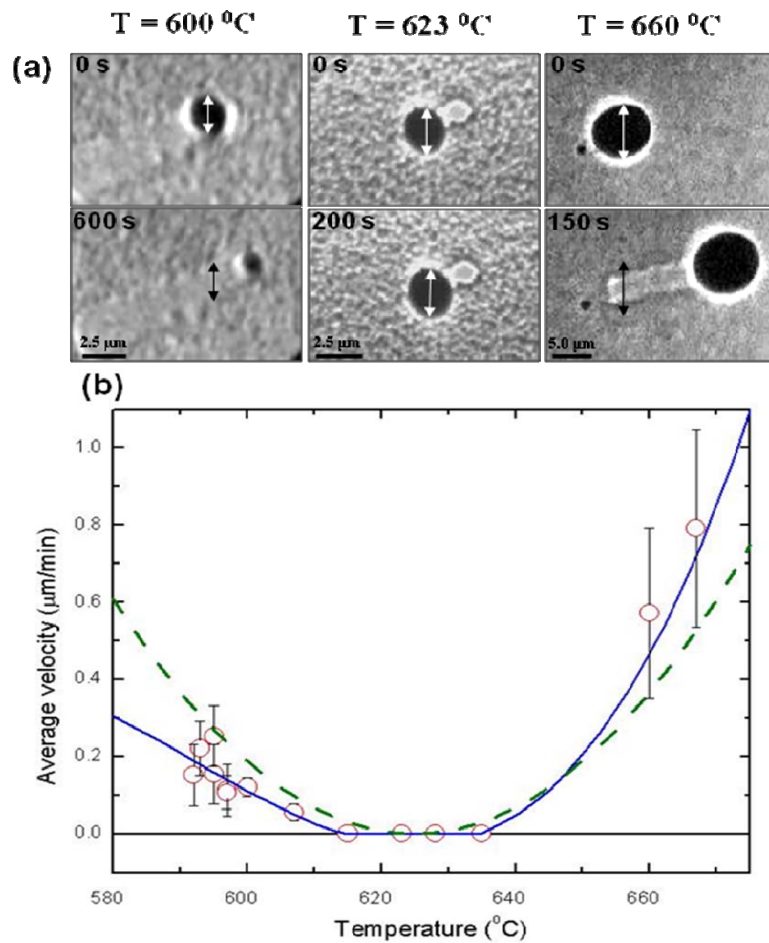


Figure 2 Droplet motion on epi-ready GaAs(001) [5]. (a) Image pairs are shown at successive times for three temperatures  $T$  as indicated; the centre image pair is near the congruent evaporation temperature. Arrows are reference markers for comparing position and diameter at two times. The droplets (left panel) move and shrink below  $T_c$  and (right panel) move and grow above  $T_c$ . Close to  $T_c$  (center panel), there is no visible motion or size change. (b) Average velocity versus temperature. Error bars show root-mean-square scatter of multiple measurements at the same  $T$ . The solid line is the truncated cubic fit described in the text, and the dashed line is the quadratic term alone, which is extracted from the fit.

Guided by the experimental results, it would seem natural to consider the net force on the droplet derived from the thermodynamics of the GaAs

surface during evaporation. The GaAs surface can be characterized by its surface Ga and As chemical potentials, i.e.,  $\mu_{Ga}$  and  $\mu_{As}$ , respectively, where the sum  $\mu_{Ga} + \mu_{As} = \mu_{GaAs}$  is fixed by equilibrium with the crystal, and  $\mu_{GaAs}$  is the bulk crystal free energy per atom pair. Congruent evaporation at a given temperature  $T$  occurs because  $\mu_{Ga}$  adjusts to a steady-state value where Ga and As evaporate at equal rates. Increasing  $T$  favours As evaporation, causing Ga to accumulate on the surface. Consequently,  $\mu_{Ga}$  increases until the Ga and As evaporation rates are equal and congruent evaporation is restored. However, with increasing  $T$ ,  $\mu_{Ga}$  will eventually rise beyond liquidus value  $\mu_L$ , and Ga can nucleate as liquid droplets rather than all evaporating. This defines the upper limit  $T_c$  for congruent evaporation. It is expected that the Ga droplets will stay close to equilibrium with the GaAs crystal at  $\mu_L$ , which gives rise to a disequilibrium between the droplet and surface for temperatures away from  $T_c$ , where  $\mu_{Ga} \neq \mu_L$ .

To see how the disequilibrium in chemical potential results in motion, it is necessary to consider the net force on a droplet when it is displaced (e.g. by a thermal fluctuation). Integrating the force vector around the periphery of the droplet, it can be shown that the total net force on a droplet is proportional to the difference in Gibbs free surface energy of the surfaces exposed and covered during the motion [5]. The newly exposed surface is created in equilibrium with the droplet at chemical potential  $\mu_L$ . However, before being covered by the droplet, the surface on the opposite side had a structure corresponding to  $\mu_{Ga}$ , whereas the reservoir for the excess Ga is now the droplet at  $\mu_L$ . Expanding to the lowest order in  $(T - T_c)$ , one finds that the difference in free surface energy is quadratic in  $(\mu_{Ga} - \mu_L)$  and that  $(\mu_{Ga} - \mu_L)$  is linear in  $(T - T_c)$ , giving the total net force on a droplet of diameter  $d$  at temperature  $T$  as

$$F = \alpha(T - T_c)^2 d, \quad (1)$$

where the coefficient  $\alpha$  embodies both thermodynamic and kinetic properties of the surface [5]. Modelling the time-averaged stick-slip motion as a damped response to  $F$  with an effective frictional force that is independent of velocity and opposite to the direction of motion, then from Equation (1), the velocity becomes

$$v \approx m\alpha(T - T_c)^2 - v_f, \quad (2)$$

where  $m$  is the mobility, and  $v_f$  is the friction term. For  $(T - T_c)^2 < v_f / m\alpha$ ,  $v = 0$ , which is consistent with the region of zero motion about  $T_c$ . When the range of  $T$  is large, it is necessary to include cubic and higher order terms in the expansion about  $T_c$ , and with Equation (2) extended to cubic order, it is possible to fit (solid blue line) the velocity data well, as shown in Figure 2(b). The basic prediction of  $v \propto (T - T_c)^2$  is, however, sufficient to capture the overall general behaviour.

We note that there have been a number of interesting studies of droplet dynamics on surfaces with different proposed mechanisms for motion [27-29]. The mechanism for running droplets described here should be applicable to other III-V semiconductors such as InAs, where the more slowly evaporating component forms droplets on the surface at temperatures where a liquidus exists. More broadly, the droplet motion may create new possibilities to position nanostructures in droplet epitaxy.

### **Droplet coalescence during Langmuir evaporation**

Above  $T_c$ , excess Ga is left behind during evaporation and diffuses to the droplets, which grow via adatom capture. Occasionally, however, droplets

also abruptly grow via coalescence [6,9] These events are particularly interesting, as illustrated by the sequence of PEEM images shown in Figure 3. Droplet 1 in Figure 3(a) is absorbed into droplet 2 (which remains stationary) in a coalescence event [see Figure 3(b)]. This leaves behind the etch pit framed in Figure 3(b) and magnified in Figure 3(c). Within 2 seconds, a rapid burst of daughter droplet nucleation occurs within this area. Following rapid growth, they begin to move at  $t = 51$  seconds. Eventually, the droplets move outside the etch pit arena, and there is no subsequent nucleation suggesting an unanticipated nucleation mechanism.

To elucidate the mechanism we employ MEM [5,6,23-26] to reveal information on surface morphology. In particular, MEM movies of coalescence events similar to Figure 3 reveal that the concave etch pit left behind by the coalescing droplet planarizes with time, and only then do the daughter droplets move away from the region. The time for significant planarization corresponds to the initial burst of nucleation and growth of the daughter droplets with no further nucleation occurring after the surface is planarized.

### **Simple model for Langmuir evaporation of GaAs**

The linkage between planarization and droplet formation suggests surface steps are important, and we develop a simple model of Langmuir evaporation from a miscut wafer of mean step spacing  $L_s$ . Our assumption is that Ga adatoms persist on the surface long enough to maintain approximate equilibrium between terrace and steps [30]. However, it is known that As readily evaporates, and a constant excess flux of As is required to prevent decomposition during MBE [15]. Consequently, we assume that, at our experimental temperatures, As surface species evaporate too rapidly to maintain a significant population across the terrace. Then, the rate of As evaporation is proportional to step density, whereas Ga evaporation is independent of step density. Formalizing this using a

standard transition-state model for As and Ga evaporation, the evaporation rates per unit area are

$$F_{Ga} = r_{Ga} \exp\left(\frac{\mu_{Ga} - E_{Ga}}{kT}\right), \quad (3)$$

$$F_{As} = r_{As,s} L_s^{-1} \exp\left(\frac{N(\mu_{GaAs} - \mu_{Ga}) - E_{AsN}}{kT}\right). \quad (4)$$

Here,  $E_{Ga}$  and  $E_{AsN}$  are the respective transition-state energy values for Ga and As evaporation, and it is assumed that the As transition state consists of  $N$  atoms. The rate constants  $r_{Ga}$  (per unit area) and  $r_{As,s}$  (per unit step length) include the transition-state entropy or degeneracy, for example, the density of sites for evaporation. As discussed earlier,  $\mu_{Ga}$  increases with increasing  $T$  until  $F_{Ga} = F_{As}$ . However, if  $\mu_{Ga}$  rises above the liquidus value, Ga can accumulate as droplets, which defines  $T_c$ . Inserting Equations (3) and (4) in the condition  $F_{Ga} = F_{As}$  for  $\mu_{Ga} = \mu_L$  then yields an expression for the congruent evaporation temperature, i.e.,

$$kT_c = \frac{(N+1)\mu_L - N\mu_{GaAs} - E_{Ga} + E_{AsN}}{\ln(r_{As,s} / L_s r_{Ga})}. \quad (5)$$

This simple model leads to several important predictions [6]. First, above  $T_c$ , if droplet coalescence suddenly exposes an etch pit of much higher local miscut, then that region will experience much faster As evaporation and Ga release, explaining the burst of nucleation and subsequent growth of the daughter droplets. Second, the release of Ga increases  $\mu_{Ga}$  in the etch pit region. This drives the surface further from the liquidus composition, which enhances the force for the droplet motion [5] and accounts for the rapid daughter droplet dynamics. Finally, it can be observed in Equation (5) that  $T_c$  depends on the miscut via the mean step spacing  $L_s$ . This has potential

implications for positioning nanostructures, which we consider in the next section.

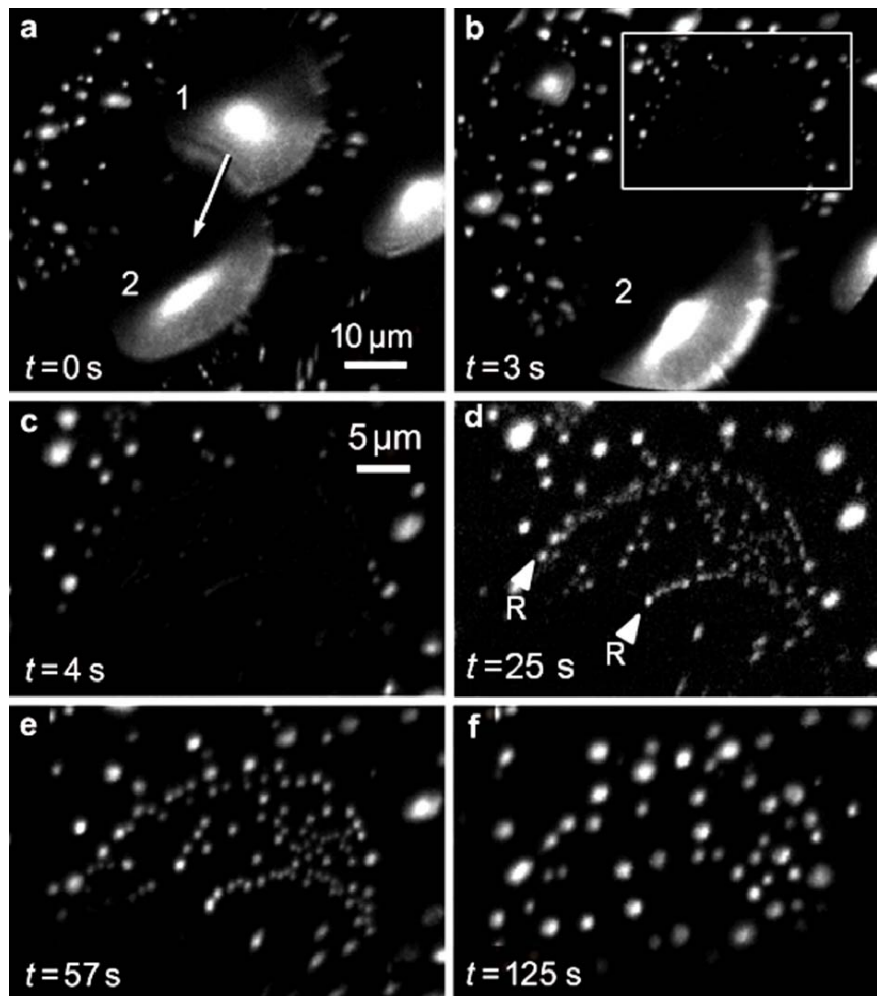


Figure 3 Images captured from a PEEM video of Ga droplet coalescence at 630 °C [6]. Liquid Ga appears bright against dark GaAs. (a) Droplets 1 and 2 are in close proximity at  $t=0$ . (b) At  $t=3$  seconds, droplet 1 translates across the substrate and coalesces with droplet 2, leaving an exposed shallow etch pit. This exposed etch pit, which is enclosed by the frame in (b), is magnified in (c-f). Daughter droplet formation and (d) growth are sometimes associated with surface ridges, R.

### **Positioning nanostructures using spatial variations in $T_c$**

Equation (5) indicates that regions of the surface possessing a higher local miscut will have a lower  $T_c$ , suggesting new possibilities for controlled nanostructure formation on lithographically patterned substrates. Evaporation should preferentially occur on the most highly sloped regions, allowing generation of droplets at predetermined locations. Annealing at temperatures above  $T_c$  for the sloped regions, but below  $T_c$  for the surrounding planar surface, should provide especially reliable Ga placement. The droplets could then be converted into quantum structures under an overpressure of a group V vapour as in standard droplet epitaxy methods [2, 20-22].

We have demonstrated droplet positioning at a proof-of-concept level. We first heated a GaAs(001) sample above  $T_c$  to form a number of well-separated Ga droplets [see Figure 4(a)] The sample was then cooled below  $T_c$  so that the Ga droplets shrink and eventually disappear [see Figure 4(b)]. This leaves a surface patterned with nanoscale depressions due to droplet etching. The largest droplet, which is designated 1 in Figure 4(a), is associated with the deepest etch pit and was the last to disappear. When we slowly increase the temperature to 620 °C, a new droplet appears at precisely the same position as droplet 1 [see Figure 4(c)]. We can control the stability of this single droplet over a significant time period (many minutes) and temperature range  $\pm 5$  °C [see Figure 4(d)]. On increasing the temperature to 635 °C, a new droplet is generated in the etch pit previously occupied by droplet 2 [see Figure 4(e)]. Even after 1 minute of annealing at 635 °C, approximately 90% of the new droplets generated in Figure 4(f) correspond to etch pit positions. This demonstrates that droplet positions can be controlled by surface patterning.

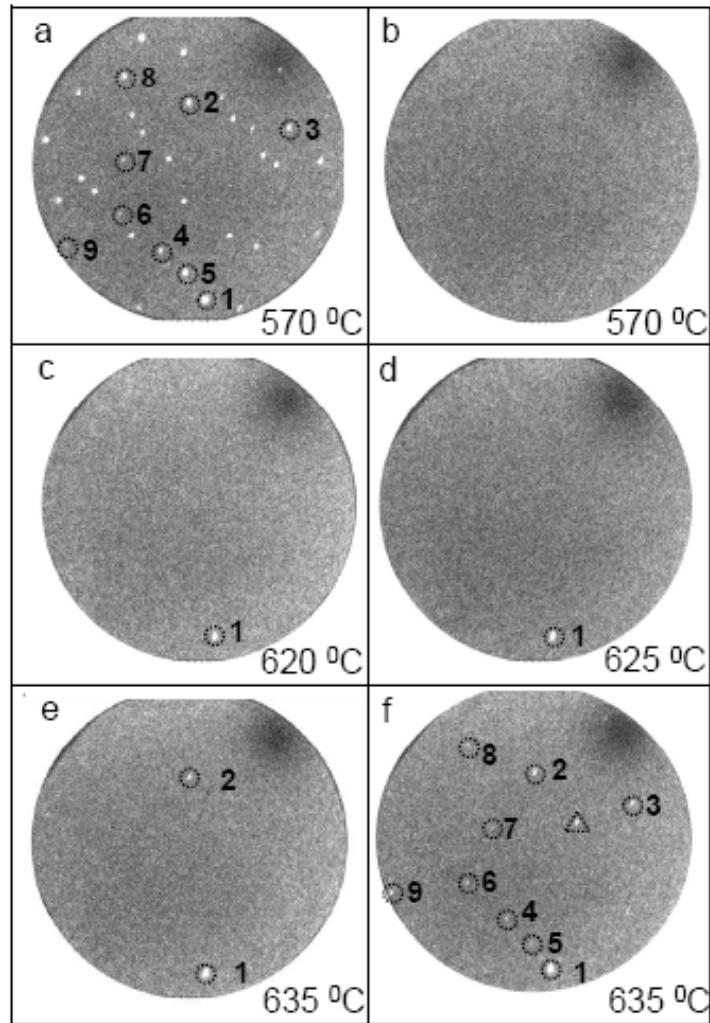


Figure 4 PEEM images of Ga droplet shrinkage and formation [6]. (a) The sample is cooled below  $T_c$  so that Ga droplets shrink and eventually disappear in (b). Circled droplet 1 in (a) is the largest droplet and the last to disappear. (c) On slowly heating the sample to 620 °C, a new droplet is generated in the original position of droplet 1. (d) This droplet was stable in the temperature range of 620–625 °C for several minutes. (e) Increasing the temperature to 635 °C results an additional droplet appearing at the original position of droplet 2 in (a). (f) After a further minute at 635 °C, 90% of the new droplets correspond to previous droplet positions in (a) (circled droplets). The droplet enclosed by a triangle has appeared at a new position.

## Conclusions

We have described the design of a III-V surface electron microscope and its application to study Langmuir evaporation of GaAs(001). Droplets move during evaporation, which is driven by disequilibrium with the surface, giving rise to an unusual temperature dependence. Coalescence events are associated with the nucleation and motion of numerous “daughter droplets”. These observations indicate a morphology-dependent congruent evaporation temperature, which has important implications for writing nanostructures.

## Acknowledgments

The work of D. E. Jesson and W. –X. Tang was supported by the Australian Research Council under grant DP0985290. We thank Rod Mackie for technical support.

## References

- [1] B. A. Joyce and D. D. Vvedensky, “Self-organized growth on GaAs surfaces,” *Mat. Sci. Eng. R.*, vol. 46, no. 6, pp. 127-176, Dec. 2004.
- [2] J. H. Lee, Z. M. Wan., Z. Y. AbuWaar, and G. J. Salamo, “Design of nanostructure complexes by droplet epitaxy,” *Cryst. Growth Des.*, vol. 9, no. 2, pp. 715-721, Jan. 2009.
- [3] S. Kiravittaya, A. Rastelli, and O. G. Schmidt, “Advanced quantum dot configurations,” *Rep. Prog. Phys.* vol. 72, no. 4, article no. 046502, Mar. 2009.
- [4] D. Spirkoska, C. Colombo, M. Heiss, G. Abstreiter, and A. F. I. Morral, “The use of molecular beam epitaxy for the synthesis of high purity III–V nanowires,” *J. Phys. Condens. Matter.* vol. 20, no.45, article no. 454255, Nov. 2008.
- [5] J. Tersoff, D. E. Jesson, and W. X. Tang, “Running droplets of Ga from evaporation of Ga arsenide,” *Science*, vol. 324, no. 5924, pp. 236-238. Apr. 2009.

- [6] J. Tersoff, D. E. Jesson, and W. X. Tang, "Decomposition controlled by surface morphology during Langmuir evaporation of GaAs," *Phys. Rev. Lett.*, vol.105, no. 3, p. 035702, Jul. 2010.
- [7] D. E. Jesson and W. X. Tang, "Surface Electron Microscopy of Ga Droplet Dynamics on GaAs(001)," in *Microscopy: Science, Technology, Applications and Education*, A. Méndez-Vilas, J. Díaz, Eds. Badajoz, Spain: Formatex, 2010, pp. 1608-1619.
- [8] K. G. Tschersich and V. von Bonin, "Formation of an atomic hydrogen beam by a hot capillary," *J. Appl. Phys.*, vol. 84, no. 8, pp.4065-4070, Oct. 1998.
- [9] E. Bauer, "Low energy electron microscopy". *Rep. Prog. Phys.* vol. 57, no. 9, pp. 895–938, sep. 1994
- [10] A. B. Pang, T. Müller, M. S. Altman, and E. Bauer, "Fourier optics of image formation in LEEM," *J. Phys. Condens. Matter*, vol. 21, no. 31, article no. 314006, Jul. 2009.
- [11] S. Günther, B. Kaulich, L. Gregoratti, and M. Kiskinova, "Photoelectron microscopy and applications in surface and materials science," *Prog. Surf. Sci.*, vol.70, no. 4-8, pp. 187-260, Jul. 2002.
- [12] C. T. Foxon, J. A. Harvey, and B. A. Joyce, "The evaporation of GaAs under equilibrium and non-equilibrium conditions using a modulated beam technique," *J. Phys. Chem. Solids.*, vol. 34, no. 10, pp. 1693-1701, Oct. 1973.
- [13] J. R. Arthur, "Vapor pressures and phase equilibria in the Ga-As system," *J. Phys. Chem. Solids.*, vol. 28, no. 11, pp. 2257-2267, Nov. 1967.
- [14] B. Goldstein, D. J. Szostak, and V. S. Ban, "Langmuir evaporation from the (100), (111A), and (111B) faces of GaAs," *Surf. Sci.*, vol. 57, no. 2, pp.733-740, Jul. 1976.
- [15] J. Y. Tsao, *Materials Fundamentals of Molecular Beam Epitaxy*. 1st ed., San Diego, CA: Academic,1993.
- [16] M. Zinke-Allmang, L. C. Feldman, and W. van Saarloos, "Experimental study of self-similarity in the coalescence growth regime," *Phys. Rev. Lett.* vol. 68, no. 15, pp. 2358-2361, Apr. 1992.

- [17] T. D. Lowes and M. Zinke-Allmang. "Microscopic study of cluster formation in the Ga on GaAs(001) system," *J. Appl. Phys.*, vol. 73, no. 10, pp.4937-4941, May 1993.
- [18] Z. Y. Zhou, C. X. Zheng, W. X. Tang, D. E. Jesson and J. Tersoff, "Congruent Evaporation Temperature of GaAs(001) Controlled by As Flux," *Appl. Phys. Lett.*, vol. 97, article no. 121912, Sep. 2010.
- [19] Z. Y. Zhou, W. X. Tang, D. E. Jesson and J. Tersoff, "Time-Evolution of the Ga Droplet Size-Distribution during Langmuir Evaporation of GaAs(001)," *Appl. Phys. Lett.*, vol. 97, no. 19, article no. 191914, Nov. 2010.
- [20] T. Mano, T. Kuroda, S. Sanguinetti, T. Ochiai, T. Tateno, J. Kim, T. Noda, M. Kawabe, K. Sakoda, G. Kido, and N. Koguchi "Self-assembly of concentric quantum double rings," *Nano Lett.*, vol. 5, no. 3, pp.425-428, Mar. 2005.
- [21] M. Yamagiwa, T. Mano, T. Kuroda, T. Tateno, K. Sakoda, G. Kido, N. Koguchi, and F. Minami "Self-assembly of laterally aligned quantum dot pairs," *Appl. Phys. Lett.*, vol. 89, no. 11, article no. 113115, Sep. 2006.
- [22] C. Somaschini, S. Bieti, N. Koguchi, S. Sanguinetti . Fabrication of multiple concentric nanoring structures. *Nano Lett.*, vol. 9, no. 10, pp. 3419-3424, Sep. 2009.
- [23] S. M. Kennedy, C. X. Zheng, W. X. Tang, D. M. Paganin, and D. E. Jesson, "Laplacian image contrast in mirror electron microscopy (addendum)," *Proc. Roy. Soc. A.*, published online, DOI: 10.1098/rspa.2011.9204.
- [24] S. M. Kennedy, C. X. Zheng, W. X. Tang, D. M. Paganin, and D. E. Jesson, "Laplacian image contrast in mirror electron microscopy," *Proc. Roy. Soc. A*, vol. 466, no. 2122, pp. 2857–2874, Oct. 2010.
- [25] S. M. Kennedy, C. X. Zheng, W. X. Tang, D. M. Paganin, and D. E. Jesson, "Caustic Imaging of gallium droplets using mirror electron microscopy," *Ultramicroscopy*, vol. 111, no. 5, pp. 356-363, Apr. 2011.

- [26] S. M. Kennedy, D. M. Paganin, and D. E. Jesson, "Laplacian and caustic imaging theories of MEM work-function contrast," *IBM J. Res. Dev.*, vol. 55, no. 4, paper 3, pp. 3:1-3:8, 2011.
- [27] E. Hilner, A.A. Zakharov, K. Schulte, P. Kratzer, J. N. Andersen, E. Lundgren, and A. Mikkelsen, "Ordering of the nanoscale step morphology as a mechanism for droplet self-propulsion," *Nano. Lett.*, vol. 9, no.7, pp. 2710-2714, Jun. 2009.
- [28] W.C. Yang, H. Ade, and R.J. Nemanich, "Stability and dynamics of Pt-Si liquid microdroplets on Si(001)," *Phys. Rev. B; Condens. Matter*, vol. 69, no. 4, article no. 045421, Jan. 2004.
- [29] P. Sutter, P.A. Bennett, J. I. Flege, and E. Sutter, "Steering liquid Pt-Si nanodroplets on Si(100) by interactions with surface steps," *Phys. Rev. Lett.*, vol. 99, no. 12, article no. 125504, Sep. 2007
- [30] J. Tersoff, M. D. Johnson, and B. G. Orr, "Adatom densities on GaAs: Evidence for near-Equilibrium growth", *Phys. Rev. Lett.*, vol. 78, no. 2, pp. 282-285, Jan. 1997.

---

## Laplacian image contrast in mirror electron microscopy

This chapter is an author generated post print of the article

S. M. Kennedy, C. X. Zheng, W. X. Tang, D. M. Paganin and D. E. Jesson, Laplacian image contrast in mirror electron microscopy,

Main paper:

Proc. R. Soc. A, 466 (2010) 2857-2874, available electronically at <http://rspa.royalsocietypublishing.org/content/466/2122/2857>.

Addendum:

Proc. R. Soc. A, 467 (2011) 3332-3341, available electronically at <http://rspa.royalsocietypublishing.org/content/467/2135/3332.short>.

## Declaration for Thesis Chapter "Laplacian image contrast in mirror electron microscopy"

Declaration by candidate

For this chapter, the nature and extent of my contribution to the work was the following:

Nature of contribution	Extent of contribution(%)
Designed and performed AFM and MEM experiments and co-wrote the paper	25

The following co-authors contributed to the work. Co-authors who are students at Monash University must also indicate the extent of their contribution in percentage terms

Name	Extent of contribution(%)	Nature of contribution
Shane Kennedy	70	Developed the model used in the paper, performed the image simulations, co-wrote the paper.
Wen-XinTang		Provided technical expertise
David Paganin		Co-wrote the paper, co-developed the model and provided technical expertise.
David Jesson		Co-wrote the paper, co-developed the model and provided technical expertise.

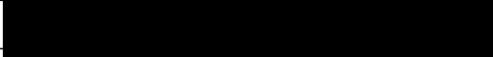
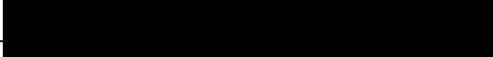
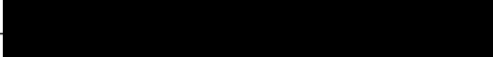
Candidate's signature		Date 24-08-12
-----------------------	--	------------------

**Declaration by co-authors**

The undersigned hereby certify that:

- (1) they meet the criteria for authorship in that they have participated in the conception, execution, or interpretation, of at least that part of the publication in their field of expertise;
- (2) they take public responsibility for their part of the publication, except for the responsible author who accepts overall responsibility for the publication;
- (3) there are no other authors of the publication according to these criteria;
- (4) potential conflicts of interest have been disclosed to (a) granting bodies, (b) the editor or publisher of journals or other publications, and (c) the head of the responsible academic unit; and
- (5) the original data are stored at the following location(s) and will be held for at least five years from the date indicated below:

Location(s)	School of Physics, Monash University, Clayton
-------------	---

Signature 1		Date 23-08-12
Signature 2		21-08-12
Signature 3		24-8-2012
Signature 4		21-08-12

# Laplacian image contrast in mirror electron microscopy

BY S. M. KENNEDY, C. X. ZHENG, W. X. TANG, D. M. PAGANIN, D. E. JESSON†

*School of Physics, Monash University, Victoria 3800, Australia.*

We discuss an intuitive approach to interpreting mirror electron microscope (MEM) images, whereby image contrast is primarily caused by the Laplacian of small height or potential variations across a sample surface. This variation is blurred slightly to account for the interaction of the electrons with the electrical potential away from the surface. The method is derived from the established geometrical theory of MEM contrast, and whilst it loses quantitative accuracy outside its domain of validity, it retains a simplicity that enables rapid interpretation of MEM images. A strong parallel exists between this method and out of focus contrast in transmission electron microscopy (TEM), which allows a number of extensions to be made such as including the effects of spherical and chromatic aberration.

**Keywords:** Mirror electron microscopy (MEM), Laplacian image contrast, phase contrast, Ga droplets, GaAs

## 1. Introduction

Mirror electron microscopy (MEM) is a well-established technique which has seen wide application in the real time study of surface phenomena. Applications include the study of chemical processes at solid surfaces (Świąch *et al.* 1993), surface magnetic fields (Barnett & Nixon 1967*a*), electric field contrast (Luk'yanov *et al.* 1974; Bok 1978; Slezák *et al.* 2000; Shimakura *et al.* 2008) and droplet surface dynamics (Tersoff *et al.* 2009). MEM is unique in surface electron microscopy in that electrons neither impact nor are emitted from the specimen surface. Instead, a near-normally incident beam is reflected at equipotential surfaces just above the specimen. This is achieved by holding the specimen at a small negative voltage relative to the electron source. As the electrons reverse direction, they are travelling very slowly and are consequently sensitive to spatial and/or temporal variations in microfields in the vicinity of the surface. These microfields may, for example, result from small variations in the electric field above the cathode caused by the surface topography (Bauer 1998; Nepijko *et al.* 2001*b*; Speake & Trenkel 2003) and/or variations in the electric potential of the specimen itself, including contact potentials, surface charges and varying conductivity (Barnett & Nixon 1967*a, b*; Luk'yanov *et al.* 1974; Bok 1978; Świąch *et al.* 1993; Godehardt 1995). MEM therefore has a significant advantage in that it can probe surface phenomena benignly, without electrons impacting the surface.

The reflected electrons in MEM contain information concerning microfields which are in turn related to the topography and/or the electrical and magnetic properties of the surface. This has stimulated significant efforts over the years to interpret MEM image contrast and extract quantitative information regarding the microfields and surface properties. Although a variety of approaches have been employed, including some based on wave mechanics (Hermans & Petterson 1970; Kennedy *et al.* 2006), most have been based on geometrical ray tracing techniques (Barnett & Nixon 1967*b*; Sedov 1970; Luk'yanov *et al.* 1974; Someya & Kobayashi 1974; Bok 1978; Rempfer & Griffith 1992; Świąch *et al.* 1993; Godehardt 1995). Building on this latter work, a geometrical theory has been developed in which MEM contrast is viewed as a transverse redistribution of electron current density on an imaging screen due to shifts in electron trajectories following interaction with microfields just above the specimen surface (Sedov 1970; Dyukov *et al.* 1991; Nepijko & Sedov 1997). This work, which has been used extensively to simulate MEM and photoemission electron microscopy (PEEM) contrast in a variety of situations (Nepijko *et al.* 2001*a, b*, 2003, 2007; Jesson *et al.* 2007; Nepijko & Schönhense 2010; Tang *et al.* 2009), will form the basis of this paper and we henceforth refer to this approach as the geometrical theory of MEM contrast.

An advantage of the geometrical theory of MEM contrast is that, for special geometries, the electron shifts can be calculated analytically which can provide important insight into the mechanisms of contrast (Nepijko & Sedov 1997; Nepijko *et al.* 2001*a*). Presently, however, there is no direct way of intuitively interpreting MEM contrast of a given general specimen. Here, we present a theory of Laplacian image contrast (see, for

† Author for correspondence (██████████).

example, Berry (2006)) in MEM which is an approximation of the geometrical theory, yet applicable to a wide range of practical imaging situations. The advantage of the theory is that the image contrast can be interpreted in terms of the Laplacian of an effective two-dimensional phase object which is directly related to the near-surface microfield. For variations in surface topography, the effective phase is related to a blurred surface height function so that the contrast can be intuitively linked to surface features. Even beyond its strict range of applicability, Laplacian image contrast retains a simplicity which enables rapid interpretation of MEM images. We will show that a strong parallel exists between this method and ‘out of focus’ contrast in transmission electron microscopy (TEM) (Cowley 1995; Spence 2003). This allows a number of extensions to be made to the intuitive method, such as including the effects of spherical and chromatic aberration.

## 2. Geometrical theory of MEM contrast

Nepijko, Sedov and Dyukov (Dyukov *et al.* 1991; Nepijko & Sedov 1997), building upon earlier work of Sedov (1970), Luk’yanov *et al.* (1974) and others (Barnett & Nixon 1967*b*; Bok 1978) have developed a robust geometrical theory of MEM contrast. The approach utilizes a predominantly classical ‘ray based’ description of the electron motion inside the imaging system. While the major results are quoted by Nepijko & Sedov (1997) and Nepijko *et al.* (2001*b*, 2003), and many salient points of the theory are emphasized by Luk’yanov *et al.* (1974), the foundations of the methodology are less accessible (Dyukov *et al.* 1991, in Russian). Since the geometrical theory is the basis for our development of a theory of Laplacian image contrast in MEM, we therefore briefly summarize the key steps here, highlighting the assumptions used in the general case as well as adapting the method to a low energy electron microscope (LEEM) imaging system.

A typical electrostatic MEM immersion lens is shown schematically in figure 1. Here the  $z$  axis coincides with the optical axis of the immersion lens and the anode aperture corresponds to the  $(x, y)$  plane of a Cartesian coordinate system. The specimen is held at a negative potential ( $V < 0$ ) relative to the grounded anode aperture a distance  $L$  away. The specimen therefore acts as the cathode of the immersion objective lens (Barnett & Nixon 1967*b*; Luk’yanov *et al.* 1974; Bok 1978; Bauer 1985). Electrons, accelerated to initial energy  $U$ , travel along the optic axis, pass through the anode aperture (figure 1) and are deflected by the difference in electric field either side of the aperture (Grant & Phillips 1990). For a perfectly smooth sample surface, the electric field between anode and cathode is uniform (except very close to the aperture) and we may trace the electron path classically, whereby the electron moves along a parabolic path as shown in figure 1. If the potential  $V$  is chosen such that the electron has zero energy at the cathode surface, i.e.  $U = -eV$  with electronic charge  $-e$ , the classical turning point is at  $z = L$ . Experimentally it is customary to adjust  $V$  so that  $U < -eV$  and the classical turning point is at  $z = L_M$  as per figure 1, which is located a distance of  $\delta$  above the specimen surface. For simplicity deflections in the  $y$  direction are not shown, but they are treated independently in the same fashion.

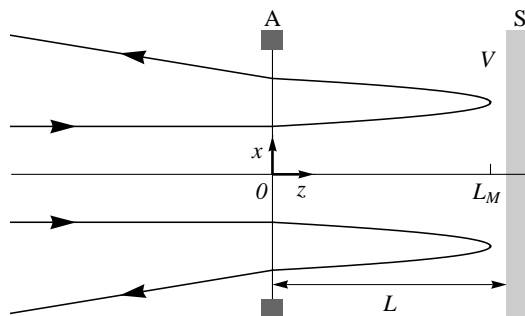


Figure 1. Classical electron trajectories (solid lines), travelling parallel to the optical axis  $z$  along the centre of an anode aperture A, are deflected away from the axis due to the aperture acting as a diverging lens, both upon entering and exiting the anode–cathode region. The aperture separates an electric field free region ( $z < 0$ ) from a constant electric field of  $V/L$  ( $0 \leq z \leq L$ ), where the cathode specimen S is held at potential  $V < 0$  compared to the anode. An electron of energy  $U < -eV$  turns at a distance of  $z = L_M$ . The  $y$  axis extends out of the page. Based on Nepijko & Sedov (1997).



From equation (2.1), the variation in electric potential above the specimen surface can then be expressed as the height function  $H(x, y)$  convolved with a smoothing function,

$$V(x, y, \bar{z}) = \frac{\bar{z}V}{2\pi L} H(x, y) \otimes (x^2 + y^2 + \bar{z}^2)^{-3/2}. \quad (2.4)$$

Physically the smoothing function represents the blurring and softening of the electric field when moving away from the cathode surface. This smoothed potential will therefore extend beyond the  $(x, y)$  range of a localised hill or valley described by  $H(x, y)$ , for example. The additional potential  $V(x, y, \bar{z})$  rapidly approaches zero as  $\bar{z}$  increases away from the surface. The geometrical theory therefore assumes that any change to the electron motion caused by the finite height variation of the cathode occurs very close to the sample surface. In addition, the  $z$ -dimension motion is assumed to be unchanged, so that all of the momentum change in the transverse dimensions  $(x, y)$  occurs very close to the classical turning point at  $z = L_M$ . This amounts to a column approximation, whereby an electron entering the anode at  $(x_0, y_0)$  is affected most strongly by the cathode at  $(3x_0/2, 3y_0/2)$  where it is closest to the surface (see figure 2). The  $x$  and  $y$  derivatives of the potential, integrated along the  $z$  axis for the column  $(3x_0/2, 3y_0/2)$  therefore give the change to the  $x$  and  $y$  velocities respectively. Using the approach of Nepijko & Sedov (1997) and Dyukov *et al.* (1991) the shift of electron position  $S_x, S_y$  on the plane  $z = 4L_M/3 + \Delta f$  due to  $H(x, y)$  for a small defocus  $\Delta f$  of the magnetic objective lens (see figure 3) is given by

$$S_x(x, y, \delta, \Delta f) = \frac{\partial}{\partial x} \frac{\sqrt{L_M}}{\pi} \frac{9\Delta f}{8L_M - 6\Delta f} H(x, y) \otimes ((\delta^2 + x^2 + y^2)^{-3/4} (2E_E(x, y, \delta) - E_K(x, y, \delta))), \quad (2.5)$$

$$S_y(x, y, \delta, \Delta f) = \frac{\partial}{\partial y} \frac{\sqrt{L_M}}{\pi} \frac{9\Delta f}{8L_M - 6\Delta f} H(x, y) \otimes ((\delta^2 + x^2 + y^2)^{-3/4} (2E_E(x, y, \delta) - E_K(x, y, \delta))), \quad (2.6)$$

where

$$E_E(x, y, \delta) = E \left( \frac{1}{2} - \frac{\delta}{2(\delta^2 + x^2 + y^2)^{1/2}} \right), \quad E_K(x, y, \delta) = K \left( \frac{1}{2} - \frac{\delta}{2(\delta^2 + x^2 + y^2)^{1/2}} \right), \quad (2.7)$$

and  $K, E$  respectively denote complete elliptic integrals of the first and second kind (Abramowitz & Stegun 1964; Borwein & Borwein 1987). Here, the magnitude of the electron shift is scaled to the object coordinates (Dyukov *et al.* 1991; Nepijko & Sedov 1997). Note that for  $\Delta f = 0$  the electron shifts are zero, even for a rough surface with non-zero  $H(x, y)$ . The plane  $z = 4L_M/3$  therefore corresponds to the in-focus plane of minimum contrast and a finite defocus  $\Delta f$  is required to obtain image contrast. In the special case where  $\delta = 0$  the electron has sufficient energy to reach the surface, and the shifts simplify to

$$S_x(x, y, \Delta f) = \frac{\partial}{\partial x} \sqrt{\frac{L}{\pi^3}} \frac{9\Delta f}{8L - 6\Delta f} \Gamma(3/4)^2 H(x, y) \otimes (x^2 + y^2)^{-3/4}, \quad (2.8)$$

and similarly for  $S_y$ . For later convenience, we separate the derivatives in  $S_x$  and  $S_y$  from the convolution of the height with the blurring function, introducing the blurred height  $H_B$

$$H_B(x, y, \delta, \Delta f) = \frac{\Delta f}{4L_M - 3\Delta f} H(x, y) \otimes B(x, y, \delta). \quad (2.9)$$

The blurring function is

$$B(x, y, \delta) = \frac{9\sqrt{L_M}}{2\pi} (\delta^2 + x^2 + y^2)^{-3/4} (2E_E(x, y, \delta) - E_K(x, y, \delta)), \quad (2.10)$$

which incorporates the smoothing or softening of the electric field as we move away from the cathode surface (see equation (2.4)), and the resulting interaction of the electron with this field. Note that the factor  $\Delta f/(4L_M - 3\Delta f)$  in equation (2.9) also contributes to the blurring of the height, but it is kept separate from  $B(x, y, \delta)$  for later convenience. Equation (2.5), for example, can then be expressed as

$$S_x(x, y, \delta, \Delta f) = (\partial/\partial x) H_B(x, y, \delta, \Delta f). \quad (2.11)$$

The shifts in electron position defined by equations (2.5) and (2.6) result in a redistribution of intensity on the plane  $z = 4L_M/3 + \Delta f$ . The new intensity distribution can be derived from electron flux conservation giving (Dyukov *et al.* 1991; Nepijko *et al.* 2001b)

$$I(x + S_x, y + S_y) = I_0(x, y) \left/ \left| 1 + \frac{\partial S_x}{\partial x} + \frac{\partial S_y}{\partial y} + \frac{\partial S_x}{\partial x} \frac{\partial S_y}{\partial y} - \frac{\partial S_x}{\partial y} \frac{\partial S_y}{\partial x} \right| \right., \quad (2.12)$$

where  $I_0(x, y)$  is the unperturbed intensity distribution on the plane corresponding to  $H(x, y) = 0$  and is typically taken as unity. Intensity values are therefore calculated from the first spatial derivatives of the shift functions, and these are moved from  $(x, y)$  to  $(x + S_x, y + S_y)$  to evaluate the new intensity distribution.

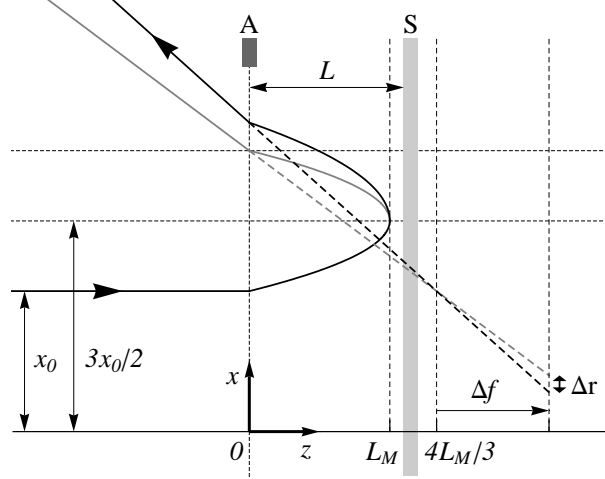


Figure 3. The unperturbed (grey line) and perturbed (black line) electron trajectories are traced back along their apparent straight line paths (dashed lines) to the plane  $z = 4L_M/3 + \Delta f$ . The difference in their position  $\Delta r$  is scaled by the expected magnification of the image on this plane relative to the cathode surface S, to obtain the electron position shifts  $S_x$  and  $S_y$  in the specimen plane.

### 3. Laplacian image contrast in MEM

We now consider the geometrical theory of MEM contrast in the limit of small objective lens defocus and/or slowly varying  $H(x, y)$ , which is an important practical case frequently encountered in MEM. In addition to the assumptions underpinning the geometrical model highlighted in section §2, we require that the derivatives of the blurred height are small,

$$|\partial^2 H_B(x, y, \delta, \Delta f)/\partial x^2| \ll 1, \quad |\partial^2 H_B(x, y, \delta, \Delta f)/\partial y^2| \ll 1, \quad (3.1)$$

which for simplicity we will refer to as

$$|\nabla_{\perp}^2 H_B(x, y, \delta, \Delta f)| \ll 1, \quad (3.2)$$

where  $\nabla_{\perp}^2$  is the transverse Laplacian ( $\partial^2/\partial x^2 + \partial^2/\partial y^2$ ). For a given blurring function  $B$  (equation 2.10) that is determined by the experimental parameters, the required limits of equations (3.1) and (3.2) are met with a sufficiently small objective lens defocus  $\Delta f$  satisfying

$$|\Delta f| < 4L_M/(3 + \max_{x,y} |\nabla_{\perp}^2 H(x, y) \otimes B(x, y, \delta)|), \quad (3.3)$$

where  $\max_{x,y} g(x, y)$  denotes the maximum value of  $g(x, y)$  over the range of points  $(x, y)$ . Conversely, if we require that the maximum  $|\Delta f|$  used in a through-focal series of images is large enough to provide significant image contrast, i.e.  $|\Delta f| > \alpha$  for some distance  $\alpha$ , equation (3.3) demands that  $H(x, y)$  be sufficiently slowly varying to satisfy  $\max_{x,y} |\nabla_{\perp}^2 H(x, y) \otimes B(x, y, \delta)| < -3 + 4L_M/\alpha$ . Note that smoothness of the height profile is not required, only that the Laplacian of the height profile (blurred by the function  $B$ ) and/or the defocus is small enough to satisfy equations (3.1) and (3.2).

Inserting equations (2.9) and (2.11) into equation (2.12), the image intensity can be expressed in terms of the blurred height function as

$$I\left(x + \frac{\partial H_B}{\partial x}, y + \frac{\partial H_B}{\partial y}, \delta, \Delta f\right) = 1/\left|1 + \frac{\partial^2 H_B}{\partial x^2} + \frac{\partial^2 H_B}{\partial y^2} + \left(\frac{\partial^2 H_B}{\partial x^2}\right)\left(\frac{\partial^2 H_B}{\partial y^2}\right) - \left(\frac{\partial^2 H_B}{\partial x \partial y}\right)^2\right|. \quad (3.4)$$

For small defocus  $\Delta f$  and/or slowly varying  $H(x, y)$  ensuring small derivatives of the blurred height (equations (3.1) and (3.2)), the intensity expression is approximated by

$$I(x, y, \delta, \Delta f) \approx 1/|1 + \partial^2 H_B/\partial x^2 + \partial^2 H_B/\partial y^2|. \quad (3.5)$$

This is valid for small shifts in electron trajectory (see equation (2.11)) so that we have neglected the change in  $x, y$  coordinates in  $I(x, y, \delta, \Delta f)$  and derivatives greater than second order. Since the second derivatives in equation (3.5) are much smaller than unity, the denominator will always be positive, so we may remove the absolute value signs and take the binomial approximation of the denominator giving

$$I(x, y, \delta, \Delta f) \approx 1 - (\partial^2/\partial x^2 + \partial^2/\partial y^2)H_B(x, y, \delta, \Delta f) = 1 - \nabla_{\perp}^2 H_B(x, y, \delta, \Delta f). \quad (3.6)$$

The blurred height contains the constant term  $\Delta f/(4L_M - 3\Delta f)$  (see equation (2.9)), and provided we choose a defocus much smaller than the sample-to-anode distance  $L$ , e.g.  $\Delta f = 10^{-5}$  m,  $L = 10^{-3}$  m, this term is approximately proportional to the defocus  $\Delta f$ . So we may write the intensity as

$$I(x, y, \delta, \Delta f) \approx 1 - \Delta f \nabla_{\perp}^2 H(x, y) \otimes B(x, y, \delta)/4L_M, \quad (3.7)$$

where the blurring function  $B(x, y, \delta)$  is given in equation (2.10). This indicates that where the height variation and/or defocus is small enough to satisfy equation (3.2), the image intensity on the ‘out of focus’ plane  $z = 4L_M/3 + \Delta f$  is the Laplacian image of the height function, blurred with a function  $B(x, y, \delta)/4L_M$  to account for the interaction of the electron with the electric field above the cathode surface. In the regime where this approximate expression is valid, we may therefore interpret MEM image contrast to be created solely by the transverse second derivatives (curvature) of the surface height variation, smoothed by a blurring function. This is an important result for the intuitive interpretation of MEM contrast of surface topography.

Laplacian imaging is widely encountered in many contexts ranging from X-Ray imaging (Paganin 2006) to oriental magic mirrors (Berry 2006) and their modern equivalent in Makyoh topography (Riesz 2000). It is also known as out of focus contrast in transmission electron microscopy (TEM) of thin specimens (Lynch *et al.* 1975; Cowley 1995; Spence 2003). The applicability of the Laplacian imaging formalism to MEM under particular conditions considerably simplifies image interpretation as we will discuss in §4.

#### 4. Intuitive interpretation of MEM image contrast

As an application of Laplacian imaging in MEM we apply the technique to investigate Ga droplets on GaAs (001). This system is known to exhibit droplet surface dynamics which obey an unusual temperature dependence (Tersoff *et al.* 2009). As Ga droplets move on the rough GaAs (001) surface they leave behind smooth trails as shown in the atomic force microscope (AFM) image in figure 4. Outside of the trail there is significant surface roughness and we obtain a mean trail profile by averaging the surface height along the  $y$  axis in the framed region shown in figure 4. The resulting averaged cross-sectional profile, contained in figure 5(a), is 1.9  $\mu\text{m}$  wide and 14 nm deep. For the range of droplet sizes studied by AFM we find that the width to depth ratio of the trails is approximately constant ( $\sim 140$ ). With  $L = 2$  mm,  $\delta = 40$  nm,  $V = -20000.4$  V and  $U = 20$  keV, and for the droplet trails considered here we find that  $\max_{x,y} |\nabla_{\perp}^2 H(x, y) \otimes B(x, y, \delta)| \approx 35 \text{ m}^{-1}$  or lower, so that the condition of equation (3.3) requires that  $|\Delta f| < 200 \mu\text{m}$  in order to satisfy  $|\nabla_{\perp}^2 H_B| \ll 1$ . Therefore the assumptions underpinning a Laplacian contrast interpretation as outlined in §3 are valid and we choose the droplet trails as convenient test objects for Laplacian MEM imaging. Note that the height of the droplet itself (denoted ‘D’ in figure 4) is too large (0.3  $\mu\text{m}$  above the cathode surface) to satisfy the assumption that changes in the  $z$ -component of the electron motion can be neglected. Therefore, it is inappropriate to apply the geometrical theory and a Laplacian interpretation in this case.

It is experimentally impractical to obtain both AFM and MEM images of the same droplet trail, therefore we consider only the general features of the AFM data of figure 4. Specifically, we ignore the significant surface roughness outside the trail, still present due to the limited area available for averaging, which will inevitably lead to strong intensity fluctuations in MEM images. So rather than use the AFM data directly in the Laplacian MEM method, in this example we instead model the trail using a height function  $H(x)$  which is the sum of two inverse tangent functions,

$$H(x) = \frac{T}{\pi} \left( \tan^{-1} \left( \frac{x-R}{O} \right) - \tan^{-1} \left( \frac{x+R}{O} \right) \right). \quad (4.1)$$

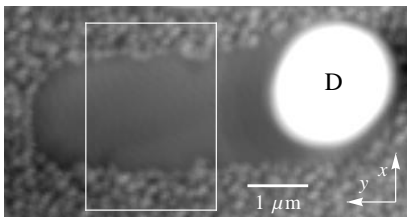


Figure 4. Atomic Force Microscope (AFM) image of a trail left by a moving Ga droplet marked D on a GaAs (001) surface. The region inside the box is integrated along  $y$  to obtain a one dimensional height profile in  $x$ , shown in figure 5(a).

Here  $T$  sets the maximum depth of the trail,  $R$  is the distance of the side from the centre, and  $O$  sets the steepness of the trail edge, e.g. for  $O = 0.1 \mu\text{m}$ , 80% of the variation of the trail edge about its midpoint occurs over a distance of  $0.5 \mu\text{m}$  (see figure 5(a)). A background linear variation in  $x$  in the AFM data was ignored when fitting the height function (the variation was removed to give figure 5(a)), as we consider only the general features of the AFM data in this example. Note that the Laplacian contrast method is insensitive to linear variations in  $x$  that span the entire AFM image, since the second derivative of the height dominates the image contrast. However a linear variation that begins and/or ends within the data range will introduce a discontinuity where the linear variation starts and/or finishes, which has a non-zero second derivative and will contribute to the image intensity.

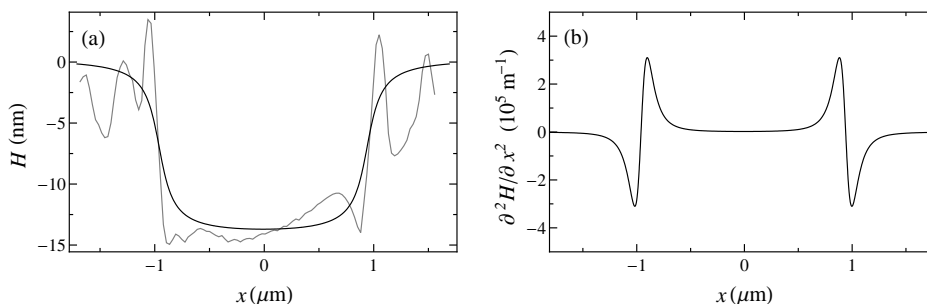


Figure 5. (a) Averaged one dimensional profile of a droplet trail on the cathode surface (grey line), along with the simplified height function  $H(x)$  (black line) fitted using equation (4.1) with  $R = 0.95 \mu\text{m}$ ,  $O = 0.1 \mu\text{m}$ ,  $T = 15 \text{ nm}$ . (b) Second spatial derivative of  $H(x)$  which provides the key qualitative features of the MEM image.

Fitting equation (4.1) to the general features of the averaged cross-sectional profile gives a simplified model of the trail height function (see figure 5(a)). As indicated in figure 5(a), we choose a broad trail edge to account for the width variation and surface roughness evident in figure 4. As discussed earlier, a major advantage of Laplacian imaging contrast is its ease of interpretation via equation (3.7). It is therefore straightforward to predict the general features of the image contrast of a droplet trail from the second derivative of the model trail height function contained in figure 5(a). This is shown in figure 5(b) and indicates that the MEM image should contain a bright and dark contrast band in the vicinity of the trail edges, along with constant intensity in the centre of the trail. We emphasise that such a first order interpretation of MEM contrast in terms of surface curvature is quite general and independent of the surface profile, provided the Laplacian imaging theory is valid. This has important practical value for studies of surface phenomena using MEM.

In practice, equation (3.7) indicates that the second derivative of  $H$  is softened or smoothed by convolution with the blurring function  $B(x, y, \delta)$  in forming the image, physically accounting for the electron interacting with the electric field above the cathode. The defocus  $\Delta f$  will affect both the magnitude and the sign of the contrast peaks. A qualitative comparison of simulated Laplacian contrast images, based on equation (3.7), with experimental MEM images of a trail similar to that in figure 4 is shown in figure 6 for negative, zero and positive defocus values. Although the surface roughness outside the trail region results in significant contrast

fluctuations, it can be seen that the main features of the experimental image through-focus sequence are consistent with Laplacian imaging theory for a generalised trail profile. A more complex or realistic height profile, e.g. that recovered in §7 in figure 9(b), can account for image features caused by surface roughness. Figure 7 compares simulations and experimental profiles of the MEM image intensity for positive and negative defocus values. The latter profiles have been integrated over the two dimensional panel region on figure 6, parallel to the trail edges, to reduce the intensity fluctuations caused by the surface roughness. The good agreement in both cases again illustrates the applicability of Laplacian imaging which facilitates the interpretation of image contrast in terms of surface curvature.

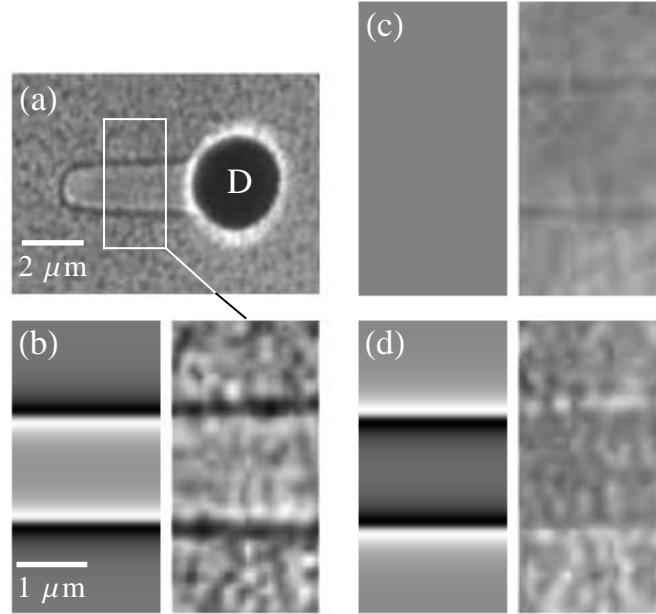


Figure 6. (a) MEM image of a moving Ga droplet D and the trail left on a GaAs (001) surface. Imaging conditions were  $V = -20000.4$  V,  $U = 20$  keV and  $L = 0.002$  m giving  $\delta = 40$  nm. Comparison of MEM images and simulations using equation (3.7) of the trail region contained in the frame in (a) are shown for (b) negative defocus ( $\Delta f = -15$   $\mu\text{m}$ ), (c) approximately zero defocus and (d) positive defocus ( $\Delta f = 15$   $\mu\text{m}$ ). The trail height function was approximated using equation (4.1) for  $R = 0.83$   $\mu\text{m}$ ,  $O = 0.1$   $\mu\text{m}$ ,  $T = 13$  nm.

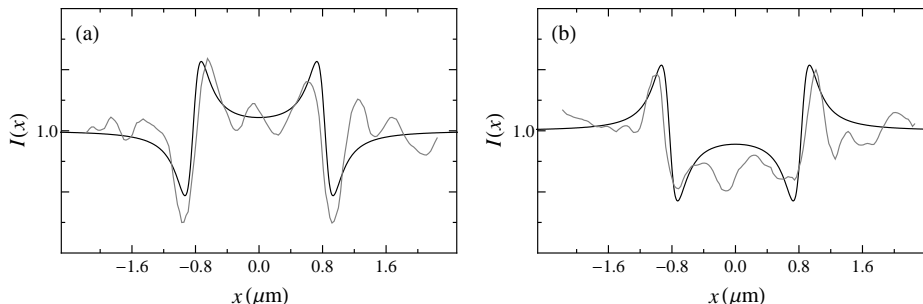


Figure 7. Comparison of simulated Laplacian contrast images (black lines) with experimental MEM intensity profiles of a droplet trail (grey lines). The experimental MEM intensity profiles were obtained by spatially averaging the intensities parallel to the trail edge over the two dimensional regions in figure 6(b) and (d). (a)  $\Delta f = -15 \mu\text{m}$ , (b)  $\Delta f = 15 \mu\text{m}$ . The trail height function was approximated using equation (4.1) for  $R = 0.83 \mu\text{m}$ ,  $O = 0.1 \mu\text{m}$ ,  $T = 13 \text{nm}$ . The grey scale intensity values in the experimental images were scaled to match the vertical axis of the simulations, allowing a qualitative comparison.

## 5. Comparison of the Laplacian and geometrical theory

It is important to establish and confirm the domain of validity of Laplacian imaging theory. We therefore compare image simulations based on the height profile of the droplet trail shown in figure 5(a), using the geometrical (equation (3.4)) and the approximate Laplacian contrast approaches (equation (3.7)). As shown in figure 8(a) for defocus  $\Delta f = -15 \mu\text{m}$  and classical turning point  $\delta = 40 \text{nm}$  from the cathode surface, the two methods agree very closely. Increasing the magnitude of the defocus and/or decreasing the turning point distance will increase the blurred height  $H_B$  and its derivatives. This weakens the validity of the assumption made in the Laplacian contrast method that  $|\nabla_{\perp}^2 H_B| \ll 1$ , and we therefore see an increased discrepancy between the image contrast generated from the Laplacian contrast and geometrical imaging simulation methods (figure 8(b)). Conversely, reducing the magnitude of the defocus and/or increasing the turning distance improves the agreement between the two approaches as expected.

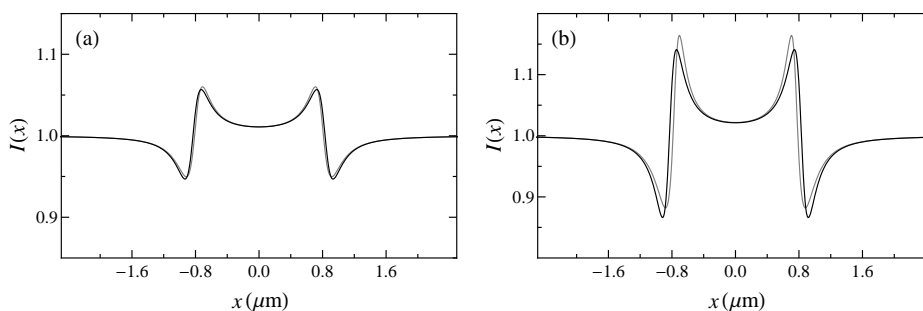


Figure 8. Comparison of the one dimensional intensity profile predicted using the geometrical treatment (grey line) with the Laplacian contrast method (black line), for the droplet trail height profile of figure 5, using  $R = 0.83 \mu\text{m}$ ,  $O = 0.1 \mu\text{m}$ ,  $T = 13 \text{nm}$ . (a)  $\Delta f = -15 \mu\text{m}$ ,  $\delta = 40 \text{nm}$ , (b)  $\Delta f = -30 \mu\text{m}$  and  $\delta = 20 \text{nm}$ .

## 6. Extensions of the Laplacian imaging theory of MEM contrast

Having established the applicability of Laplacian imaging theory to MEM we now utilise previous studies to extend our analysis. In particular, Laplacian contrast is also known as out of focus contrast in TEM of thin

specimens (Lynch *et al.* 1975; Cowley 1995; Spence 2003), and we can utilise this formalism to include the effects of spherical and chromatic aberration. These aberrations are an intrinsic part of an MEM imaging system and limit resolution (Rempfer & Griffith 1992). Since a Laplacian contrast interpretation is applicable to imaging objects at high resolution provided  $|\nabla_{\perp}^2 H_B| \ll 1$ , it is important to incorporate such effects into the imaging theory. The expression for TEM out of focus contrast for a thin uniformly-illuminated specimen is (Lynch *et al.* 1975; Cowley 1995; Spence 2003)

$$I(x, y, z = z_0 + \Delta f) = 1 - k^{-1} \Delta f \nabla_{\perp}^2 \phi, \quad (6.1)$$

for a defocus  $\Delta f$  and electron wavenumber  $k = 2\pi/\lambda$ . The electron phase change through the specimen  $\phi$  is inversely proportional to the local electron wavelength  $\lambda$  so that the wavelength dependence factors out in equation (6.1) and so it is possible to extrapolate the wavelength to zero (cf. equation (6.4)).

We note that equation (6.1) is identical to the Laplacian theory description of MEM contrast (equation (3.7)) provided the phase of the wave function is

$$\phi(x, y, \delta) = \frac{k}{\Delta f} H_B(x, y, \delta, \Delta f). \quad (6.2)$$

We may view this as the effective phase variation of an electron wave post interaction with the cathode sample surface, which has been scaled up to the vacuum or post anode aperture energy. Equation (6.1) therefore describes the out of focus MEM contrast in the defocused image plane  $z = 4L_M/3 + \Delta f$ .

Lynch *et al.* (1975) extended the TEM out of focus expression to include the effects of spherical aberration, which depends on the bi-Laplacian or iterated Laplacian ( $\nabla_{\perp}^4 \equiv \nabla_{\perp}^2 \nabla_{\perp}^2$ ) of the phase variation  $\phi$ , scaled by the spherical aberration coefficient  $C_S$ ,

$$I(x, y, \delta, \Delta f) \approx 1 - \frac{\Delta f}{k} \nabla_{\perp}^2 \phi(x, y, \delta) + \frac{C_S}{2k^3} \nabla_{\perp}^4 \phi(x, y, \delta). \quad (6.3)$$

We may recast this equation using equation (6.2) to give

$$I(x, y, \delta, \Delta f) \approx 1 - \nabla_{\perp}^2 H_B(x, y, \delta, \Delta f) + \frac{C_S}{2\Delta f k^2} \nabla_{\perp}^4 H_B(x, y, \delta, \Delta f), \quad (6.4)$$

which extends our Laplacian contrast expression to include spherical aberration. For the resolutions employed in the study of droplet trails and with  $C_S$  values derived by Rempfer & Griffith (1992) we have found that including spherical aberration provides less than a one percent change in the simulated intensity variation. However, we anticipate that the inclusion of spherical aberration will be of benefit in simulating higher resolution images of surface objects within the domain of validity of Laplacian imaging.

We may also extend the Laplacian contrast method to include the effects of a finite energy spread in the electron beam, which causes chromatic aberration in the image intensity. A distribution in energy  $D(U)$  varies the classical turning point  $\delta$ , via

$$\delta = L \left( 1 + \frac{U}{eV} \right), \quad (6.5)$$

where the cathode surface is kept at a potential of  $V < 0$ . The distribution in turning point  $D(\delta)$  can then be obtained from the energy distribution, e.g.  $D(\delta) \approx D(U) dU/d\delta$ . Following the approach of Fejes (1977) we incoherently average over the distribution, summing up the contributions of each intensity (equation (3.7)) weighted by the distribution function,

$$I_C(x, y, \Delta f) = \int I(x, y, \delta, \Delta f) D(\delta) d\delta \approx \int D(\delta) d\delta - \nabla_{\perp}^2 \int H_B(x, y, \delta, \Delta f) D(\delta) d\delta. \quad (6.6)$$

Since the turning distance  $\delta$  only appears in the blurring function, in effect we may replace the monochromatic blurring function  $(\Delta f/(4L_M - 3\Delta f))B(x, y, \delta)$  with the chromatically averaged  $B_C(x, y, \delta_0, \Delta f)$ , given by

$$B_C(x, y, \delta_0, \Delta f) = \int \frac{\sqrt{L - \delta}}{\pi} \frac{9(\Delta f + 2(\delta - \delta_0))}{8(L - \delta) - 6(\Delta f + 2(\delta - \delta_0))} (\delta^2 + x^2 + y^2)^{-3/4}$$

$$\times (2E_E(x, y, \delta) - E_K(x, y, \delta))D(\delta)d\delta, \quad (6.7)$$

with a defocus of  $\Delta f + 2(\delta - \delta_0)$  to ensure that each intensity corresponds to the plane  $z = 4(L - \delta_0)/3 + \Delta f$ , and where  $\delta_0$  is the mean of the distribution. Chromatic aberration, then, can be incorporated into the approximate method by adjusting the blurring function, in essence averaging over several blurring functions to obtain the effective blurring function  $B_C$ . With a normalized distribution we then have

$$I_C(x, y, \delta_0, \Delta f) \approx 1 - \nabla_{\perp}^2 H(x, y) \otimes B_C(x, y, \delta_0, \Delta f). \quad (6.8)$$

As with spherical aberration, chromatic aberration has a small effect on simulating the MEM image contrast of the droplet trails (less than one percent as expected). This is true for a Gaussian energy distribution with a typical full-width-half-maximum equal to 0.3 eV for a Schottky field emission source and a variety of mean  $\delta_0$  values. However, we would again envisage that equation (6.8) will be of value for the study of surface objects at high resolution within the Laplacian imaging regime of  $|\nabla_{\perp}^2 H_B| \ll 1$ .

## 7. Inverse problem of Laplacian MEM imaging

Many of the geometrical treatments consider the important ‘inverse problem’ of MEM imaging, whereby image contrast is analysed to estimate the perturbed electric potential and/or the height variation of the specimen (Luk’yanov *et al.* 1974; Dyukov *et al.* 1991; Nepijko & Sedov 1997; Nepijko & Schönense 2010). The inverse problem has also been explored in other areas of surface electron microscopy such as LEEM (Yu *et al.* 2010). In the Laplacian theory of MEM contrast this may be achieved in a very straightforward fashion using the Fourier derivative theorem (Cowley 1995; Paganin 2006) to convert between spatial derivatives and Fourier space coordinates,

$$\mathcal{F}(I(x, y, \delta, \Delta f) - 1) \approx \mathcal{F}(-\nabla_{\perp}^2 H_B(x, y, \delta, \Delta f)) = (k_x^2 + k_y^2) \mathcal{F}H_B(x, y, \delta, \Delta f). \quad (7.1)$$

Here  $k_x$  and  $k_y$  are the Fourier space coordinates corresponding to real space coordinates  $x$  and  $y$  respectively,  $\mathcal{F}$  is the Fourier transform with respect to  $x$  and  $y$ , and  $\mathcal{F}^{-1}$  is the corresponding inverse Fourier transform. We therefore have (Gureyev & Nugent 1997)

$$H_B(x, y, \delta, \Delta f) \approx \mathcal{F}^{-1}((k_x^2 + k_y^2)^{-1} \mathcal{F}(I(x, y, \delta, \Delta f) - 1)), \quad (7.2)$$

which in principle allows the recovery of the blurred height function from a single image, facilitating the analysis of MEM movie dynamics (Tersoff *et al.* 2009). This expression bears a strong resemblance to phase retrieval via the transport of intensity equation (Teague 1983; Gureyev & Nugent 1997; Paganin & Nugent 1998), whereby a phase contrast image may be used to recover the original phase object.

Upon obtaining the blurred height function, we then deconvolve to obtain the height function, for example via equation (2.9) using the convolution theorem (Cowley 1995)

$$H(x, y, \delta) = \frac{(4L_M - 3\Delta f)}{2\pi\Delta f} \mathcal{F}^{-1} \left( \frac{\mathcal{F}(H_B(x, y, \delta, \Delta f))}{\mathcal{F}(B(x, y, \delta))} \right). \quad (7.3)$$

If the value of the defocus is not known, we can only recover the height to within the scaling factor  $(4L_M - 3\Delta f)/\Delta f$ . Here we present two preliminary examples in one dimension of the inverse problem of Laplacian MEM imaging. Figure 9(a) shows the recovered height using equations (7.3) and (7.3) from the simulated MEM images shown in figure 7. The recovered height is in very good agreement with the ideal height profile of equation (4.1), also shown in figure 9(a).

Figure 9(b) shows an average of the recovered heights from the experimental MEM intensity profiles of figure 7 to within a scaling factor, as the specific defocus values were not known. The general features of the recovered height are in good agreement with the ideal height profile, with discrepancies largely due to the surface roughness evident in the recovered height profile. Using equation (3.7) to simulate the Laplacian image contrast of the recovered height profile of figure 9(b), we found that the normalised root mean squared difference between the simulated intensity and the measured MEM image intensity profiles (figure 7) was 3 % and 10 % for the negative and positive defocus images respectively.

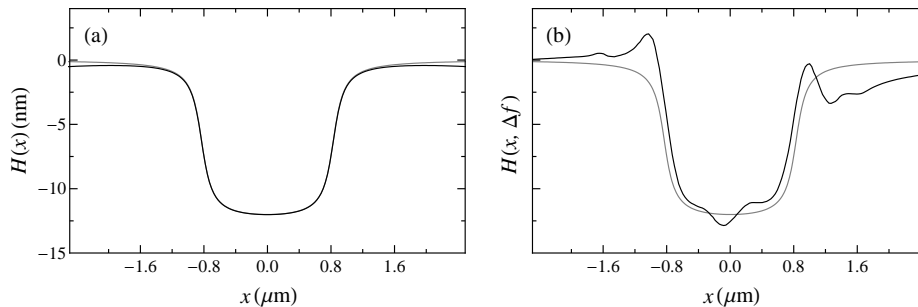


Figure 9. Recovered height profiles of the droplet trail (black lines) using equations (7.3) and (7.3) compared to the ideal height profile (grey lines) of equation (4.1) with  $R = 0.83 \mu\text{m}$ ,  $O = 0.1 \mu\text{m}$ ,  $T = 13 \text{ nm}$ . (a) the recovered height from the simulated MEM intensity profiles for the ideal height (black lines in figure 7), using  $\Delta f = -15 \mu\text{m}$ . (b) average of the recovered height profiles (black line) of the experimental MEM images (grey lines in figure 7). The recovered height  $H(x, \Delta f) = H(x)\Delta f / (4L_M - 3\Delta f)$  includes the scaling factor  $\Delta f / (4L_M - 3\Delta f)$  since  $\Delta f$  in each image was unknown.

## 8. Conclusions

We have demonstrated that Laplacian imaging theory can be applied to MEM imaging of surface topography (or equivalently surface potentials) provided the height function describing the surface topography is slowly spatially varying and/or the objective lens defocus is small. Under such conditions, image contrast is primarily caused by the Laplacian of small height or potential variations across a sample surface. This contrast is blurred due to the interaction of the electrons with the electrical potential away from the surface. However, the method facilitates the rapid and intuitive interpretation of image contrast in terms of surface topographic or potential variations. The approach can be readily extended to include spherical and chromatic aberration. Finally, we have demonstrated that the Laplacian imaging theory forms a convenient basis for the solution of the inverse problem in MEM.

We are grateful to Rod Mackie for technical support. S.M.K. acknowledges funding from the J. L. William Bequest. D.M.P., W.X.T. and D.E.J. acknowledge funding from the Australian Research Council.

## References

- Abramowitz, M. & Stegun, I. A. 1964 *Handbook of mathematical functions with formulas, graphs, and mathematical tables*, second printing, Ch. 17, pp. 589–592, Washington: United States Department of Commerce and National Bureau of Standards (also available online).
- Barnett, M. E. & Nixon, W. C. 1967a A mirror electron microscope using magnetic lenses *J. Sci. Instrum.* **44**, 893–897. (DOI 10.1088/0950-7671/44/11/302).
- Barnett, M. E. & Nixon, W. C. 1967b Electrical contrast in mirror electron microscopy *Optik* **26**, 310–325.
- Bauer, E. 1985 The resolution of the low energy electron reflection microscope *Ultramicroscopy* **17** 51–56. (DOI 10.1016/0304-3991(85)90176-7).
- Bauer, E. 1994 Low energy electron microscopy *Rep. Prog. Phys.* **57** 895–938. (DOI 10.1088/0034-4885/57/9/002).
- Bauer, E. 1998 LEEM basics *Surf. Rev. Lett.* **5** 1275–1286. (DOI 10.1142/S0218625X98001614).
- Berry, M. V. 2006 Oriental magic mirrors and the Laplacian image *Eur. J. Phys.* **27** 109–118. (DOI 10.1088/0143-0807/27/1/012).
- Bok, A. B. 1978 Mirror electron microscopy theory and applications. In *Diffraction and imaging techniques in material science* (eds S. Amelinckx, R. Gevers & J. Van Landuyt), 2nd rev. edn., pp. 761–788, Amsterdam: North-Holland.
- Borwein, J. M. & Borwein, P. B. 1987 *Pi and the AGM, a study in analytic number theory and computational complexity*, vol. 4, pp. 7–9, New York: John Wiley & Sons.
- Boudjelkha, M. T. & Diaz, J. B. 1972 Half space and quarter space Dirichlet problems for the partial differential equation *Applicable Analysis* **1** 297–324. (DOI 10.1080/00036817208839020).
- Cowley, J. M. 1995 *Diffraction physics*, 3rd rev. edn., pp. 26–35, 59–63, Amsterdam: North-Holland.
- Dyukov, V. G., Nepijko, S. A. & Sedov, N. N. 1991 *Electron microscopy of local potentials*, pp. 10–12, 28–35, 45–51, 63–66, 73–76, Kiev: Naukova Dumka (in Russian).
- Fejes, P. L. 1977 Approximations for the calculation of high-resolution electron-microscope images of thin films *Acta Cryst.* **A33** 109–113. (DOI 10.1107/S0567739477000230).

- Godehardt, R. 1995 Mirror electron microscopy *Adv. Imag. Elect. Phys.* **94** 81–150. (DOI 10.1016/S1076-5670(08)70144-7).
- Grant, I. S. & Phillips, W. R. 1990 *Electromagnetism*, 2nd edn., pp. 100–103, Chichester: John Wiley & Sons.
- Gureyev, T. E. & Nugent, K. A. 1997 Rapid quantitative phase imaging using the transport of intensity equation *Opt. Commun.* **133** 339–346. (DOI 10.1016/S0030-4018(96)00454-3).
- Hermans, A. J. & Petterson, J. A. 1970 A quantum mechanical treatment of the mirror electron microscope *J. Eng. Math.* **4** 141–154. (DOI 10.1007/BF01535086).
- Jesson, D. E., Pavlov, K. M., Morgan, M. J. & Usher, B. F. 2007 Imaging surface topography using Lloyd’s mirror in photoemission electron microscopy *Phys. Rev. Lett.* **99** 016103. (DOI 10.1103/PhysRevLett.99.016103).
- Kennedy, S. M., Jesson, D. E., Morgan, M. J., Smith, A. E. & Barker, P. F. 2006 Phase sensitivity of slow electrons to interactions with weak potentials *Phys. Rev. A* **74** 044701. (DOI 10.1103/PhysRevA.74.044701).
- Luk’yanov, A. E., Spivak, G. V. & Gvozdover, R. S. 1974 Mirror electron microscopy *Sov. Phys. Usp.* **16** 529–552. (DOI 10.1070/PU1974v016n04ABEH005299).
- Lynch, D. F., Moodie, A. F. & O’Keefe, M. A. 1975 n-beam lattice images. V. The use of the charge-density approximation in the interpretation of lattice images *Acta Cryst.* **A31** 300–307. (DOI 10.1107/S0567739475000642).
- Nepijko, S. A. & Schönhense, G. 2010 Measurement of potential distribution function on object surface by using an electron microscope in the mirror operation mode *J. Microsc.* **238** 90–94. (DOI 10.1111/j.1365-2818.2009.03340.x).
- Nepijko, S. A. & Sedov, N. N. 1997 Aspects of mirror electron microscopy *Adv. Imag. Elect. Phys.* **102** 273–323. (DOI 10.1016/S1076-5670(08)70125-3).
- Nepijko, S. A., Sedov, N. N., Schmidt, O., Schönhense, G., Bao, X. & Huang, W. 2001a Imaging of three-dimensional objects in emission electron microscopy *J. Microsc.* **202** 480–487. (DOI 10.1046/j.1365-2818.2001.00846.x).
- Nepijko, S. A., Sedov, N. N. & Schönhense, G. 2001b Peculiarities of imaging one- and two-dimensional structures using an electron microscope in the mirror operation mode *J. Microsc.* **203** 269–276. (DOI 10.1046/j.1365-2818.2001.00895.x).
- Nepijko, S. A., Gloskovskii, A., Sedov, N. N. & Schönhense, G. 2003 Measurement of the electric field distribution and potentials on the object surface in an emission electron microscope without restriction of the electron beams *J. Microsc.* **211** 89–94. (DOI 10.1046/j.1365-2818.2003.01199.x).
- Nepijko, S. A., Marx, G. K. L. & Schönhense, G. 2007 Quantitative determination of magnetic fields on object surfaces via photoemission electron microscopy without restriction of the electron beam *Nucl. Instr. and Meth. in Phys. Res. B* **264** 194–200. (DOI 10.1016/j.nimb.2007.08.076).
- Paganin, D. M. & Nugent, K. A. 1998 Noninterferometric phase imaging with partially coherent light *Phys. Rev. Lett.* **80** 2586–2589. (DOI 10.1103/PhysRevLett.80.2586).
- Paganin, D. M. 2006 *Coherent X-ray optics*, pp. 278–284, 295–301, 395–396, New York: Oxford University Press.
- Polozhiy, G. N. 1967 *Equations of mathematical physics*, pp. 62–64, 149, New York: Hayden Book Company.
- Press, W. H., Teukolsky, S. A., Vetterling, W. T. & Flannery, B. P. 2007 *Numerical recipes, the art of scientific computing*, 3rd edn., pp. 600–604, Cambridge: Cambridge University Press.
- Rempfer, G. F. & Griffith, O. H. 1992 Emission microscopy and related techniques: resolution in photoelectron microscopy, low energy electron microscopy and mirror electron microscopy *Ultramicroscopy* **47** 35–54. (DOI 10.1016/0304-3991(92)90184-L).
- Riesz, F. 2000 Geometrical optical model of the image formation in Makyoh (magic-mirror) topography *J. Phys. D: Appl. Phys.* **33** 3033–3040. (DOI 10.1088/0022-3727/33/23/305).
- Sedov, N. N. 1970 Théorie quantitative des systèmes en microscopie électronique à balayage, à miroir et à émission. *J. Microscopie* **9** 1–26.
- Slezák, J., Ondřejček, M., Chvoj, Z., Cháb, V., Conrad, H., Heun, S., Schmidt, Th., Ressel, B. & Prince, K. C. 2000 Surface diffusion of Au on Si(111): a microscopic study *Phys. Rev. B* **61** 16121–16128. (DOI 10.1103/PhysRevB.61.16121).
- Shimakura, T., Takahashi, Y., Sugaya, M., Ohnishi, T., Hasegawa, M., Ohta, H. 2008 Mirror electron microscope for inspecting nanometer-sized defects in magnetic media *Microelectron. Eng.* **85** 1811–1814. (DOI 10.1016/j.mee.2008.05.018).
- Someya, T. & Kobayashi, J. 1974 Quantitative application of electron-mirror microscopy to the determination of pure shear of ferroelectric  $\text{Gd}_2(\text{MoO}_4)_3$  *Phys. Stat. Sol. (a)* **26** 325–336. (DOI 10.1002/pssa.2210260134).
- Speake, C. C. & Trenkel, C. 2003 Forces between conducting surfaces due to spatial variations of surface potential *Phys. Rev. Lett.* **90** 160403. (DOI 10.1103/PhysRevLett.90.160403).
- Spence, J. C. H. 2003 *High-resolution electron microscopy*, 3rd edn., Ch. 3, Oxford: Oxford University Press.
- Świąch, W., Rausenberger, B., Engel, W., Bradshaw, A. M. & Zeitler, E. 1993 In-situ studies of heterogeneous reactions using mirror electron microscopy *Surf. Sci.* **294** 297–307. (DOI 10.1016/0039-6028(93)90116-2).
- Tang, W. X., Jesson, D. E., Pavlov, K. M., Morgan, M. J. & Usher, B. F. 2009 Ga droplet morphology on GaAs(001) studied by Lloyd’s mirror photoemission electron microscopy *J. Phys.: Condens. Matter* **21** 314022. (DOI 10.1088/0953-8984/21/31/314022).

- M. R. 1983 Deterministic phase retrieval: a Green's function solution *J. Opt. Soc. Am.* **73** 1434–1441. (DOI 10.1364/JOSA.73.001434).
- Tersoff, J., Jesson, D. E. & Tang W. X. 2009 Running droplets of Ga from evaporation of GaAs *Science* **324** 236–238. (DOI 10.1126/science.1169546).
- Yu, R. P., Kennedy, S. M., Paganin, D. M. & Jesson, D. E. 2010 Phase retrieval low energy electron microscopy *Micron* **41** 232–238. (DOI 10.1016/j.micron.2009.10.010).

# Laplacian image contrast in mirror electron microscopy. Addendum

BY S. M. KENNEDY, C. X. ZHENG, W. X. TANG, D. M. PAGANIN, D. E. JESSON†

*School of Physics, Monash University, Victoria 3800, Australia.*

We extend the theory of Laplacian image contrast in mirror electron microscopy (MEM) to the case where the sample is illuminated by a parallel, collimated beam. This popular imaging geometry corresponds to a modern low energy electron microscope equipped with a magnetic objective lens. We show that within the constraints of the relevant approximations, the results for parallel illumination differ only negligibly from diverging MEM specimen illumination conditions.

**Keywords:** Mirror electron microscopy (MEM), Laplacian image contrast, phase contrast

## 1. Introduction

A recent paper by Kennedy *et al.* (2010) describes how, under certain conditions, images formed in mirror electron microscopy can be interpreted in terms of the Laplacian of small height or potential variations across a sample surface. The specific MEM imaging geometry considered conforms to an experimental configuration where the incident electron beam is slightly divergent as a result of the anode aperture. This arrangement has been considered by several authors (Dyukov *et al.* 1991; Nepijko & Sedov 1997; Nepijko *et al.* 2001*a, b*, 2003, 2007; Nepijko & Schönhense 2010). It is a subset of non-parallel MEM specimen illumination considered in the literature (Barnett & Nixon 1967*a*; Luk'yanov *et al.* 1974; Someya & Kobayashi 1974; Dupuy *et al.* 1984; Godehardt 1995). Modern low energy electron microscopes are, however, equipped with a magnetic objective lens and it is customary to slightly converge the incident illumination to compensate for the diverging effect of the anode aperture, resulting in collimated illumination of the sample (Altman 2010; Tromp *et al.* 2010), within the domain of validity of the aperture lens approximation. This paper therefore considers how MEM Laplacian imaging theory (Kennedy *et al.*, 2010) is modified by a parallel or collimated illumination geometry. We show, that in the limit of small objective lens defocus, the results converge to the original divergent illumination geometry considered by Kennedy *et al.* (2010) so that the conclusions drawn there remain valid.

## 2. Comparison of divergent and parallel MEM illumination geometries

An electrostatic MEM immersion lens is shown schematically in figure 1, which illustrates the divergent MEM illumination geometry considered by Kennedy *et al.* (2010), Luk'yanov *et al.* (1974), Dyukov *et al.* (1991), Godehardt (1995), Nepijko & Sedov (1997), Nepijko *et al.* (2001*a, b*, 2003, 2007), Nepijko & Schönhense (2010). Here, an electron beam of energy  $U$  travels parallel to the optical axis  $z$  of the immersion lens and passes through the grounded anode aperture A. The overall effect of the electric field in the vicinity of the grounded aperture is approximated by replacing the aperture with a thin diverging lens (Grant & Phillips 1990; Lenc & Müllerová 1992; Rempfer & Griffith 1992; Nepijko & Sedov 1997; Kennedy *et al.*, 2010), so that the electron beam is deflected away from the optical axis  $z$ . The electron beam is therefore diverging as it interacts with the electric field above the specimen surface C, which is located a distance of  $L$  from the anode and acts as the cathode of the immersion objective lens (Barnett & Nixon 1967*b*; Luk'yanov *et al.* 1974; Bok 1978; Bauer 1985, 1998; Kennedy *et al.*, 2010). The cathode C is held at a negative potential  $V < -U/e < 0$  relative to the grounded anode, where  $-e$  is the electronic charge, so that the electron beam is reflected in the vicinity of  $z = L_M$ , a distance of  $\delta$  above the specimen surface,

$$L_M = L - \delta = -LU/eV, \quad (2.1)$$

and the returning electron beam is further deflected as it exits the anode aperture. For a perfectly flat, equipotential specimen, an electron that enters the anode aperture at  $(x_0, y_0)$  is closest to the cathode surface at  $(3x_0/2, 3y_0/2)$ .

† Author for correspondence (██████████).

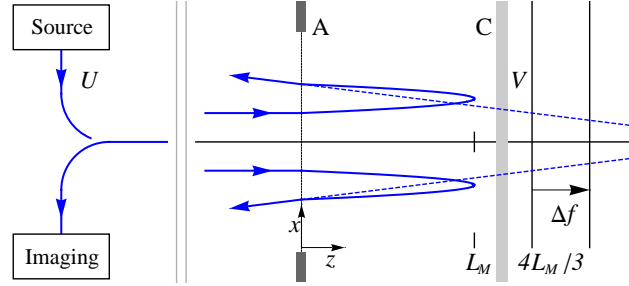


Figure 1. Classical electron trajectories (solid lines), travelling parallel to the optical axis  $z$  in the electric field free region ( $z < 0$ ) along the centre of an anode aperture A. The trajectories are deflected away from the  $z$  axis both upon entering and exiting the anode–cathode region, due to the distortion of the electric field in the vicinity of the anode aperture A. This effect is approximated by treating the aperture A as a diverging lens (Grant & Phillips 1990; Lenc & Müllerová 1992; Rempfer & Griffith 1992; Nepijko & Sedov 1997; Kennedy *et al.*, 2010). This deflection results in diverging illumination of the cathode specimen C, which is held at the potential  $V < 0$  compared to the anode, so that an electron of energy  $U < -eV$  turns at a distance of  $z = L_M$ . The  $y$  axis extends out of the page. Based on Kennedy *et al.* (2011).

To a good approximation, the magnetic imaging part of the objective lens can be considered separately to the electrostatic MEM immersion lens of figure 1 (Bauer 1985, 1994). A virtual image is formed by retracing the exiting electron trajectories at  $z = 0$  to the plane at  $z = \Delta f + 4L_M/3$ , which is the object plane of the magnetic objective lens defocused by  $\Delta f$  (Rempfer & Griffith 1992; Nepijko & Sedov 1997; Kennedy *et al.*, 2010). The magnification on this plane is

$$\bar{M}(\Delta f) = \frac{2}{3} \left( 1 - \frac{3\Delta f}{4L_M} \right), \quad (2.2)$$

compared to the specimen surface, which reduces to  $2/3$  for small defocus.

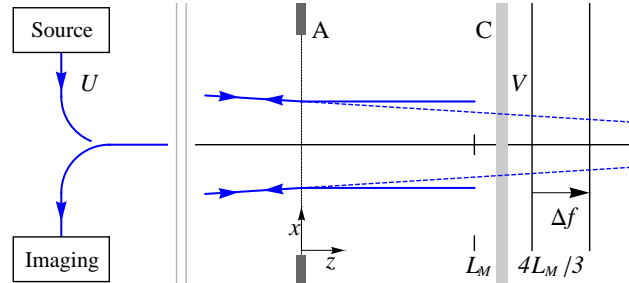


Figure 2. Classical electron trajectories (solid lines), in which the converging incident electron beam in the electric field free region ( $z < 0$ ) is focused on the optical axis  $z$  at  $z = 4L_M$ . The trajectories are deflected away from the  $z$  axis due to the distortion of the electric field in the vicinity of the anode aperture A. This effect is approximated by treating the aperture A as a diverging lens (Grant & Phillips 1990; Lenc & Müllerová 1992; Rempfer & Griffith 1992; Nepijko & Sedov 1997; Kennedy *et al.*, 2010). The deflection of the converging beam away from the  $z$  axis results in parallel illumination of the cathode specimen C, which is held at the potential  $V < 0$  compared to the anode, so that an electron of energy  $U < -eV$  turns at a distance of  $z = L_M$ . The returning electron trajectories are deflected away from the  $z$  axis when passing back out the anode aperture, retracing the incident trajectory for a perfectly flat equipotential specimen. As in figure 1, we trace back along the apparent straight line paths (dashed lines) to the virtual image plane in the vicinity of  $z = 4L_M/3$ . The  $y$  axis extends out of the page. Based on Kennedy *et al.* (2011)

In a modern LEEM instrument, it is customary to illuminate the specimen with an electron beam that is parallel to the optical axis  $z$  (Altman 2010; Tromp *et al.*, 2010). When treating the anode aperture A as a diverging lens with focal length  $-4L_M$  (Grant & Phillips 1990; Lenc & Müllerová 1992; Rempfer & Griffith 1992; Nepijko & Sedov 1997; Kennedy *et al.*, 2010), we achieve parallel illumination by using a converging electron beam that is focused on the  $z$  axis to the point  $z = 4L_M$ . After passing through the anode aperture the

beam emerges parallel to the optical axis  $z$ . As shown in figure 2, for a perfectly flat, equipotential specimen an electron that enters the anode aperture at  $(x_0, y_0)$  remains at  $(x_0, y_0)$  in the vicinity of the turning region  $z = L_M$ , and exits the anode aperture at approximately the same transverse position. As before we trace back along the apparent straight line path of the exiting electron to the virtual image plane  $z = \Delta f + 4L_M/3$ , where the virtual image plane is magnified by

$$M(\Delta f) = \frac{2}{3} \left( 1 - \frac{3\Delta f}{8L_M} \right), \quad (2.3)$$

compared to the specimen surface.

Given the wide applicability of systems using the modern LEEM parallel illumination of the specimen (figure 2), it is important to consider the modifications to Laplacian imaging theory, since the latter was originally developed in a divergent-illumination geometry.

### 3. Geometrical theory of MEM contrast

Following the approach of Kennedy *et al.* (2010), we consider the interaction of an electron with variations in electrical potential  $V(x, y, \bar{z})$  above the specimen surface, where  $\bar{z} = L - z$ . This additional potential can be caused by areas of differing work function or applied voltage, and/or when a surface varies in height. Here we concentrate on surface height variations, but the methodology is equally applicable to surface potential variations, or both height and potential variations. We approximate a surface with height variations, characterised by  $H(x, y)$ , with the equivalent planar surface with a corresponding potential distribution (Nepijko & Sedov 1997)

$$V(x, y, \bar{z} = 0) = VH(x, y)/L. \quad (3.1)$$

Solving the Dirichlet problem for Laplace's equation for a half space we have (Polozhiy 1967; Boudjelkha & Diaz 1972; Nepijko & Sedov 1997; Kennedy *et al.* 2010)

$$V(x, y, \bar{z}) = \frac{\bar{z}}{2\pi} \int \int_{-\infty}^{\infty} \frac{V(\xi, \eta, \bar{z} = 0)}{((x - \xi)^2 + (y - \eta)^2 + \bar{z}^2)^{3/2}} d\xi d\eta, \quad (3.2)$$

which expressed as a convolution is (Cowley 1995; Press *et al.* 2007)

$$V(x, y, \bar{z}) = \frac{\bar{z}}{2\pi} V(x, y, \bar{z} = 0) \otimes (x^2 + y^2 + \bar{z}^2)^{-3/2}. \quad (3.3)$$

From equation (3.1), the variation in electric potential above the specimen surface can then be expressed as the height function  $H(x, y)$  convolved with a smoothing function,

$$V(x, y, \bar{z}) = \frac{\bar{z}V}{2\pi L} H(x, y) \otimes (x^2 + y^2 + \bar{z}^2)^{-3/2}. \quad (3.4)$$

As discussed in Kennedy *et al.* (2010), the smoothing function represents the blurring and softening of the electric field when moving away from the cathode surface. For example, the smoothed potential extends beyond the  $(x, y)$  range of a localised hill or valley described by  $H(x, y)$ . The geometrical theory of MEM contrast assumes that any change to the electron motion caused by the finite height variation of the specimen occurs very close to the sample surface, since the additional potential  $V(x, y, \bar{z})$  rapidly approaches zero as  $\bar{z}$  increases away from the surface. Additionally, it is assumed that the  $z$ -dimension motion is unchanged, so that all of the momentum change in the transverse dimensions  $(x, y)$  occurs very close to the classical turning point at  $z = L_M$ .

In the modern LEEM geometry, an electron that enters the anode at  $(x_0, y_0)$  is affected most strongly by the cathode at  $(x_0, y_0)$  where it is closest to the surface (see figure 2), rather than  $(3x_0/2, 3y_0/2)$  for the divergent illumination geometry. We therefore estimate the  $x$  and  $y$  derivatives of the potential by integrating along the  $z$  axis for the column  $(x_0, y_0)$ , obtaining the change to the  $x$  and  $y$  velocities respectively. The shift of electron position  $S_x, S_y$  on the plane  $z = 4L_M/3 + \Delta f$  due to  $H(x, y)$ , which is scaled by  $1/M$  (equation (2.3)) (Dyukov *et al.*, 1991; Nepijko & Sedov, 1997), is given by

$$S_x(x, y, \delta, \Delta f) = (\partial/\partial x) \frac{\sqrt{L_M}}{\pi} \frac{9\Delta f}{8L_M - 3\Delta f} H(x, y) \otimes ((\delta^2 + x^2 + y^2)^{-3/4} (2E_E(x, y, \delta) - E_K(x, y, \delta))), \quad (3.5)$$

and

$$S_y(x, y, \delta, \Delta f) = (\partial/\partial y) \frac{\sqrt{L_M}}{\pi} \frac{9\Delta f}{8L_M - 3\Delta f} H(x, y) \otimes ((\delta^2 + x^2 + y^2)^{-3/4} (2E_E(x, y, \delta) - E_K(x, y, \delta))), \quad (3.6)$$

where

$$E_E(x, y, \delta) = E \left( \frac{1}{2} - \frac{\delta}{2(\delta^2 + x^2 + y^2)^{1/2}} \right), \quad E_K(x, y, \delta) = K \left( \frac{1}{2} - \frac{\delta}{2(\delta^2 + x^2 + y^2)^{1/2}} \right), \quad (3.7)$$

and  $K$ ,  $E$  respectively denote complete elliptic integrals of the first and second kind (Abramowitz & Stegun 1964; Borwein & Borwein 1987). For  $\Delta f = 0$  the electron shifts are zero, even for a rough surface with non-zero  $H(x, y)$ . Therefore the plane  $z = 4L_M/3$  corresponds to the in-focus plane of minimum contrast, and a finite defocus  $\Delta f$  is required to obtain image contrast (Kennedy *et al.*, 2010).

We note that equations (3.5) and (3.6) differ from equations (1.5) and (1.6) of Kennedy *et al.* (2010) only in that the term  $9\Delta f/(8L_M - 6\Delta f)$  has been replaced by  $9\Delta f/(8L_M - 3\Delta f)$  here. This is equivalent to multiplying the position shift functions in the divergent illumination geometry by the change in magnification  $\bar{M}/M$  (equations (2.2) and (2.3) respectively), in changing from divergent to parallel illumination. That is, multiplying the prefactor in (1.5) and (1.6) of Kennedy *et al.* (2010), which is  $(\sqrt{L_M}/\pi)(9\Delta f/(8L_M - 6\Delta f))$ , by the change in magnification

$$\frac{\bar{M}}{M} = \frac{\frac{2}{3} \left(1 - \frac{3\Delta f}{4L_M}\right)}{\frac{2}{3} \left(1 - \frac{3\Delta f}{8L_M}\right)} = \frac{8L_M - 6\Delta f}{8L_M - 3\Delta f}, \quad (3.8)$$

gives a prefactor of  $(\sqrt{L_M}/\pi)(9\Delta f/(8L_M - 3\Delta f))$ , as per equations (3.5) and (3.6) here. Thus for small objective lens defocus  $\Delta f \ll 4L_M/3$ , these shifts are negligibly affected by the change in MEM geometry.

We may express the electron position shifts in terms of the blurred height  $H_B$ . For example,  $S_x$  becomes

$$S_x(x, y, \delta, \Delta f) = (\partial/\partial x) H_B(x, y, \delta, \Delta f), \quad (3.9)$$

and similarly for  $S_y$ , with

$$H_B(x, y, \delta, \Delta f) = \frac{\Delta f}{8L_M - 3\Delta f} H(x, y) \otimes B(x, y, \delta), \quad (3.10)$$

and blurring function

$$B(x, y, \delta) = \frac{9\sqrt{L_M}}{\pi} (\delta^2 + x^2 + y^2)^{-3/4} (2E_E(x, y, \delta) - E_K(x, y, \delta)). \quad (3.11)$$

The shift in electron positions redistributes the intensity on the plane  $z = 4L_M/3 + \Delta f$ , which can be derived from electron flux conservation giving (Dyukov *et al.* 1991; Nepijko *et al.* 2001b; Kennedy *et al.*, 2010)

$$I \left( x + \frac{\partial H_B}{\partial x}, y + \frac{\partial H_B}{\partial y}, \delta, \Delta f \right) = 1 / \left| 1 + \frac{\partial^2 H_B}{\partial x^2} + \frac{\partial^2 H_B}{\partial y^2} + \left( \frac{\partial^2 H_B}{\partial x^2} \right) \left( \frac{\partial^2 H_B}{\partial y^2} \right) - \left( \frac{\partial^2 H_B}{\partial x \partial y} \right)^2 \right|, \quad (3.12)$$

in terms of the blurred height  $H_B$ .

#### 4. Laplacian Image contrast in MEM with parallel illumination

We now consider the geometrical theory of MEM contrast in the limit of small objective lens defocus and/or slowly varying  $H(x, y)$ . This limit requires that the derivatives of the blurred height are small,

$$|\partial^2 H_B(x, y, \delta, \Delta f)/\partial x^2| \ll 1, \quad |\partial^2 H_B(x, y, \delta, \Delta f)/\partial y^2| \ll 1, \quad (4.1)$$

which for simplicity we will refer to as

$$|\nabla_{\perp}^2 H_B(x, y, \delta, \Delta f)| \ll 1, \quad (4.2)$$

where  $\nabla_{\perp}^2$  is the transverse Laplacian ( $\partial^2/\partial x^2 + \partial^2/\partial y^2$ ). The conditions (4.1) and (4.2) are met for a sufficiently slowly varying  $H$  and for defocus that satisfies

$$|\Delta f| \ll 8L_M / (3 + \max_{x,y} |\nabla_{\perp}^2 H(x,y) \otimes B(x,y,\delta)|), \quad (4.3)$$

where  $\max_{x,y} g(x,y)$  denotes the maximum value of  $g(x,y)$  over the range of points  $(x,y)$ . Note that smoothness of the height profile is not required, only that the Laplacian of the height profile (blurred by the function  $B$ ) and/or the defocus is small enough to satisfy equations (4.1) and (4.3). In comparison with the equivalent validity condition for diverging illumination, equation (3.3) of Kennedy *et al.* (2010), noting that the modified form of  $B(x,y,\delta)$  for parallel illumination (equation (3.11)) is twice that of  $B$  for diverging illumination (equation (2.10) of Kennedy *et al.* (2010)), under parallel illumination we have a factor of 3 in the denominator of equation (4.3) rather than 6. This suggests that for parallel illumination, Laplacian imaging theory is valid for a broader range of defocus values.

In the limit of small defocus  $\Delta f$  and/or slowly varying  $H(x,y)$  ensuring small derivatives of the blurred height, the intensity (equation (3.12)) is approximated by (Kennedy *et al.*, 2010)

$$I(x,y,\delta,\Delta f) \approx 1 - \nabla_{\perp}^2 H_B(x,y,\delta,\Delta f). \quad (4.4)$$

This is valid for small shifts in electron trajectory, so we have neglected both the change in  $x, y$  coordinates in  $I(x,y,\delta,\Delta f)$  and derivatives greater than second order. Since we have assumed the derivatives are small (equation (4.1)), we have also taken the binomial approximation in the denominator. The blurred height contains the constant term  $\Delta f / (8L_M - 3\Delta f)$  (see equation (3.10)), so for defocus values satisfying  $\Delta f \ll 8L_M/3$  we have an intensity of

$$I(x,y,\delta,\Delta f) \approx 1 - \Delta f \nabla_{\perp}^2 H(x,y) \otimes \frac{B(x,y,\delta)}{8L_M}. \quad (4.5)$$

We note that because  $B(x,y,\delta)$  for parallel illumination (equation (3.11)) is twice that for diverging illumination, the intensity (equation (4.5)) is identical to the intensity expression for divergent illumination, equation (3.7) of Kennedy *et al.* (2010). Consequently, the simulations and interpretation of droplet trail contrast in §4 and §5 of Kennedy *et al.* (2010) equally apply to both geometries.

Whilst we consider parallel illumination here, the Laplacian imaging theory can be applied to similar imaging geometries. The general effect will be to multiply the electron shifts with the term  $\bar{M}/M$ , where  $\bar{M}$  is the virtual image plane magnification in an existing geometry, and  $M$  is the magnification in the new geometry. Lastly, where these approximations are not valid, due, for example, to either large defocus and/or strong surface height variations, alternative methods such as numerical ray tracing or the recently developed caustic imaging theory may be employed (Kennedy *et al.* 2011). For fully quantitative simulations, alternative methods may also require a more rigorous treatment of the electric field variations throughout the path of the electron beam, for example, the distortion of the equipotential surfaces in the vicinity of the anode aperture, which was approximated by a thin diverging lens here.

## 5. Extensions and the inverse problem

Kennedy *et al.* (2010) discuss a number of extensions, such as the inclusion of chromatic aberration. These extensions are equally applicable to the modern geometry considered here, with the same equations used provided the appropriate expressions for the blurred height and blurring function are used (equations (3.10) and (3.11) respectively). In particular, to include chromatic aberration, we replace the monochromatic blurring function  $(\Delta f / (8L_M - 3\Delta f))B(x,y,\delta)$  with the chromatically averaged  $B_C(x,y,\delta_0,\Delta f)$ , given by (Kennedy *et al.* 2010)

$$B_C(x,y,\delta_0,\Delta f) = \int \frac{\sqrt{L-\delta}}{\pi} \frac{9(\Delta f + 2(\delta - \delta_0))}{8(L-\delta) - 3(\Delta f + 2(\delta - \delta_0))} (\delta^2 + x^2 + y^2)^{-3/4} \times (2E_E(x,y,\delta) - E_K(x,y,\delta)) D(\delta) d\delta. \quad (5.1)$$

Here, a defocus of  $\Delta f + 2(\delta - \delta_0)$  ensures that each image corresponds to the plane  $z = 4(L - \delta_0)/3 + \Delta f$ , and where  $\delta_0$  is the mean of the distribution. Chromatic aberration, then, can be incorporated into the Laplacian

imaging theory by averaging over several blurring functions to obtain the effective blur  $B_C$ . With a normalized distribution we then have (Kennedy *et al.* 2010)

$$I_C(x, y, \delta_0, \Delta f) \approx 1 - \nabla_{\perp}^2 H(x, y) \otimes B_C(x, y, \delta_0, \Delta f). \quad (5.2)$$

Kennedy *et al.* (2010) also considers the inverse problem whereby image contrast is analysed to estimate the perturbed electric potential and/or the height variation of the specimen. In the Laplacian imaging theory of MEM contrast this may be achieved using the Fourier derivative theorem (Cowley 1995; Paganin 2006) to convert between spatial derivatives and Fourier space coordinates,

$$\mathcal{F}(I(x, y, \delta, \Delta f) - 1) \approx \mathcal{F}(-\nabla_{\perp}^2 H_B(x, y, \delta, \Delta f)) = (k_x^2 + k_y^2) \mathcal{F} H_B(x, y, \delta, \Delta f), \quad (5.3)$$

where  $k_x$  and  $k_y$  are the Fourier space coordinates corresponding to real space coordinates  $x$  and  $y$  respectively,  $\mathcal{F}$  is the Fourier transform with respect to  $x$  and  $y$ , and  $\mathcal{F}^{-1}$  is the corresponding inverse Fourier transform. This gives (Gureyev & Nugent 1997; Kennedy *et al.* 2010)

$$H_B(x, y, \delta, \Delta f) \approx \mathcal{F}^{-1}((k_x^2 + k_y^2)^{-1} \mathcal{F}(I(x, y, \delta, \Delta f) - 1)), \quad (5.4)$$

namely the recovery of the blurred height function from a single image, facilitating the analysis of MEM movie dynamics (Tersoff *et al.* 2009). This expression bears a strong resemblance to phase retrieval via the transport of intensity equation (Teague 1983; Gureyev & Nugent 1997), whereby the original phase object may be recovered via a single phase contrast image.

After obtaining the blurred height function, which depends on the parameters of the MEM, we then deconvolve to obtain the height function, for example via equation (3.10) and using the convolution theorem (Cowley 1995)

$$H(x, y, \delta) = \frac{(8L_M - 3\Delta f)}{2\pi\Delta f} \mathcal{F}^{-1} \left( \frac{\mathcal{F}(H_B(x, y, \delta, \Delta f))}{\mathcal{F}(B(x, y, \delta))} \right). \quad (5.5)$$

If the value of the defocus is not known, we can only recover the height to within the scaling factor  $(8L_M - 3\Delta f)/\Delta f$ . The scaling factor is the sole difference between equation (5.5) and the equivalent equation (7.3) for divergent illumination in Kennedy *et al.* (2010). But since the preliminary examples of a droplet trail in figure 9 of Kennedy *et al.* (2010) were recovered to within the scaling factor, the examples are unchanged assuming parallel illumination.

## 6. Conclusions

We have applied the recently developed Laplacian imaging theory of MEM to an imaging geometry where a converging electron beam is used to ensure parallel illumination of the specimen. Within the domain of validity of the aperture lens approximation and for small defocus, the expressions for the MEM image contrast are unchanged when compared with divergent illumination, and the results and extensions considered by Kennedy *et al.* (2010) apply. We have shown that the Laplacian imaging theory for parallel illumination has a broader range of valid defocus values. For larger defocus, a scaling factor is geometry dependent, but the Laplacian imaging theory remains a valid and intuitive method of interpreting MEM image contrast.

We are grateful to Michael Altman and Ruud Tromp for stimulating this work. S.M.K. acknowledges funding from the J. L. William Bequest and a Postgraduate Publication Award. D.M.P., W.X.T. and D.E.J. acknowledge funding from the Australian Research Council.

## References

- Abramowitz, M. & Stegun, I. A. 1964 *Handbook of mathematical functions with formulas, graphs, and mathematical tables*, second printing, Ch. 17, pp. 589–592, Washington: United States Department of Commerce and National Bureau of Standards (also available online).
- Altman, M. S. 2010 Trends in low energy electron microscopy. *J. Phys.: Condens. Matter* **22**, 084017 (DOI 10.1088/0953-8984/22/8/084017).
- Barnett, M. E. & Nixon, W. C. 1967a A mirror electron microscope using magnetic lenses *J. Sci. Instrum.* **44**, 893–897. (DOI 10.1088/0950-7671/44/11/302).
- Barnett, M. E. & Nixon, W. C. 1967b Electrical contrast in mirror electron microscopy *Optik* **26**, 310–325.

- Bauer, E. 1985 The resolution of the low energy electron reflection microscope *Ultramicroscopy* **17** 51–56. (DOI 10.1016/0304-3991(85)90176-7).
- Bauer, E. 1994 Low energy electron microscopy *Rep. Prog. Phys.* **57** 895–938. (DOI 10.1088/0034-4885/57/9/002).
- Bauer, E. 1998 LEEM basics *Surf. Rev. Lett.* **5** 1275–1286. (DOI 10.1142/S0218625X98001614).
- Bok, A. B. 1978 Mirror electron microscopy theory and applications. In *Diffraction and imaging techniques in material science* (eds S. Amelinckx, R. Gevers & J. Van Landuyt), 2nd rev. edn., pp. 761–788, Amsterdam: North-Holland.
- Borwein, J. M. & Borwein, P. B. 1987 *Pi and the AGM, a study in analytic number theory and computational complexity*, vol. 4, pp. 7–9, New York: John Wiley & Sons.
- Boudjelkha, M. T. & Diaz, J. B. 1972 Half space and quarter space Dirichlet problems for the partial differential equation *Applicable Analysis* **1** 297–324. (DOI 10.1080/00036817208839020).
- Cowley, J. M. 1995 *Diffraction physics*, 3rd rev. edn., pp. 26–35, 59–63, Amsterdam: North-Holland.
- Dupuy, J. C., Sibai, A. & Vilotitch, B. 1984 Mirror electron microscopy (MEM): Work function and imaging of an electron beam biased junction of silicon (100) *Surf. Sci.* **147** 191–202. (DOI 10.1016/0039-6028(84)90175-4).
- Dyukov, V. G., Nepijko, S. A. & Sedov, N. N. 1991 *Electron microscopy of local potentials*, pp. 10–12, 28–35, 45–51, 63–66, 73–76, Kiev: Naukova Dumka (in Russian).
- Godehardt, R. 1995 Mirror electron microscopy *Adv. Imag. Elect. Phys.* **94** 81–150. (DOI 10.1016/S1076-5670(08)70144-7).
- Grant, I. S. & Phillips, W. R. 1990 *Electromagnetism*, 2nd edn., pp. 100–103, Chichester: John Wiley & Sons.
- Gureyev, T. E. & Nugent, K. A. 1997 Rapid quantitative phase imaging using the transport of intensity equation *Opt. Commun.* **133** 339–346. (DOI 10.1016/S0030-4018(96)00454-3).
- Kennedy, S. M., Zheng, C. X., Tang, W. X., Paganin, D. M. & Jesson, D. E. 2010 Laplacian image contrast in mirror electron microscopy. *Proc. R. Soc. A.* **466**, 2857–2874 (DOI 10.1098/rspa.2010.0093).
- Kennedy, S. M., Zheng, C. X., Tang, W. X., Paganin, D. M. & Jesson, D. E. 2011 Caustic imaging of gallium droplets using mirror electron microscopy. *Ultramicroscopy* **111**, 356–363 (DOI 10.1016/j.ultramic.2011.01.019).
- Lenc, M. & Müllerová, I. 1992 Electron optical properties of a cathode lens. *Ultramicroscopy* **41**, 411–417 (DOI 10.1016/0304-3991(92)90220-E).
- Luk'yanov, A. E., Spivak, G. V. & Gvozdover, R. S. 1974 Mirror electron microscopy *Sov. Phys. Usp.* **16** 529–552. (DOI 10.1070/PU1974v016n04ABEH005299).
- Nepijko, S. A. & Schönhense, G. 2010 Measurement of potential distribution function on object surface by using an electron microscope in the mirror operation mode *J. Microsc.* **238** 90–94. (DOI 10.1111/j.1365-2818.2009.03340.x).
- Nepijko, S. A. & Sedov, N. N. 1997 Aspects of mirror electron microscopy *Adv. Imag. Elect. Phys.* **102** 273–323. (DOI 10.1016/S1076-5670(08)70125-3).
- Nepijko, S. A., Sedov, N. N., Schmidt, O., Schönhense, G., Bao, X. & Huang, W. 2001a Imaging of three-dimensional objects in emission electron microscopy *J. Microsc.* **202** 480–487. (DOI 10.1046/j.1365-2818.2001.00846.x).
- Nepijko, S. A., Sedov, N. N. & Schönhense, G. 2001b Peculiarities of imaging one- and two-dimensional structures using an electron microscope in the mirror operation mode *J. Microsc.* **203** 269–276. (DOI 10.1046/j.1365-2818.2001.00895.x).
- Nepijko, S. A., Gloskovskii, A., Sedov, N. N. & Schönhense, G. 2003 Measurement of the electric field distribution and potentials on the object surface in an emission electron microscope without restriction of the electron beams *J. Microsc.* **211** 89–94. (DOI 10.1046/j.1365-2818.2003.01199.x).
- Nepijko, S. A., Marx, G. K. L. & Schönhense, G. 2007 Quantitative determination of magnetic fields on object surfaces via photoemission electron microscopy without restriction of the electron beam *Nucl. Instr. and Meth. in Phys. Res. B* **264** 194–200. (DOI 10.1016/j.nimb.2007.08.076).
- Paganin, D. M. 2006 *Coherent X-ray optics*, pp. 278–284, 295–301, 395–396, New York: Oxford University Press.
- Polozhiy, G. N. 1967 *Equations of mathematical physics*, pp. 62–64, 149, New York: Hayden Book Company.
- Press, W. H., Teukolsky, S. A., Vetterling, W. T. & Flannery, B. P. 2007 *Numerical recipes, the art of scientific computing*, 3rd edn., pp. 600–604, Cambridge: Cambridge University Press.
- Rempfer, G. F. & Griffith, O. H. 1992 Emission microscopy and related techniques: resolution in photoelectron microscopy, low energy electron microscopy and mirror electron microscopy *Ultramicroscopy* **47** 35–54. (DOI 10.1016/0304-3991(92)90184-L).
- Someya, T. & Kobayashi, J. 1974 Quantitative application of electron-mirror microscopy to the determination of pure shear of ferroelectric  $\text{Gd}_2(\text{MoO}_4)_3$  *Phys. Stat. Solidi (a)* **26** 325–336. (DOI 10.1002/pssa.2210260134).
- Teague, M. R. 1983 Deterministic phase retrieval: a Green's function solution *J. Opt. Soc. Am.* **73** 1434–1441. (DOI 10.1364/JOSA.73.001434).
- Tersoff, J., Jesson, D. E. & Tang W. X. 2009 Running droplets of Ga from evaporation of GaAs *Science* **324** 236–238. (DOI 10.1126/science.1169546).
- Tromp, R. M., Hannon, J. B., Ellis, A. W., Wan, W., Berghaus, A. & Schaff, O. 2010 A new aberration-corrected, energy-filtered LEEM/PEEM instrument. I. Principles and design. *Ultramicroscopy* **110**, 852–861 (DOI 10.1016/j.ultramic.2010.03.005).



---

## Caustic imaging of gallium droplets using mirror electron microscopy

This chapter is an author generated post print of the article

S. M. Kennedy, C. X. Zheng, W. X. Tang, D. M. Paganin and D. E. Jesson, *Caustic imaging of gallium droplets using mirror electron microscopy*, *Ultramicroscopy*, 111 (2011) 356-363, available electronically at <http://www.sciencedirect.com/science/article/pii/S0304399111000349>.

## Declaration for Thesis Chapter “Caustic imaging of gallium droplets using mirror electron microscopy”

Declaration by candidate

For this chapter, the nature and extent of my contribution to the work was the following:

Nature of contribution	Extent of contribution(%)
Designed and performed the AFM and MEM experiments and co-wrote the paper.	25

The following co-authors contributed to the work. Co-authors who are students at Monash University must also indicate the extent of their contribution in percentage terms

Name	Extent of contribution(%)	Nature of contribution
Shane Kennedy	70	Developed the model used in the paper, performed the image simulations, co-wrote the paper.
Wen-XinTang		provided technical expertise.
David Paganin		Co-wrote the paper, co-developed the model and provided technical expertise.
David Jesson		Co-wrote the paper, co-developed the model and provided technical expertise.

Candidate's signature		Date	24-08-12
-----------------------	--	------	----------

**Declaration by co-authors**

The undersigned hereby certify that:

- (1) they meet the criteria for authorship in that they have participated in the conception, execution, or interpretation, of at least that part of the publication in their field of expertise;
- (2) they take public responsibility for their part of the publication, except for the responsible author who accepts overall responsibility for the publication;
- (3) there are no other authors of the publication according to these criteria;
- (4) potential conflicts of interest have been disclosed to (a) granting bodies, (b) the editor or publisher of journals or other publications, and (c) the head of the responsible academic unit; and
- (5) the original data are stored at the following location(s) and will be held for at least five years from the date indicated below:

Location(s)	School of Physics, Monash University, Clayton
-------------	---

Signature 1		Date	23-08-12
Signature 2			21-08-12
Signature 3			24-08-2012
Signature 4			21-08-12

# Caustic imaging of gallium droplets using mirror electron microscopy

S. M. Kennedy, C. X. Zheng, W. X. Tang, D. M. Paganin and D. E. Jesson<sup>1</sup>

*School of Physics, Monash University, Victoria, 3800, Australia*

---

## Abstract

We discuss a new interpretation of mirror electron microscopy (MEM) images, whereby electric field distortions caused by surface topography and/or potential variations are sufficiently large to create caustics in the image contrast. Using a ray-based trajectory method, we consider how a family of rays overlaps to create caustics in the vicinity of the imaging plane of the magnetic objective lens. Such image caustics contain useful information on the surface topography and/or potential, and can be directly related to surface features. Specifically we show how a through-focus series of MEM images can be used to extract the contact angle of a Ga droplet on a GaAs (001) surface.

*Keywords:* Mirror electron microscopy (MEM), caustic imaging, Ga droplets, GaAs, contact angle

---

## 1. Introduction

Mirror electron microscopy (MEM) is a well-established technique for imaging surface phenomena in real time, with applications in studying electric field contrast [1–6], droplet surface dynamics [7–9], surface magnetic fields [10], and chemical processes at solid surfaces [11]. The importance of understanding *in situ* dynamical behaviour and surface evolution under technologically important conditions makes the interpretation of MEM images an important avenue of investigation. In MEM, electrons neither touch nor are emitted from the sample. Instead a normally incident electron beam is reflected just above the specimen surface, as a result of the specimen

---

<sup>1</sup> [REDACTED]

voltage being tuned to be slightly more negative than that of the electron source. In the turn-around region, the slow moving electrons are sensitive to spatial and/or temporal variations in the electric field and are deflected, creating image contrast in the reflected beam. Such variations in the electric field may, for example, be caused by the surface topography [12–15] and/or variations in the electric potential of the specimen, which includes contact potentials, surface charges and varying conductivity [1–3, 6, 10, 11, 16].

The returning electron beam therefore contains information on the electric field variations caused by surface topography and/or electrical and magnetic phenomena. This has stimulated numerous efforts to interpret MEM image contrast and extract quantitative information regarding electric field variations and surface properties. A variety of approaches have been employed, some based on wave mechanics [17, 18], but most have been based on geometrical ray tracing techniques [1, 2, 11, 14, 16, 19–24]. For small surface variations and/or small defocus, it has recently been shown that MEM image contrast can be intuitively and rapidly interpreted as the Laplacian or curvature of a blurred surface height function [25].

Large variations in surface height or potential are, however, capable of deflecting the electron trajectories so much that very strong image contrast is created including caustic features [1, 19, 26, 27]. Such deflections typically violate the assumptions underlying many of the previous approaches, which assume that the  $z$  motion of the electron beam (i.e. along the optical axis) is largely unchanged by the surface height or potential variations [6, 14, 19, 20, 24, 25]. Approaches allowing for strongly deflected electron trajectories have, to date, only been solvable for specific analytical cases [14, 20]. Here we present a general ray-based method of interpreting MEM image contrast using a family or envelope of incident electron rays traced through the electric field close to the specimen surface. This approach is similar to the methods employed by Kan and Phaneuf [13]. Where strong deflections occur, ray trajectories crossing a caustic surface are observed, which can be directly related to variations in the field above the surface. This specifically allows for the simulation and interpretation of MEM image contrast in the presence of stronger field variations than has previously been possible.

## 2. MEM imaging geometry

A typical electrostatic MEM immersion lens is shown schematically in Fig. 1. Electrons of initial energy  $U$  travel along the optical axis  $z$  of the im-

immersion lens, pass through the anode aperture A, and are reflected in the vicinity of  $z = L_M$ , a distance of  $\delta$  above the specimen surface C. The specimen, located a distance of  $L$  from the anode, acts as the cathode of the immersion objective lens [1, 2, 16, 25, 28, 29], and is held at a negative potential  $V < -U/e < 0$  relative to the grounded anode, where  $-e$  is the electronic charge.

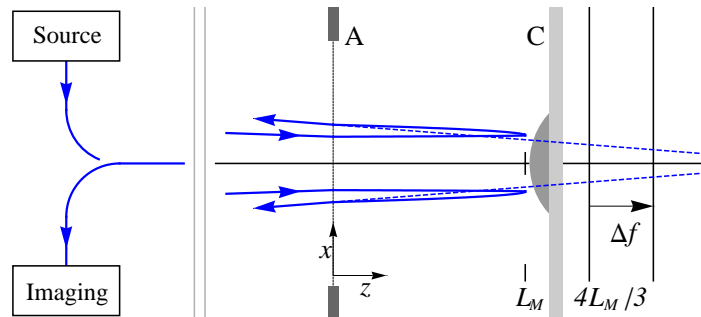


Figure 1: MEM imaging geometry. An electron beam of energy  $U$  is focused by the magnetic objective lens to a cross-over point ( $x = 0, z = 4L_M$ ). The anode aperture A acts as a diverging lens, deflecting the electron trajectories away from the  $z$  axis as they enter and leave. The cathode C is set at the potential  $V < -U/e < 0$  so that the electron beam turns around in the vicinity of  $z = L_M$ , where it is sensitive to deviations in the electric field due to surface and/or potential variations of the cathode. We trace the exiting electron trajectories back along the apparent straight line paths to the virtual image plane at  $z = \Delta f + 4L_M/3$ . This is the object plane for the magnetic objective lens. The  $y$  axis extends out of the page.

The magnetic imaging part of the objective lens can, to a good approximation, be considered separately to the electrostatic MEM immersion lens of Fig. 1 [28, 29]. Following reflection, the returning electron beam is further deflected by the anode aperture which acts as a diverging lens [20, 22, 25, 30]. On retracing back along the apparent straight line paths of the exiting electron trajectories it can be seen that a virtual image is formed on a plane at  $z = \Delta f + 4L_M/3$ . This is the object plane of the magnetic objective lens defocused by  $\Delta f$ , which is defined as positive in the positive  $z$  direction, and where  $L_M$  is given by

$$L_M = -LU/eV = L - \delta. \quad (1)$$

As shown in Fig. 2, the incident electron beam is focused on the point  $z = 4L_M$  by the magnetic objective lens. However, the anode aperture

acts as a diverging lens providing parallel illumination of the sample. For the perfectly flat and equipotential specimen of Fig. 2, the electron beam remains parallel to the  $z$  axis at the transverse distance of  $x = x_0$ . After turning in the vicinity of  $z = L_M$ , the returning electron beam is deflected away from the  $z$  axis as it passes back through the anode aperture, and travels along the same trajectory as the incident beam. We trace the apparent straight line path of the emerging electron beam back to the virtual image plane in the vicinity of  $z = 4L_M/3$ . At this plane, an electron that interacted with the potential above the cathode surface at  $x = x_0$  appears on the virtual image plane at  $2x_0/3$ , so the virtual image must have transverse distances scaled by  $3/2$  to return to the scale of the specimen.

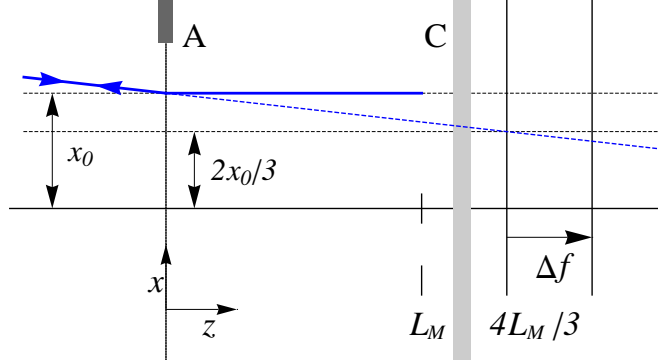


Figure 2: Formation of the virtual image plane at  $z = 4L_M/3$  for an unperturbed cathode specimen. An electron trajectory directed towards the point  $(x = 0, z = 4L_M)$  is deflected when passing through the anode aperture, emerging parallel to the  $z$  axis. After turning in the vicinity of the point  $(x = x_0, z = L_M)$ , the returning electron is again deflected away from the  $z$  axis. The apparent straight line path of the exiting electron is traced back to the virtual image plane in the vicinity of  $z = 4L_M/3$ , with transverse distance  $2x_0/3$ . The  $y$  axis extends out of the page.

### 3. Evaluation of the electric potential above the specimen surface

To calculate the distribution of electron positions on the image plane  $z = \Delta f + 4L_M/3$ , we must first solve Laplace's equation for the electric potential  $\phi(r, \theta, z)$  in the region  $0 \leq z \leq L$ . In cylindrical coordinates  $r, \theta, z$ , this is given by [31]

$$\nabla^2 \phi = \frac{1}{r} \frac{\partial}{\partial r} \left( r \frac{\partial \phi}{\partial r} \right) + \frac{1}{r^2} \frac{\partial^2 \phi}{\partial \theta^2} + \frac{\partial^2 \phi}{\partial z^2} = 0. \quad (2)$$

For an equipotential flat specimen surface, there is no  $r$  or  $\theta$  dependence and the solution of Eq. (2) is approximately

$$\phi_U(z) = Vz/L, \quad 0 \leq z \leq L, \quad (3)$$

where the penetration of the electric field through the anode aperture is approximated by treating the aperture as a thin diverging lens [20, 22, 25, 30]. For spatial variations in surface topography and/or potential the solution of Eq. (2) is necessarily more complex. In limited cases, analytical solutions can be found [20]. Additionally, for surface potential variations, and for sufficiently small variations in topography, the system can be reduced to the equivalent Dirichlet problem for Laplace's equation for a half space, facilitating the calculation of  $\phi(r, \theta, z)$  [20, 25, 32–35]. However, this latter approach breaks down when surface topographical variations are large enough to appreciably move the electron turn-around region (i.e. by many times the unperturbed turning distance  $\delta$  from the specimen).

In general it is necessary to solve Eq. (2) numerically. Many authors use charge-ring techniques [36–38], but here we employ standard finite element methods, using the specimen topography as one boundary (either equipotential or with a variable surface potential) and the grounded anode as the opposite boundary. Our simulations utilise the finite element methods package FreeFem++ v3.9-0 [39], with mesh adaptation. We consider the specific case of a cylindrically symmetrical electric potential,  $\phi(r, z)$ , so we need only consider the electric field in two dimensions. However, the method is readily extendable to three dimensions with a corresponding increase in complexity and computation time.

#### 4. Caustic image simulations

With knowledge of the electric potential in the region  $0 \leq z \leq L$ , we can evaluate the electron trajectories through this region and project them back onto the virtual image plane at  $z = \Delta f + 4L_M/3$ . To this end, let  $(r^{(j)(t)}, z^{(j)(t)})$  and  $(v_r^{(j)(t)}, v_z^{(j)(t)})$  denote the respective position and velocity of the  $j$ th electron at time  $t$ . For the maximum velocities  $v_{max} \approx 0.28c$  m/s considered here, where  $c$  is the speed of light in vacuum, the Lorentz factor  $(1 - v_{max}^2/c^2)^{-1/2} \approx 1.04$  so we ignore relativistic corrections. At  $t = 0$  we input a family of electron ray trajectories at  $z = 0$ , which are equally spaced in the transverse dimension  $r$  by the distance  $r_0$ . The  $j$ th ray at

$t = 0$  begins at the point

$$(r^{(j)(0)}, z^{(j)(0)}) = (jr_0, 0), \quad (4)$$

with velocities  $(v_r^{(j)(0)}, v_z^{(j)(0)})$  in the  $r$  and  $z$  directions respectively. The initial velocity in  $z$  is set by the electron beam energy,

$$v_z^{(j)(0)} = \sqrt{2U/m}, \quad (5)$$

where  $m$  is the electron rest mass. The initial velocity in  $r$  is zero, as the electron trajectories at  $z = 0$  are parallel to the  $z$  axis after passing through the anode aperture that acts as a diverging lens with focal length  $-4L_M$  [20, 22, 25, 30], giving

$$v_r^{(j)(0)} = 0. \quad (6)$$

From these initial conditions we use a fourth order Runge–Kutta method to trace each trajectory through the electric potential, calculating the position and velocity for successive time steps of  $h$  [40]. Details of this procedure are provided in Appendix A, and are similar to the approach used in Kan and Phaneuf [13]. Eventually, the  $j$ th electron exits the immersion lens at position  $(r^{(j)(exit)}, 0)$  with velocities  $(v_r^{(j)(exit)}, v_z^{(j)(exit)})$ . We account for the anode aperture deflection and trace back along the apparent straight line path of the electron to the virtual image plane  $z = \Delta f + 4L_M/3$  (Figs. 1 and 2), giving the virtual position of the  $j$ th ray,

$$\left( r^{(j)(exit)} - \left( \Delta f + \frac{4L_M}{3} \right) \left( \frac{v_r^{(j)(exit)}}{-v_z^{(j)(exit)}} + \frac{r^{(j)(exit)}}{4L_M} \right), \Delta f + \frac{4L_M}{3} \right). \quad (7)$$

The family of ray trajectories from a flat equipotential (i.e. unperturbed) specimen surface exit the anode aperture equally spaced at position  $jr_0$ , and will maintain an equal spacing  $S(\Delta f)$  when traced back to the image plane, with

$$S(\Delta f) = r_0 \left( \frac{2}{3} - \frac{\Delta f}{4L_M} \right). \quad (8)$$

We may calculate the image intensity on the plane  $\Delta f + 4L_M/3$  by considering the density of rays on this plane. This is inversely proportional to the ray spacing in  $r$ ,  $s(r, \Delta f)$  [41], given by the difference between  $r$  positions of adjacent rays in Eq. (7). Assuming an input intensity of unity, a ray spacing of  $s(r, \Delta f) = S(\Delta f)$  gives unit intensity. We therefore convert the family of ray trajectories into an intensity at any position on the plane

$\Delta f + 4L_M/3$  by dividing the unperturbed ray separation  $S(\Delta f)$  by the distance between adjacent rays  $s(r, \Delta f)$ , so giving [41]

$$I(r, \Delta f) = S(\Delta f)/s(r, \Delta f). \quad (9)$$

The image intensity may then be expressed as a one-dimensional profile in  $r$ , or as a two-dimensional plot by exploiting the cylindrical symmetry. Where initially adjacent rays cross ( $s \rightarrow 0$ ) the intensity is theoretically infinite, but in practice this results in a region of very high intensity, creating caustic features in the image [26, 27, 42]. Caustic surfaces, most of which are stable with respect to perturbation, are envelopes of ray families that may be classified into a variety of equivalence classes [27, 43]. Numerically, we may account for crossing rays by choosing a threshold ray spacing, e.g.  $s(r, \Delta f) = 0.1S(\Delta f)$ , below which from Eq. (9) we keep  $I \approx 10$ . This is equivalent to specifying the saturation level of the detector.

## 5. Caustic imaging of Ga droplets on GaAs (001)

As a specific application of caustic imaging theory we investigate liquid Ga droplets on GaAs (001). Such droplets are formed during Langmuir evaporation [9] and exhibit droplet surface dynamics with an unusual temperature dependence [8]. In particular, Ga droplets move on the rough GaAs (001) surface and leave behind smooth trails, as shown by the room temperature atomic force microscope (AFM) image in Fig. 3. An experimental through-focus MEM image sequence obtained at 660 °C during Langmuir evaporation is shown in Fig. 4. We now separately remark on the image contrast of the trails and droplets.

(a) *Trails.* The AFM data indicates that the droplet trails are typically shallow (15 nm) with slowly varying edges, so that Laplacian imaging theory is applicable and the MEM contrast can be interpreted in terms of surface curvature [25]. Specifically, the Laplacian imaging theory states that the image contrast is proportional to both  $\Delta f$  and to the transverse Laplacian of the local height profile  $H(x, y)$ , providing that  $H(x, y)$  is sufficiently slowly varying and/or  $\Delta f$  is sufficiently small [25]. At exact focus ( $\Delta f = 0$ ) the trail contrast vanishes.

(b) *Droplets.* The droplets, however, typically extend  $0.3 \mu\text{m}$  from the surface, which is many times larger than a typical electron turning distance ( $\delta = 40 \text{ nm}$ ) from the cathode. This produces significant perturbations

of the electric field creating caustic features for a wide range of defocus values. At negative defocus the image consists of a bright caustic ring  $C_R$  bordering a dark central region (see [8]). For large positive defocus, a very bright central caustic region is visible. Close to  $\Delta f = 0$  there is still strong droplet contrast visible exhibiting a transition between the two extremes. This illustrates the breakdown of Laplacian imaging theory [25] and we therefore apply caustic imaging theory to understand droplet image contrast.

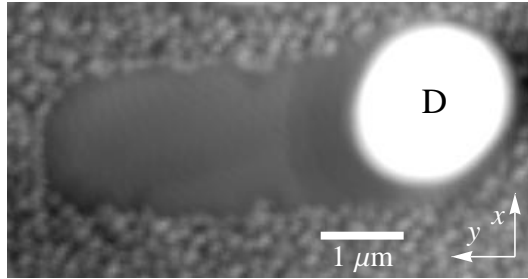


Figure 3: AFM image of a liquid Ga droplet D and the smooth trail it leaves on a GaAs (001) surface [25]. The shape of the droplet is well-approximated by a spherical cap.

## 6. Electric potential due to a liquid surface droplet

We evaluate the perturbing potential by modelling the droplet height  $H$  as a cylindrically symmetric spherical cap shown in Fig. 5, which is in good agreement with AFM measurements of solidified droplets (Fig. 3). This equilibrium shape is characterized by the projected radius  $R$  and the contact angle  $\Theta$ ,

$$H(0 \leq r \leq R) = \sqrt{\frac{R^2}{\sin^2 \Theta} - r^2} - \frac{R}{\tan \Theta}, \quad H(r > R) = 0, \quad (10)$$

as shown in Fig. 5. We use dimensions  $R = 0.78 \mu\text{m}$ ,  $\Theta = 36^\circ$  and  $H(0) = 0.25 \mu\text{m}$  for a typical droplet as imaged by AFM. Since the droplet consists of almost pure Ga, it may also be at a different potential to the GaAs (001) cathode, due to having a different surface work function [3, 44]. Massies *et al.* [44] indicate that the work function difference between the Ga droplet and the GaAs surface is in the range of 0.1 V to 0.3 V.

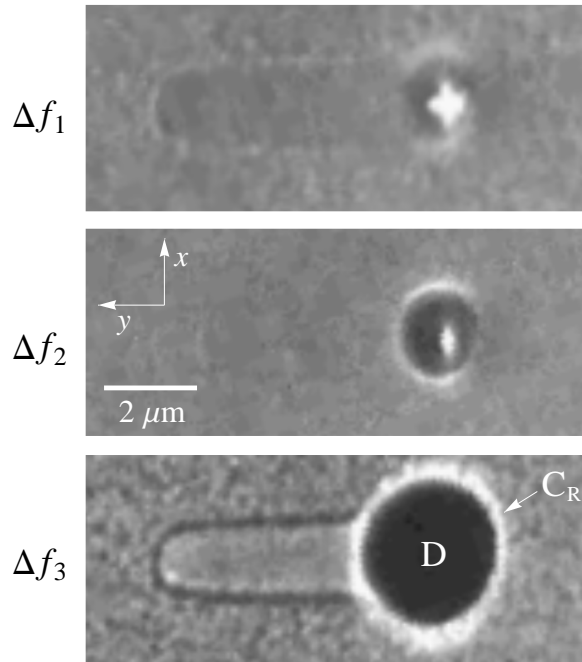


Figure 4: Experimental MEM images of a liquid Ga droplet marked D and the smooth trail it leaves on a GaAs (001) surface, for defoci  $\Delta f_1 = 16 \mu\text{m}$ ,  $\Delta f_2 = 0$ , and  $\Delta f_3 = -78 \mu\text{m}$ . Note the caustic ring  $C_R$  bordering a dark central region D in the bottom panel. Images were obtained using an Elmitec LEEM III system at  $660 \text{ }^\circ\text{C}$ .  $U = 20 \text{ keV}$  and  $V = -20000.4 \text{ V}$  which, for  $L = 2 \text{ mm}$ , gives a turning distance of  $\delta = 40 \text{ nm}$ .

We solve Laplace's equation (Eq. (2)) in the region  $0 \leq r \leq 100 \mu\text{m}$  and from  $L - 120 \mu\text{m} \leq z \leq L$  using the finite element methods package FreeFem++ v3.9-0 [39], using mesh adaptation with an interpolation error level of  $5 \times 10^{-6}$  (see the end of Appendix A for a discussion on suitable computational parameters). The bottom boundary follows the height profile of Eq. (10) and has a potential of  $V = -20000.4 \text{ V}$  outside the droplet and  $-20000.7 \text{ V}$  at the droplet boundary to account for a work function difference of  $0.3 \text{ V}$ . The top boundary has the potential expected for the unperturbed potential (Eq. (3))  $\phi_U(z = L - 120 \mu\text{m}) = -18800.376 \text{ V}$  with  $L = 2 \text{ mm}$ . The  $r = 0$  and  $r = 100 \mu\text{m}$  boundaries are kept open, and the model assumes that the equipotential lines will be perpendicular to these boundaries. This ensures that the system is rotationally symmetric about the axis  $r = 0$ , and demands that the perturbations to the potential caused

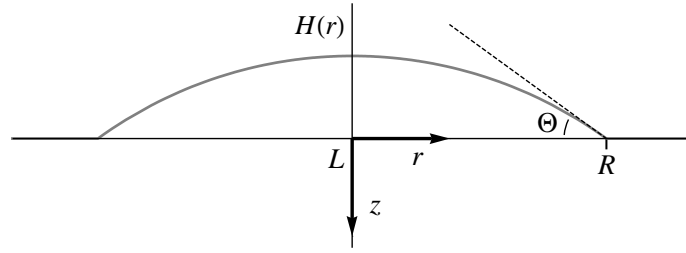


Figure 5: The droplet is modelled as a spherical cap (Eq. (10)), with projected radius  $R$  and contact angle  $\Theta$ .

by the droplet are zero at the chosen distance of  $r = 100 \mu\text{m}$ . The boundaries and mesh are shown in Fig. 6, and the resulting equipotential lines close to the droplet surface are shown in Fig. 7 for a work function of 0.3 V.

## 7. Caustic image simulation of a Ga droplet

To simulate the MEM contrast of a Ga droplet we employed the methods of section 4, inputting 201 rays at  $z = 0$  from  $r = 0 \mu\text{m}$  to  $r = 4.5 \mu\text{m}$  which gives an equal spacing of  $r_0 = 22.5 \text{ nm}$ . Using a fourth order Runge–Kutta method (Appendix A) with a sufficiently small time step of  $h = 5 \times 10^{-14} \text{ s}$ , we propagated each ray through the electric field, and then traced the exiting electron trajectories back along the apparent straight line paths to  $z = \Delta f + 4L_M/3$  using Eq. (7). The resulting distribution of electron ray trajectories is shown in Fig. 8 for  $-100 \mu\text{m} \leq \Delta f \leq 100 \mu\text{m}$ , where positive  $\Delta f$  is in the positive  $z$  direction (Fig. 1). Accompanying grey scale image simulations are shown for indicated defocus values.

The distribution of the envelope of electron ray trajectories and accompanying image simulations in Fig. 8 displays three distinct regimes of caustic features which accurately reproduce and explain the experimental through focus sequence in Fig. 4. For negative defocus, the contrast is dominated by a bright fold caustic ring  $C_R$  bordering a dark central region, with diameter increasing with negative defocus. For positive defocus, we expect a very bright central spot associated with the central cusp caustic evident in the ray tracing. For defocus values close to zero, we see a transition between the two extremes, where both a bright ring and bright central spot coexist. Note that the contrast close to zero defocus is not explainable

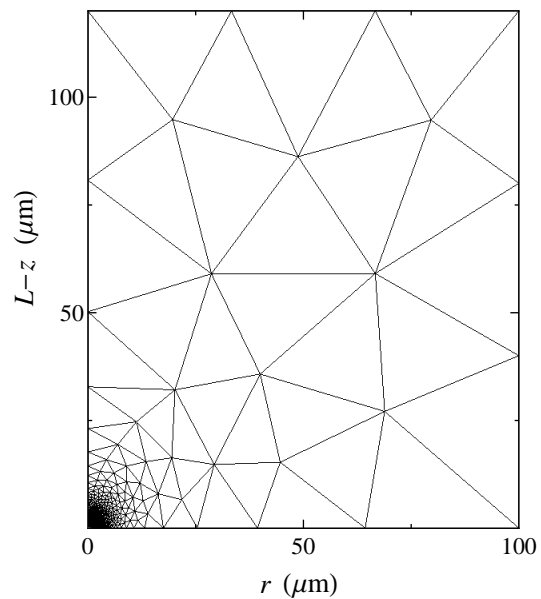


Figure 6: Boundaries and adapted mesh used to solve Laplace's equation (Eq. (2)) above the droplet surface with the FreeFem++ v3.9-0 package [39]. Note that the base of the droplet, as shown in Fig. 5, extends out to  $r = 0.78 \mu\text{m}$ .

with Laplacian imaging theory [25], which predicts zero image contrast. Caustic imaging theory may therefore be used to interpret and understand the image features of specimens that significantly perturb the electric field close to the sample. We now consider the potential utility of caustic imaging theory in recovering surface structural information from experimental MEM images.

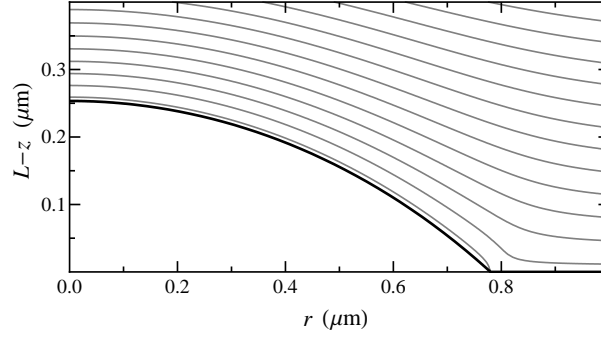


Figure 7: Equipotential surfaces above a Ga droplet on GaAs (001) evaluated from Eq. (2). A work function difference of 0.3 V exists between the droplet surface (black line) and the planar GaAs (001) surface ( $L-z = 0$  axis). The droplet and GaAs (001) surfaces are therefore at  $-20000.7$  V and  $-20000.4$  V respectively. Equipotential surfaces, beginning at  $-20000.6$  V and increasing by 0.3 V, are indicated by the grey lines.

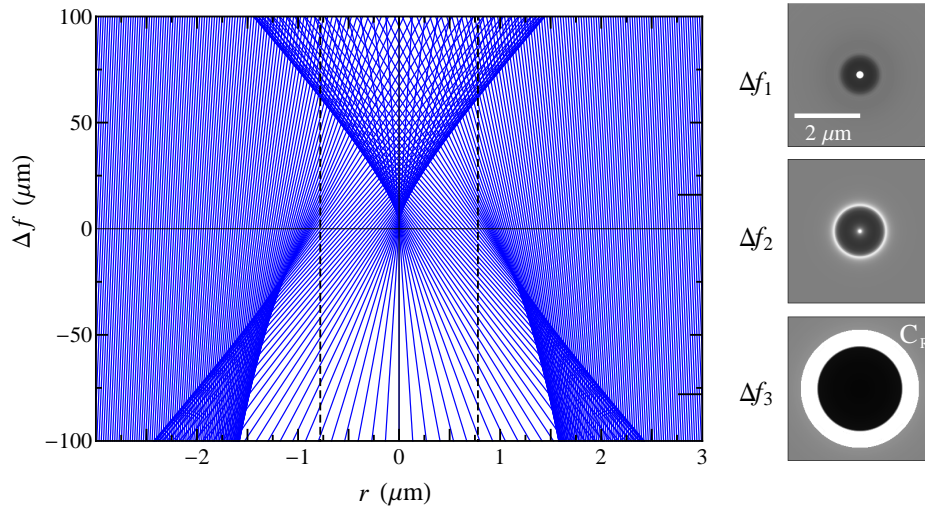


Figure 8: Distribution of the family of electron ray trajectories on the imaging plane  $z = \Delta f + 4L_M/3$ , after interaction with the electric field above a Ga droplet on GaAs (001) (solid lines). The defocus  $\Delta f$  is positive in the positive  $z$  direction (see Fig. 1). The  $r$  positions have been multiplied by  $3/2$  so that the virtual image plane matches the transverse scale of the specimen (see Fig. 2). The projected radius of the droplet,  $R = 0.78 \mu\text{m}$  is indicated by vertical dashed lines. (Right panels) two dimensional image simulations calculated from Eq. (9) are shown for  $\Delta f_1 = 16 \mu\text{m}$ ,  $\Delta f_2 = 0 \mu\text{m}$ , and  $\Delta f_3 = -78 \mu\text{m}$ , and show good agreement with the experimental images of Fig. 4. Color online.

## 8. Recovering surface topography from experimental MEM images

Caustic imaging theory provides a direct link between strong image features in experimental MEM images and the electric field distortions produced by specimen surface and/or potential variations. Understanding the “forward problem” of caustic formation allows one to broach the associated “inverse problem” of extracting structural information from the caustics present in a through-focus series of images. As a particular example of this inverse problem of caustic imaging, here we show how to determine the contact angle  $\Theta$  (Fig. 5) of a Ga droplet during Langmuir evaporation of GaAs (001).

As noted earlier, a running droplet of Ga leaves a shallow trail on GaAs (001) as shown in Fig. 3. We can apply Laplacian imaging theory [25] to the trail image contrast in Fig. 4 to estimate the trail width as  $1.56 \pm 0.02 \mu\text{m}$ . This utilises the approximately symmetrical change in the width of the trail contrast for defocus values close to and either side of zero, and therefore fixes the droplet projected radius  $R = 0.78 \pm 0.01 \mu\text{m}$ . We can also compare the features of the simulated trail contrast using caustic imaging theory to the MEM images to calibrate the relationship between the magnetic objective lens defocus and the lens current. The weaker contrast trail region therefore provides a useful reference to help quantify the droplet contrast. In general, however, there may not exist a convenient object for defocus calibration. In such cases, and as an alternative to the method outlined above, Schmidt *et al.* [45] have derived an expression relating defocus and experimental parameters including objective lens current.

Since the droplet has a spherical cap geometry, with  $R$  known, it is only necessary to determine  $\Theta$  to fully reconstruct the droplet shape. To determine the contact angle we select a caustic feature in the experimental images and compare this with simulation for a range of defocus values. The radius  $R_D$  of the dark central region bounded by the bright caustic in Fig. 9 is an excellent candidate since: (i) it is well defined, (ii) it is a sharp feature of intrinsically high visibility, and (iii) it varies monotonically with defocus in the range  $-140 \mu\text{m} < \Delta f < -30 \mu\text{m}$ .

Simulated values of  $R_D$  as a function of  $\Delta f$  are displayed in Fig. 10 for different values of contact angle. Here, we have assumed a work function difference of 0.3 V between the droplet and GaAs (001) surface. Exper-

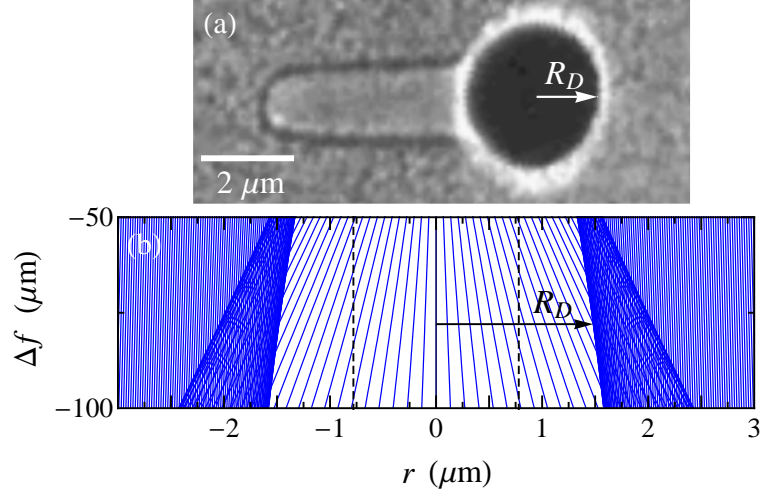


Figure 9: Radius of the dark central region bounded by the bright fold caustic,  $R_D$ , is shown on (a) an experimental MEM image and (b) a family of simulated rays. Colour online.

imental measurements of  $R_D$  are overlaid on this plot which fixes the contact angle to be  $38 \pm 3^\circ$ . This is in excellent agreement with the *ex situ* AFM measurement of  $36^\circ$  with standard deviation of  $2^\circ$  for typical Ga droplets, and demonstrates that caustic imaging can provide quantitative topographical data. Note that introducing a lower work function will affect the simulated  $R_D$  values and increase our estimate of  $\Theta$ . However, the maximum increase is only 4 degrees for the limiting case of zero work function difference. If the uncertainties are added in quadrature, we measure the contact angle to be  $38 \pm 7^\circ$ .

The effects of spherical aberration of the magnetic objective lens on the simulated images can be estimated using the exit angle of the electron,  $\alpha$ , as it emerges from the anode aperture. The tangent of this angle is given by

$$\tan \alpha = \frac{v_r^{(j)(exit)}}{-v_z^{(j)(exit)}} + \frac{r^{(j)(exit)}}{4L_M}, \quad (11)$$

using the terminology of Eq. (7). We estimate the change to the transverse

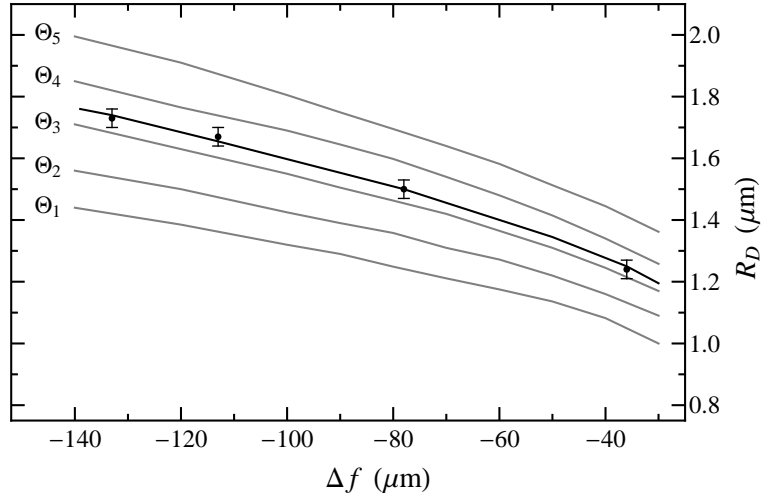


Figure 10: Simulated radius of the dark central region  $R_D$  for MEM images at negative defocus, for Ga droplets of projected radius  $0.78 \mu\text{m}$ , work function difference  $0.3 \text{ V}$ , and contact angles  $\Theta_1 = 15^\circ$ ,  $\Theta_2 = 25^\circ$ ,  $\Theta_3 = 35^\circ$ ,  $\Theta_4 = 45^\circ$ , and  $\Theta_5 = 55^\circ$  (grey lines). Measured experimental radius values, with uncertainty of  $\pm 0.03 \mu\text{m}$ , are overlaid and the line of best fit is shown as the black line.

position  $\Delta r$  of an electron in the vicinity of the virtual image plane  $z = 4L_M/3$  via [22, 46]

$$\Delta r = C_S \alpha^3, \quad (12)$$

where  $C_S$  is the spherical aberration coefficient. This can be directly incorporated into Eq. (7), by adding the approximate shift  $\Delta r$  to each ray's virtual position (Eq. (7)). We have simulated the ray envelope with  $C_S = 0.1 \text{ m}$  [22, 25, 45], and find that for the ray trajectories that determine the radius of the dark central region  $R_D$ , the change in position due to spherical aberration  $\Delta r$  is less than  $5 \text{ nm}$ , so spherical aberration for  $C_S \leq 0.1 \text{ m}$  has a negligible effect on the results of Fig. 10. The small number of rays with the largest angle  $\alpha$ , which determine the outer edge of the caustic ring  $C_R$  in Fig. 8, are estimated to be shifted by as much as  $50 \text{ nm}$ , but this does not affect the determination of the contact angle using the method outlined here. We may also include the effects of chromatic aberration by taking a weighted average of a series of monochromatic intensity patterns for a spread of energy values [25, 47]. For a Gaussian energy spread of full-width half-maximum  $0.3 \text{ eV}$ , we find that the effect on the image intensity for the low resolution case considered here is very small ( $< 1 \%$ ).

The capability to extract three-dimensional topographical or surface potential information from surface electron microscopy is extremely valuable. Experiments can be undertaken at elevated temperatures during material deposition under ultra high vacuum (UHV) conditions. Surface features such as contact angles can in principle be determined *in situ* from caustic features as a function of external conditions, provided the conditions do not vary rapidly on the time scale of a through-focus series which typically takes only a few seconds to acquire. By mapping several different caustic features as a function of defocus it should be possible to eliminate defocus entirely from the structure determination and/or extend the method to more complex geometries.

## 9. Multi-dimensional caustic imaging

We saw particular caustics in Fig. 8, namely cusp and fold caustics, fully unfolded [27] in a control space coordinatised by the transverse spatial coordinate  $r$  and a single control parameter  $\tau = \Delta f$ . More generally, one could have higher-dimensional caustics (e.g. the hyperbolic umbilic, the elliptic umbilic, the parabolic umbilic, etc. [43]). Since such higher-dimensional caustics require more than two dimensions for a full unfolding, the previously mentioned through-focal series  $I(r, \tau = \Delta f)$  might be replaced with the more general control-parameter series  $I(x, y, \tau_1, \tau_2, \dots)$ ; here  $(x, y)$  are Cartesian coordinates in the detector plane perpendicular to the optical axis  $z$ , and  $(\tau_1, \tau_2, \dots)$  denote a suitable set of continuously-variable control parameters such as defocus, cathode potential, electron energy, etc. For a given image series, the number of parameters in the set  $(x, y, \tau_1, \tau_2, \dots)$  will ideally be equal to the dimension of the space required for a full unfolding of the caustic being imaged.

Regarding the inverse problem, of determining surface structure from a given MEM caustic in the image series  $I(x, y, \tau_1, \tau_2, \dots)$ , the approach of Fig. 10 may be generalised as follows. Suppose one has an *a priori* model of the structure of interest (cf. Fig. 5), which is parameterized by a suitably small set of numbers  $(\Theta_1, \Theta_2, \dots)$ . Suppose, further, that in a given experiment one has measured the MEM caustic surfaces in  $I(x, y, \tau_1, \tau_2, \dots)$ . Importantly, such caustic surfaces are intrinsically of high visibility, and will therefore typically dominate image contrast. Under a suitable error metric, let  $\mathcal{E}[(\Theta_1, \Theta_2, \dots); I(x, y, \tau_1, \tau_2, \dots)]$  denote the mismatch between

the measured MEM caustic surfaces in  $I(x, y, \tau_1, \tau_2, \dots)$ , and the caustic surfaces which result when one evaluates the forward problem for the specified model as a function of  $(\Theta_1, \Theta_2, \dots)$ . The inverse problem of caustic imaging is then reduced to the multi-dimensional optimisation problem of finding the particular set of parameters  $(\Theta_1, \Theta_2, \dots)$  which minimise  $\mathcal{E}$ . Many numerical algorithms exist for such a multi-dimensional optimisation problem, see for example Chapter 10 of Press *et al.* [40]. Note, moreover, that such optimisations might also be carried out over data spaces with dimension smaller than that required for a full caustic unfolding, a particular example of which was given in Fig. 10.

## 10. Conclusions

We have demonstrated that a caustic dominated imaging theory can be usefully applied to interpret MEM contrast from surface topography (and/or surface potential) variations which appreciably distort the electric field above the specimen surface. The method obtains the electric potential above the specimen by numerically solving Laplace's equation. A family of electron ray trajectories is then numerically propagated through the electric field close to the specimen surface to obtain the electron distribution in the objective lens image plane. The resulting contrast may include strong image features where one has envelopes of overlapping rays, evident as bright caustic regions. Such caustics can be related to the specimen topography and/or potential and may be used to recover quantitative surface topographical information.

## Acknowledgments

We are grateful to Rod Mackie for technical support. S.M.K. acknowledges funding from the J. L. William Bequest. D.M.P., W.X.T. and D.E.J. acknowledge funding from the Australian Research Council via the Discovery-Projects programme.

## Appendix A. Fourth order Runge–Kutta method

The fourth order Runge–Kutta method is one of several methods that may be used to evaluate the electron path through the electric field (see the discussion and references in [38, 40]). Assuming rotational symmetry in cylindrical polar coordinates, at time  $t$  the  $j$ th electron is at  $(r^{(j)(t)}, z^{(j)(t)})$  with velocity  $(v_r^{(j)(t)}, v_z^{(j)(t)})$ . We estimate the new electron location and

velocity at time  $t + h$  using classical kinematic equations of motion. The fourth order Runge–Kutta method in essence estimates the average velocity in  $r$  and  $z$  over the time interval from  $t$  to  $t + h$ , and then multiplies this average velocity by  $h$  to obtain the new position in  $r$  and  $z$ . In the  $r$  direction, for example, the equation of motion is

$$v_{r,f} = v_{r,i} + \Delta t a_{r,av}(r, z), \quad (\text{A.1})$$

where  $v_{r,f}$  is the final velocity,  $v_{r,i}$  is the initial velocity, the acceleration  $a_r$  is

$$a_r(r, z) = -\frac{e}{m} \frac{\partial \phi(r, z)}{\partial r}, \quad (\text{A.2})$$

and  $a_{r,av}$  is the average acceleration over the time interval  $\Delta t$ . Where the acceleration is constant at all points  $(r, z)$ , Eq. (A.1) is trivial to apply. However where  $a_r(r, z)$  and  $a_z(r, z)$  vary with  $(r, z)$ , we use the fourth order Runge–Kutta method to generate a series of estimates of the acceleration and velocity over the time from  $t$  to  $t + h$ ,

$$\begin{aligned} vr_1 &= v_r^{(j)(t)}, & vz_1 &= v_z^{(j)(t)}, \\ vr_2 &= v_r^{(j)(t)} + (h/2)(-e/m) \left[ \frac{\partial \phi(r, z)}{\partial r} \right]_{(r=r^{(j)(t)} + (h/2)vr_1, z=z^{(j)(t)} + (h/2)vz_1)}, \\ vz_2 &= v_z^{(j)(t)} + (h/2)(-e/m) \left[ \frac{\partial \phi(r, z)}{\partial z} \right]_{(r=r^{(j)(t)} + (h/2)vr_1, z=z^{(j)(t)} + (h/2)vz_1)}, \\ vr_3 &= v_r^{(j)(t)} + (h/2)(-e/m) \left[ \frac{\partial \phi(r, z)}{\partial r} \right]_{(r=r^{(j)(t)} + (h/2)vr_2, z=z^{(j)(t)} + (h/2)vz_2)}, \\ vz_3 &= v_z^{(j)(t)} + (h/2)(-e/m) \left[ \frac{\partial \phi(r, z)}{\partial z} \right]_{(r=r^{(j)(t)} + (h/2)vr_2, z=z^{(j)(t)} + (h/2)vz_2)}, \\ vr_4 &= v_r^{(j)(t)} + h(-e/m) \left[ \frac{\partial \phi(r, z)}{\partial r} \right]_{(r=r^{(j)(t)} + hvr_3, z=z^{(j)(t)} + hvz_3)}, \\ vz_4 &= v_z^{(j)(t)} + h(-e/m) \left[ \frac{\partial \phi(r, z)}{\partial z} \right]_{(r=r^{(j)(t)} + hvr_3, z=z^{(j)(t)} + hvz_3)}, \\ r^{(j)(t+h)} &= r^{(j)(t)} + (h/6)(vr_1 + 2vr_2 + 2vr_3 + vr_4), \\ z^{(j)(t+h)} &= z^{(j)(t)} + (h/6)(vz_1 + 2vz_2 + 2vz_3 + vz_4). \end{aligned} \quad (\text{A.3})$$

Similarly, we may estimate the average acceleration over the time interval, and multiply this by  $h$  to obtain the new velocity in  $r$  and  $z$ . We use the classical kinematic equation of motion, in  $r$  for example,

$$r_f = r_i + v_{r,i}\Delta t + (a_{r,av}(r, z)/2)\Delta t^2, \quad (\text{A.4})$$

for final and initial points  $r_f$  and  $r_i$  respectively, to obtain the necessary points at which we evaluate the acceleration and obtain a weighted average,

$$\begin{aligned}
ar_1 &= (-e/m) \left[ \frac{\partial\phi(r,z)}{\partial r} \right]_{(r=r^{(j)}(t), z=z^{(j)}(t))}, \\
az_1 &= (-e/m) \left[ \frac{\partial\phi(r,z)}{\partial z} \right]_{(r=r^{(j)}(t), z=z^{(j)}(t))}, \\
ar_2 &= (-e/m) \left[ \frac{\partial\phi(r,z)}{\partial r} \right]_{(r=r^{(j)}(t) + (h/2)v_r^{(j)}(t) + (ar_1/2)(h/2)^2, \\
&\quad z=z^{(j)}(t) + (h/2)v_z^{(j)}(t) + (az_1/2)(h/2)^2)}, \\
az_2 &= (-e/m) \left[ \frac{\partial\phi(r,z)}{\partial z} \right]_{(r=r^{(j)}(t) + (h/2)v_r^{(j)}(t) + (ar_1/2)(h/2)^2, \\
&\quad z=z^{(j)}(t) + (h/2)v_z^{(j)}(t) + (az_1/2)(h/2)^2)}, \\
ar_3 &= (-e/m) \left[ \frac{\partial\phi(r,z)}{\partial r} \right]_{(r=r^{(i)}(t) + (h/2)v_r^{(j)}(t) + (ar_2/2)(h/2)^2, \\
&\quad z=z^{(j)}(t) + (h/2)v_z^{(j)}(t) + (az_2/2)(h/2)^2)}, \\
az_3 &= (-e/m) \left[ \frac{\partial\phi(r,z)}{\partial z} \right]_{(r=r^{(i)}(t) + (h/2)v_r^{(j)}(t) + (ar_2/2)(h/2)^2, \\
&\quad z=z^{(j)}(t) + (h/2)v_z^{(j)}(t) + (az_2/2)(h/2)^2)}, \\
ar_4 &= (-e/m) \left[ \frac{\partial\phi(r,z)}{\partial r} \right]_{(r=r^{(j)}(t) + hv_r^{(j)}(t) + (ar_3/2)h^2, \\
&\quad z=z^{(j)}(t) + hv_z^{(j)}(t) + (az_3/2)h^2)}, \\
az_4 &= (-e/m) \left[ \frac{\partial\phi(r,z)}{\partial z} \right]_{(r=r^{(j)}(t) + hv_r^{(j)}(t) + (ar_3/2)h^2, \\
&\quad z=z^{(j)}(t) + hv_z^{(j)}(t) + (az_3/2)h^2)}, \\
v_r^{(j)(t+h)} &= v_r^{(j)}(t) + (h/6)(ar_1 + 2ar_2 + 2ar_3 + ar_4), \\
v_z^{(j)(t+h)} &= v_z^{(j)}(t) + (h/6)(az_1 + 2az_2 + 2az_3 + az_4).
\end{aligned} \tag{A.5}$$

Typically, we expect that any perturbations to the electric field will approach zero far from the specimen (e.g.  $10^{-4}$  m), so we often need only solve for the electric field relatively close to the cathode variations. We may also, then, begin the Runge–Kutta method at some point  $z = z_1$  much closer to the cathode, minimising computation time. This also ensures that the final point of the trajectory is at  $z = 0$  as required, whereas a full Runge–Kutta treatment to  $z = 0$  would often overshoot the position  $z = 0$  due to the discrete size of the time step  $h$ .

The derivative of the electric potential  $\phi$  may be performed, for example, via the symmetric finite-difference approximation [40]

$$\partial\phi(r, z)/\partial r \approx (\phi(r + \Delta, z) - \phi(r - \Delta, z))/2\Delta. \tag{A.6}$$

Note that a smaller derivative step size  $\Delta$  will not always increase accuracy, as a  $\Delta$  that is too small may result in the difference  $(\phi(r+\Delta, z) - \phi(r-\Delta, z))$  being in the significant figures affected by numerical noise and/or rounding errors. For the examples in this paper,  $\Delta = 5 \times 10^{-9}$  m for  $z$  derivatives and  $\Delta = 10^{-7}$  m for  $r$  derivatives.

The choice of time step  $h$  follows similar constraints. If it is too large (e.g.  $10^{-12}$  s), the electron may pass beyond the classical turning point  $z = L_M$  and the boundary of the droplet, which disrupts the ray tracing method. If it is too small (e.g.  $10^{-15}$  s), computation time is greatly increased and the differences in position may occur only in the significant figures that are most strongly affected by numerical noise and/or rounding errors.

The choice of the parameters used in the FreeFEM++ solution of Laplace's equation (see section 6) will influence the accuracy of the simulations, as numerical errors in the electric potential solution will directly affect the simulated trajectories. In particular, the number of maximum mesh points allowed in the mesh adaption function must be sufficient to properly sample the variations of the electric field. For the droplet and trail considered here, the default FreeFEM++ maximum of 9000 mesh vertices was sufficient, but for a rapidly varying electric potential (e.g. sharp surface steps that are tens of nanometres apart) a higher maximum is required. Similarly, the mesh adaption error must be sufficiently small, so that the generated mesh samples the electric potential over an appropriately small scale where the potential varies over a short distance.

If these parameters are not well chosen, it is usually evident as large coarse areas of mesh, in asymmetry in the mesh pattern above a symmetrical specimen, and in the instability and roughness of the recovered equipotential surfaces. We therefore recommend examining plots of the mesh and equipotential surfaces above the specimen to ensure they are well behaved.

- [1] A. E. Luk'yanov, G. V. Spivak, R. S. Gvozdover, *Sov. Phys. Usp.* 16 (1974) 529 (doi:10.1070/PU1974v016n04ABEH005299).
- [2] A. B. Bok, in *Diffraction and Imaging Techniques in Material Science* (Eds. S. Amelinckx, R. Gevers & J. Van Landuyt), 2nd rev. edn., Amsterdam: North-Holland, 1978, pp. 761–788.

- [3] J. C. Dupuy, A. Sibai, B. Vilotitch, *Surf. Sci.* 147 (1984) 191 (doi:10.1016/0039-6028(84)90175-4).
- [4] J. Slezák, M. Ondřejček, Z. Chvoj, V. Cháb, H. Conrad, S. Heun, Th. Schmidt, B. Ressel, K. C. Prince, *Phys. Rev. B* 61 (2000) 16121 (doi:10.1103/PhysRevB.61.16121).
- [5] T. Shimakura, Y. Takahashi, M. Sugaya, T. Ohnishi, M. Hasegawa, H. Ohta, *Microelectron. Eng.* 85 (2008) 1811 (doi:10.1016/j.mee.2008.05.018).
- [6] S. A. Nepijko, G. Schönhense, *J. Microsc.* 238 (2010) 90 (doi:10.1111/j.1365-2818.2009.03340.x).
- [7] E. Hilner, A. A. Zakharov, K. Schulte, P. Kratzer, J. N. Andersen, E. Lundgren, A. Mikkelsen, *Nano Lett.* 9 (2009) 2710 (doi:10.1021/nl9011886).
- [8] J. Tersoff, D. E. Jesson, W. X. Tang, *Science* 324 (2009) 236 (doi:10.1126/science.1169546).
- [9] J. Tersoff, D. E. Jesson, W. X. Tang, *Phys. Rev. Lett.* 105 (2010) 035702 (doi:10.1103/PhysRevLett.105.035702).
- [10] M. E. Barnett, W. C. Nixon, *J. Sci. Instrum.* 44 (1967) 893 (doi:10.1088/0950-7671/44/11/302).
- [11] W. Świąch, B. Rausenberger, W. Engel, A. M. Bradshaw, E. Zeitler, *Surf. Sci.* 294 (1993) 297 (doi:10.1016/0039-6028(93)90116-2).
- [12] E. Bauer, *Surf. Rev. Lett.* 5 (1998) 1275 (doi:10.1142/S0218625X98001614).
- [13] H.-C. Kan, R. J. Phaneuf, *J. Vac. Sci. Technol. B* 19 (2001) 1158 (doi:10.1116/1.1385688).
- [14] S. A. Nepijko, N. N. Sedov, G. Schönhense, *J. Microsc.* 203 (2001) 269 (doi:10.1046/j.1365-2818.2001.00895.x).
- [15] C. C. Speake, C. Trenkel, *Phys. Rev. Lett.* 90 (2003) 160403 (doi:10.1103/PhysRevLett.90.160403).
- [16] M. E. Barnett, W. C. Nixon, *Optik* 26 (1967) 310.

- [17] A. J. Hermans, J. A. Petterson, *J. Eng. Math.* 4 (1970) 141 (doi:10.1007/BF01535086).
- [18] S. M. Kennedy, D. E. Jesson, M. J. Morgan, A. E. Smith, P. F. Barker, *Phys. Rev. A* 74 (2006) 044701 (doi:10.1103/PhysRevA.74.044701).
- [19] R. Godehardt, *Adv. Imag. Elect. Phys.* 94 (1995) 81 (doi:10.1016/S1076-5670(08)70144-7).
- [20] S. A. Nepijko, N. N. Sedov, *Adv. Imag. Elect. Phys.* 102 (1997) 273 (doi:10.1016/S1076-5670(08)70125-3).
- [21] S. A. Nepijko, A. Gloskovskii, N. N. Sedov, G. Schönhense, *J. Microsc.* 211 (2003) 89 (doi:10.1046/j.1365-2818.2003.01199.x).
- [22] G. F. Rempfer, O. H. Griffith, *Ultramicroscopy* 47 (1992) 35 (doi:10.1016/0304-3991(92)90184-L).
- [23] N. N. Sedov, *J. Microsc.-Paris* 9 (1970) 1.
- [24] T. Someya, J. Kobayashi, *Phys. Status Solidi (a)* 26 (1974) 325 (doi:10.1002/pssa.2210260134).
- [25] S. M. Kennedy, C. X. Zheng, W. X. Tang, D. M. Paganin, D. E. Jesson, *Proc. R. Soc. A* 466 (2010) 2857 (doi:10.1098/rspa.2010.0093). And *ibid.* Addendum, submitted in 2010.
- [26] M. V. Berry, in *Physics of Defects, Les Houches Lecture Series Session XXXV* (Eds. R. Balian, M. Kléman, J.-P. Poirier), Amsterdam: North-Holland, 1981, pp. 453–543.
- [27] J. F. Nye, *Natural Focusing and Fine Structure of Light: Caustics and Wave Dislocations*, Bristol: Institute of Physics Publishing, 1999, pp. 9–11, 46–48.
- [28] E. Bauer, *Ultramicroscopy* 17 (1985) 51–56 (doi:10.1016/0304-3991(85)90176-7).
- [29] E. Bauer, *Rep. Prog. Phys.* 57 (1994) 895 (doi:10.1088/0034-4885/57/9/002).
- [30] I. S. Grant, W. R. Phillips, *Electromagnetism*, 2nd edn., Chichester: John Wiley & Sons, 1990, pp. 100–103.

- [31] J. D. Jackson, *Classical Electrodynamics*, 3rd edn., New York: John Wiley & Sons, 1999, pp. 34–35, 111–112.
- [32] M. T. Boudjelkha, J. B. Diaz, *Appl. Anal.* 1 (1972) 297 (doi:10.1080/00036817208839020).
- [33] D. E. Jesson, K. M. Pavlov, M. J. Morgan, B. F. Usher, *Phys. Rev. Lett.* 99 (2007) 016103 (doi:10.1103/PhysRevLett.99.016103).
- [34] G. N. Polozhiy, *Equations of Mathematical Physics*, New York: Hayden Book Company, 1967, pp. 62–64, 149.
- [35] W. X. Tang, D. E. Jesson, K. M. Pavlov, M. J. Morgan, B. F. Usher, *J. Phys.: Condens. Matter* 21 (2009) 314022 (doi:10.1088/0953-8984/21/31/314022).
- [36] H. R. Lewis Jr., *J. Appl. Phys.* 37 (1966) 2541 (doi:10.1063/1.1782081).
- [37] G. Schönecker, R. Spehr, H. Rose, *Nucl. Instr. and Meth. A* 298 (1990) 360 (doi:10.1016/0168-9002(90)90638-M).
- [38] W. Wan, J. Feng, H.A. Padmore, D.S. Robin, *Nucl. Instr. and Meth. A* 519 (2004) 222 (doi:10.1016/j.nima.2003.11.159).
- [39] F. Hecht, O. Pironneau, A. Le Hyaric, J. Morice, *FreeFem++ version 3.9-0*, accessed June 2010, available from <http://www.freefem.org/ff++/>
- [40] W. H. Press, S. A. Teukolsky, W. T. Vetterling, B. P. Flannery, *Numerical Recipes, the Art of Scientific Computing*, 3rd edn., Cambridge: Cambridge University Press, 2007, pp. 229–232, 907–910, and chapter 10.
- [41] M. Born, E. Wolf, *Principles of Optics*, 7th (expanded) edn., Cambridge: Cambridge University Press, 2006, pp. 120–125.
- [42] M. V. Berry, in *Singular Optics*, SPIE proceedings (Ed. M. S. Soskin), vol. 3487, Bellingham, WA: SPIE International Society for Optical Engineering, 1998, pp. 1–5.
- [43] V. I. Arnol'd, in *Bifurcations and Catastrophe Theory* (Eds. V. I. Arnol'd, V. S. Afrajmovich, Yu. S. Il'yashenko, L. P. Shil'nikov, N. Kazarinoff), Berlin: Springer-Verlag, 1999, Ch. 2.

- [44] J. Massies, P. Etienne, F. Dezaly, N. T. Linh, *Surf. Sci.* 99 (1980) 121 (doi:10.1016/0039-6028(80)90582-8).
- [45] Th. Schmidt, H. Marchetto, P. L. Lévesque, U. Groh, F. Maier, D. Preikszas, P. Hartel, R. Spehr, G. Lilienkamp, W. Engel, R. Fink, E. Bauer, H. Rose, E. Umbach, H.-J. Freund, *Ultramicroscopy* 110 (2010) 1358 (doi:10.1016/j.ultramic.2010.07.007).
- [46] J. C. H. Spence, *High-Resolution Electron Microscopy*, 3rd edn., Oxford University Press, 2003, pp. 40–41.
- [47] S. M. Kennedy, N. E. Schofield, D. M. Paganin, D. E. Jesson, *Surf. Rev. Lett* 16 (2009) 855 (doi:10.1142/S0218625X09013402).

---

## Electron caustic lithography

5

This chapter is an author generated post print of the article

S. M. Kennedy, C. X. Zheng, J. Fu, W. X. Tang, D. M. Paganin and D. E. Jesson, *Electron caustic lithography*, AIP Advances, 2 (2012) 022152, available electronically at [http://aipadvances.aip.org/resource/1/aaidbi/v2/i2/p022152\\_s1](http://aipadvances.aip.org/resource/1/aaidbi/v2/i2/p022152_s1).

## Declaration for Thesis Chapter "Electron caustic lithography"

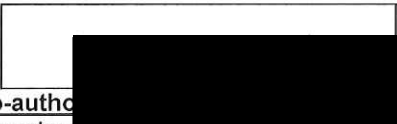
Declaration by candidate

For this chapter, the nature and extent of my contribution to the work was the following:

Nature of contribution	Extent of contribution(%)
Designed and performed the FIB and MEM experiments, provided technical expertise and co-wrote the paper.	45

The following co-authors contributed to the work. Co-authors who are students at Monash University must also indicate the extent of their contribution in percentage terms

Name	Extent of contribution(%)	Nature of contribution
Shane Kennedy	45	Performed the image simulations, co-wrote the paper.
Jing Fu		provided technical expertise.
Wen-XinTang		provided technical expertise.
David Paganin		Co-developed the model and provided technical expertise.
David Jesson		Co-wrote the paper, Co-developed the model and provided technical expertise.

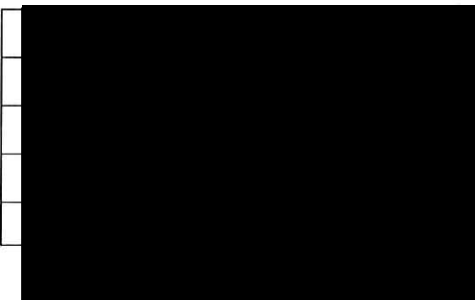
Candidate's signature		Date	24-08-12
-----------------------	---	------	----------

**Declaration by co-authors**

The undersigned hereby certify that:

- (1) they meet the criteria for authorship in that they have participated in the conception, execution, or interpretation, of at least that part of the publication in their field of expertise;
- (2) they take public responsibility for their part of the publication, except for the responsible author who accepts overall responsibility for the publication;
- (3) there are no other authors of the publication according to these criteria;
- (4) potential conflicts of interest have been disclosed to (a) granting bodies, (b) the editor or publisher of journals or other publications, and (c) the head of the responsible academic unit; and
- (5) the original data are stored at the following location(s) and will be held for at least five years from the date indicated below:

Location(s)	School of Physics, Monash University, Clayton
-------------	---

Signature 1		Date	23-08-12
Signature 2			24-08-12
Signature 3			21-08-12
Signature 4			24-08-2012
Signature 5			21-08-12

## Electron caustic lithography

S. M. Kennedy<sup>1</sup>, C. X. Zheng<sup>1</sup>, J. Fu<sup>2</sup>, W. X. Tang<sup>1</sup>, D. M. Paganin<sup>1</sup>, and D. E. Jesson<sup>1\*</sup>

<sup>1</sup>*School of Physics, Monash University, Victoria, 3800, Australia and*

<sup>2</sup>*Department of Mechanical and Aerospace Engineering,*

*Monash University, Victoria, 3800, Australia*

### Abstract

A maskless method of electron beam lithography is described which uses the reflection of an electron beam from an electrostatic mirror to produce caustics in the demagnified image projected onto a resist-coated wafer. By varying the electron optics, e.g. via objective lens defocus, both the morphology and dimensions of the caustic features may be controlled, producing a range of bright and tightly focused projected features. The method is illustrated for line and fold caustics and is complementary to other methods of reflective electron beam lithography.

## I. INTRODUCTION

Electron optical systems have emerged as attractive candidates for high resolution lithography.<sup>1,2</sup> Direct-write e-beam lithography (EBL) utilising scanning electron microscopy (SEM), for example, is of significant value in laboratory based nanofabrication.<sup>2-6</sup> However, the serial nature of this inherently scanning technique renders it too slow for high-throughput industrial applications involving large scale circuits.<sup>1,3,7</sup> Projection methods utilising a parallel electron beam and mask can, in principle, overcome such patterning speed limitations.<sup>2,7-13</sup> However, significant demands are placed on the design of the electron mask due to the requirement of sufficiently high aspect ratio between thick/thin regions which absorb/transmit electrons.<sup>3</sup> This has limited the approach to stencil masks and low energy electrons, compromising the attainable resolution.<sup>2</sup>

The mask limitation is therefore a serious issue in the application of projection electron lithography methods. This has led to innovative approaches such as SCALPEL which utilises the angular scattering properties of electrons, rather than absorption in the mask, to create intensity variations across a resist.<sup>2,8,9,11</sup> In addition there has been a development of maskless approaches, including the use of multiple beams,<sup>14,15</sup> low energy electron microscopy,<sup>10</sup> and reflective electron beam lithography (REBL) wherein the electron beam is reflected by an array of electrostatic mirrors.<sup>12,13</sup> In this letter we describe a complementary approach to REBL and electron projection lithography which is based on the formation of intense electron caustics which can be subsequently projected onto a resist by suitable electron optics. The caustics are formed within the cathode lens of a mirror electron microscope (MEM) in which electrons turn around in the vicinity of a negatively biased specimen surface.<sup>16-18</sup> Rather than using an array of individually controlled electrostatic mirrors as in REBL, a single mirror surface is lithographically patterned to create perturbations in the uniform electric field above the specimen which can be used to form caustics. This perturbed electric potential mirror therefore entirely replaces the conventional mask and specific caustics can be tuned by the patterning and subsequently projected onto a resist coated wafer. The method has the advantage that for a given lithographically patterned mirror surface, the caustic pattern projected onto the resist can be varied by simply adjusting the electron optics, e.g. the objective lens defocus.

Caustics are regions of very high intensity created naturally by focusing optics. For example, the sharp bright lines on the floor of a swimming pool are formed by sunlight shining through the perturbed water surface. As caustics are regions of very high intensity, reflected electron caustics projected onto a resist-coated wafer would apply a high electron dose to the resist producing a strong response. A variety of caustic classes can be formed in MEM.<sup>19</sup> Here we consider line and fold caustics which produce bright focused points and lines respectively when projected onto a resist. These caustic features form the basic building blocks or elements of a projected lithographic pattern, and can include more complex caustic classes such as an elliptic umbilic, which could form a three way junction element. Importantly, caustics are typically sharper and finer than the mirror surface variations producing them. In the analogy of swimming pool caustics, a gently perturbed water surface produces much finer caustics on the swimming pool floor. The combination of bright and finely focused features therefore makes caustic mirrors of significant value to EBL.

## II. ELECTRON CAUSTIC LITHOGRAPHY

The proposed experimental arrangement for mirror electron caustic lithography (ECL) is shown in Fig. 1. An electron beam is directed into the immersion objective lens providing parallel illumination of the cathode, which is negatively charged so that the electron beam turns around above the surface. Variations in the cathode surface topography and/or potential result in a varying electric field close to the surface, which deflect the electron beam in the vicinity of the turn-around region. These deflections and distortions create caustics in the returning electron beam, which in Fig. 1 is demagnified and directed onto a resist such that the cathode is acting as a caustic mirror (CAM). As a proof of concept, we now consider two examples of CAMs which produce point, circular, and line elements of a projected lithographic pattern.

As a first example of a CAM, we consider circular microholes in a GaAs surface which produce line and fold caustics as shown in Fig. 2(a)–(c). As discussed by Kan and Phaneuf,<sup>20</sup> microholes act to focus the reflected electron beam forming very bright central spots, which

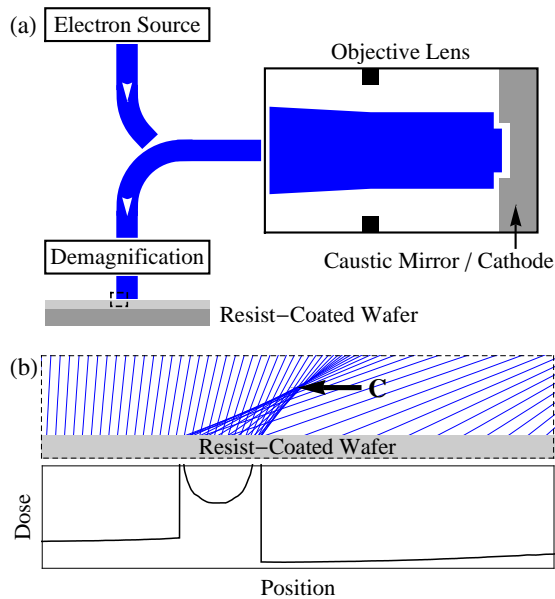


FIG. 1. (a) Proposed experimental arrangement for mirror electron caustic lithography (ECL). The electron beam (blue line) provides parallel illumination of the cathode specimen. The electron beam is slowed by the electric field in the region above the cathode, and the cathode is negatively charged so that the electron beam turns around just before the surface. The electron beam interacts with and is deflected by the electric field above the cathode surface, is reaccelerated away, and carries these distortions back through the system to the resist. (b) Electron ray trajectories (blue lines) projected onto the resist-coated wafer (dashed box in (a)). Where initially adjacent electron rays cross (marked by arrow) a caustic  $C$  is formed, creating a focused region of very high intensity and high dose to the resist.

are seen experimentally in Fig. 2(a). These are line caustics,<sup>19</sup> and are evident as bright spots when projected onto the resist. Decreasing the objective lens current introduces darker circular regions around the diminished central spots. Fold caustics form at the edges of these darker regions, which are evident as bright circular outer rings in Fig. 2(b). As objective lens current is further decreased, the central spot or line caustic fades, leaving larger darker central regions with fold caustics or bright circular boundaries in Fig. 2(c). These begin to overlap with the images of adjacent microholes, eventually becoming a grid of vertical and horizontal bright lines.

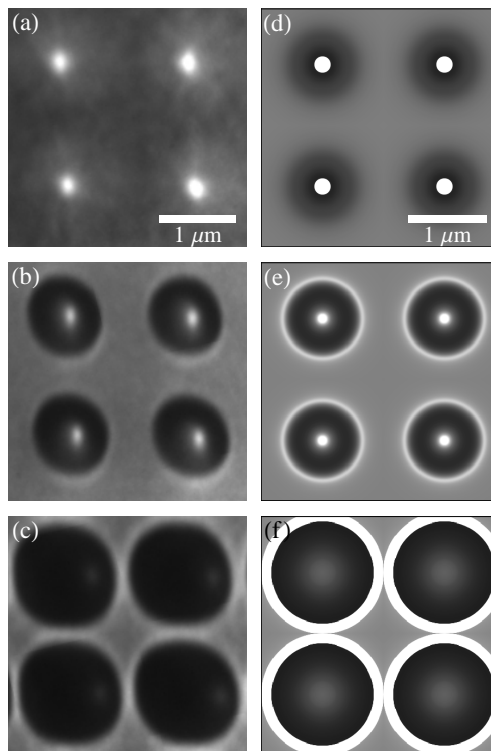


FIG. 2. Experimental and simulated MEM images of a grid of circular microholes in a GaAs surface of diameter 600 nm and depth 200 nm, formed by focused ion beam (FIB) techniques. The experimental images are taken with varying objective lens current i.e. defocus providing a through-focus sequence of images. The electron energy is  $U = 20$  keV, the specimen voltage is  $V = -20000.4$  V, and the anode-cathode separation is  $L = 2$  mm so that the electron beam turns approximately 40 nm above the surface. The objective lens current is (a) 1670 mA, (b) 1650 mA, (c) 1640 mA, and the defocus for the simulated images is (d)  $-20$   $\mu\text{m}$ , (e)  $10$   $\mu\text{m}$ , and (f)  $50$   $\mu\text{m}$ .

The range of caustic shapes of varying sizes and intensities produced in ECL may be understood using the recently developed caustic imaging theory.<sup>21-23</sup> This approach interprets caustic features as the natural result of electron redistribution created by the perturbed electric field above the cathode surface. In Fig. 3 we show the simulated positions of initially equidistant electrons that are projected onto the resist with objective lens defocus  $\Delta f$ . This simulated electron ray family shows the formation of a central line caustic in the vicinity of  $\Delta f = -5$   $\mu\text{m}$  and the surrounding fold caustic for  $\Delta f > 25$   $\mu\text{m}$ , where initially

adjacent electron ray paths overlap. By comparing the spacing of originally adjacent rays to the original spacing at a specific defocus (solid horizontal lines in Fig. 3), we may simulate the projected caustic features<sup>21–23</sup> as shown in Fig. 2(d)–(f). The simulated caustics are in good agreement with experimental caustics, and further highlights that by varying the objective lens current (i.e. defocus) we can control both the dimensions and the type of caustic features that are produced. The caustic imaging theory can be used to simulate and predict the caustics that will be produced in MEM, and so develop a suitable CAM to produce the desired lithographic pattern.

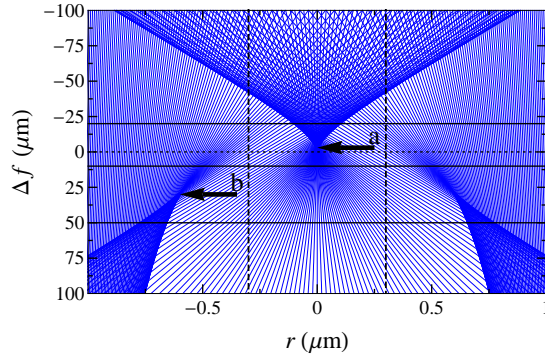


FIG. 3. Simulated electron ray path positions projected onto the resist, having reflected from a caustic mirror of a surface hole in GaAs, for defocus  $\Delta f$  which is controlled by the objective lens current. A line caustic is formed at the region marked ‘a,’ a fold caustic at the region marked ‘b,’ these caustics are regions of strongly enhanced electron intensity. The mirror or cathode surface is held at a potential of  $V = -20000.4$ , the electron energy is  $U = 20$  keV, and the cathode–anode distance is  $L = 2$  mm. The edges of the circularly symmetrical hole are indicated by vertical dashed lines. The  $r$  positions of the rays were multiplied by  $3/2$  to remove the demagnification of the anode aperture as discussed in Kennedy *et al.*<sup>21</sup> The horizontal solid lines are the positions of the projected image plane for the images in Fig. 2.

In order to create line elements in a lithographic pattern, consider a raised ridge or wire on the mirror surface as depicted in cross section in Fig. 4(a). Simulated MEM images indicate that this mirror surface produces both double and single fold caustics, producing lines in the projected image (Fig. 4(b) and (c) respectively), with the type, position and intensity

of the caustics varying with the electron optics of the MEM system. These caustic features are similar to those experimentally obtained from a nanowire on a planar surface.<sup>23</sup>

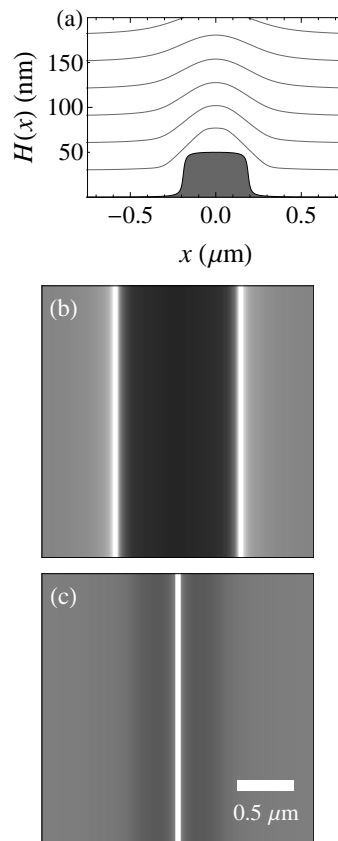


FIG. 4. (a) Equipotential surfaces above a raised ridge (dark region) on a CAM substrate with height profile  $H(x)$  and potential  $-20000.4$  V. The potential difference between each surface is  $0.3$  V. (b) Simulated MEM image an infinitely long raised line at negative defocus, demonstrating that two line caustics can be formed. (c) Simulated MEM image of the same raised line at positive defocus, demonstrating that the same surface feature can produce a single line caustic.

### III. CAUSTIC MIRRORS IN ECL

The use of a CAM in place of a conventional mask in ECL has a number of advantages. All surfaces are potentially CAM candidates and specific mirrors can be tailored by con-

ventional lithography techniques such as top-down direct write EBL techniques.<sup>4-6,24-26</sup> It may also be feasible to utilize self-assembled nanostructures on surfaces, such as quantum dots, as the basis of CAMs for niche applications. Caustics are commonly produced when focusing an optical beam, and they are typically stable to perturbations<sup>19</sup> such as imperfections on the mirror surface, and aberrations in the optical system including an electron energy spread.<sup>3,8,12</sup> Thus a variety of caustics should be readily formed from a vast range of mirror surfaces, including curved lines and junctions, with contributions from both surface topography and potential variations, such as differences in material work function. Caustic features can typically be focused to finer dimensions than the surface structures or variations producing them, improving resolution of lithographic patterns. For example, bright spots of diameter 100 nm are shown in Fig. 2(b) and were produced from microholes of diameter 600 nm, and a raised line of width 400 nm produced a simulated line caustic of width less than 100 nm. Caustic features are by definition very bright, which increases the electron dose to the desired region of the resist, which in combination with the fine focusing of features increases the contrast between exposed and underexposed regions of the resist.

In REBL, the role of the mask is played by the digital pattern generator (DPG) developed by Petric *et al.*,<sup>12,13</sup> which is a sophisticated array of electrostatic mirrors that create the pixels of the image projected onto the resist. As a logical extension, the flexibility of ECL could be improved by adopting a DPG with every individually controllable pixel ‘on,’ i.e. reflecting every electron with a variable but consistently negative potential, creating a flexible CAM. While this decreases the ease of use compared to a static CAM, with no ‘off’ pixels of the CAM DPG, few electrons would be absorbed, increasing electron current and efficiency. By further controlling the electron optics i.e. the defocus of the projected image, a single pattern in the CAM DPG could produce a range of caustic features, such as the examples in Figs. 2 and 4.

Finally we consider throughput, which is a major consideration confronting EBL. As mentioned earlier, the throughput of serial scanning techniques is inherently limited. Simply increasing beam current to increase throughput creates the issue of space-charge effects which tend to blur image features.<sup>6,8,9</sup> However, ECL is a parallel illumination method which can simultaneously illuminate large areas of the resist, ameliorating the requirements

for large beam currents.<sup>8,10</sup> In addition, dual beam LEEM methods have been shown to reduce the effect of the electron beam on the mirror itself, which causes some mirror surfaces to change potential and distort the outgoing electron beam.<sup>10</sup> ECL is entirely compatible with a multiple column architecture which can, in principle, reduce the required beam current in any one column, and realise several tens of wafers per hour.<sup>13</sup> Further improvements are likely in throughput for reflective electron beam lithography systems and ECL will also benefit from such developments.

#### IV. CONCLUSION

In summary, we have outlined a new approach to EBL, ECL, which utilises the reflection of an electron beam from an electrostatic mirror to produce caustics in the demagnified image projected onto the resist. By varying the electron optics both the type and dimensions of the caustic features may be controlled, producing a range of bright tightly focused image features which form the building blocks of a lithographic pattern. The potential exists to apply DPG technology to ECL, providing a more flexible CAM and a complementary mode of REBL.

#### ACKNOWLEDGMENTS

We are grateful to Rod Mackie for technical support. S.M.K., W.X.T., D.M.P. and D.E.J. acknowledge funding from the Australian Research Council via the Discovery–Projects programme. This work was performed in part at the Melbourne Centre for Nanofabrication, an initiative partly funded by the Commonwealth of Australia and the Victorian Government.

---

\*

<sup>1</sup> Y. Xia, J. A. Rogers, K. E. Paul, and G. M. Whitesides, *Chem. Rev.* **99**, 1823 (1999), (doi:10.1021/cr980002q).

<sup>2</sup> A. A. Tseng, K. Chen, C. D. Chen, and K. J. Ma, *IEEE Trans. Electronics Packaging Manufacturing*, **26**, 141 (2003), (doi:10.1109/TEPM.2003.817714).

- <sup>3</sup> D. M. Tennant, in *Nanotechnology*, edited by G. Timp (Springer-Verlag, New York, 1999), pp. 161–205.
- <sup>4</sup> M. D. Fischbein and M. Drndić, *Nano Lett.* **7**, 1329 (2007), (doi:10.1021/nl0703626).
- <sup>5</sup> T. Gnanavel, M. A. Mat Yajid, Z. Saghi, Y. Peng, B. J. Inkson, M. R. J. Gibbs, and G. Möbus, *Appl. Phys. A* **102**, 205 (2011), (doi:10.1007/s00339-010-5953-0).
- <sup>6</sup> J. A. Liddle and G. M. Gallatin, *Nanoscale* **3**, 2679 (2011), (doi:10.1039/c1nr10046g).
- <sup>7</sup> G.-L. Wang, M. Gao, L.-S. Feng, Y. Dun, J.-G. Hou, and J. Tang, *Key Engineering Materials* **483** 243 (2011), (doi:10.4028/www.scientific.net/KEM.483.243).
- <sup>8</sup> H. C. Pfeiffer and W. Stickel, *Microelectron. Eng.* **27**, 143 (1995), (doi:10.1016/0167-9317(94)00075-6).
- <sup>9</sup> L. R. Harriott, in *Proceedings of the Particle Accelerator Conference*, New York, USA, 27 Mar – 02 Apr 1999, edited by A. Luccio and W. MacKay (IEEE, Piscataway, 1999), Vol. 1, pp. 595–599, (doi:10.1109/PAC.1999.795770).
- <sup>10</sup> M. Mankos, D. Adler, L. Veneklasen, and E. Munro, *Surface Science* **601**, 4733 (2007), (doi:10.1016/j.susc.2007.05.062).
- <sup>11</sup> S. D. Berger and J. M. Gibson, *Appl. Phys. Lett.* **57**, 153 (1990), (doi:10.1063/1.103969).
- <sup>12</sup> P. Petric, C. Bevis, A. Carroll, H. Percy, M. Zywno, K. Standiford, A. Brodie, N. Bareket, and L. Grella, *J. Vac. Sci. Technol. B* **27**, 161 (2009), (doi:10.1116/1.3054281).
- <sup>13</sup> P. Petric, C. Bevis, M. McCord, A. Carroll, A. Brodie, U. Ummethala, L. Grella, A. Cheung, and R. Freed, *J. Vac. Sci. Technol. B* **28**, C6 (2010), (doi:10.1116/1.3511436).
- <sup>14</sup> S. Eder-Kapl, E. Haugeneder, H. Langfischer, K. Reimer, J. Eichholz, M. Witt, H.-J. Doering, J. Heinitz, and C. Brandstaetter, *Microelectron. Eng.* **83**, 968 (2006), (doi:10.1016/j.mee.2006.01.246).
- <sup>15</sup> M. J. Wieland, G. de Boer, G. F. ten Berge, M. van Kervinck, R. Jager, J. J. M. Peijster, E. Slot, S. W. H. K. Steenbrink, T. F. Teepen, B. J. Kampherbeek, *Proc SPIE* **7637**, 7637-0F (2010), (doi:10.1117/12.849480).
- <sup>16</sup> M. Altman, *J. Phys: Condens. Matter* **22**, 084017 (2010), (doi:10.1088/0953-8984/22/8/084017).
- <sup>17</sup> D. E. Jesson and W. X. Tang, in *Microscopy: Science, Technology, Applications and Education*, edited by A. Méndez-Vilas and J. Díaz, (Formatex Research Center, Badajoz, 2010), Vol. 3, pp. 1608–1619.

- <sup>18</sup> W. X. Tang, C. X. Zheng, Z. Y. Zhou, D. E. Jesson and J. Tersoff, *IBM J. Res. & Dev.* **55**, 10:1 (2011), (doi:10.1147/JRD.2011.2158762).
- <sup>19</sup> M. V. Berry, in *Physics of Defects, Les Houches Lecture Series Session XXXV* edited by R. Balian, M. Kléman and J.-P. Poirier (North-Holland, Amsterdam, 1981) p. 453.
- <sup>20</sup> H.-C. Kan and R. J. Phaneuf, *J. Vac. Sci. Technol. B* **19**, 1158 (2001), (doi:10.1116/1.1385688).
- <sup>21</sup> S. M. Kennedy, C. X. Zheng, W. X. Tang, D. M. Paganin, and D. E. Jesson, *Ultramicroscopy* **111**, 356 (2011), (doi:10.1016/j.ultramic.2011.01.019).
- <sup>22</sup> S. M. Kennedy, D. M. Paganin, and D. E. Jesson, *IBM J. Res. & Dev.* **55**, 3:1 (2011), (doi:10.1147/JRD.2011.2143310).
- <sup>23</sup> S. M. Kennedy, M. Hjort, B. Mandl, E. Marsell, A. A. Zakharov, A. Mikkelsen, D. M. Paganin, and D. E. Jesson, *Nanotechnology* **23**, 125703 (2012), (doi:10.1088/0957-4484/23/12/125703).
- <sup>24</sup> Y. Huang, X. Duan, Q. Wei, and C. M. Lieber, *Science* **291**, 630 (2001), (doi:10.1126/science.291.5504.630).
- <sup>25</sup> Z. Saghi, T. Gnanavel, Y. Peng, B. J. Inkson, A. G. Cullis, M. R. Gibbs, and G. Möbus, *Appl. Phys. Lett.* **93**, 153102 (2008), (doi:10.1063/1.2998360).
- <sup>26</sup> K. Sun, L. M. Wang, and R. C. Ewing, *Nucl. Instrum. & Methods in Phys. Research B* **266**, 3133 (2008), (doi:10.1016/j.nimb.2008.03.173).



---

## Congruent evaporation temperature of GaAs(001) controlled by As flux

This chapter is an author generated post print of the article

Z. Y. Zhou, C. X. Zheng, W. X. Tang, D. E. Jesson and J. Tersoff, *Congruent evaporation temperature of GaAs(001) controlled by As flux*, Appl. Phys. Lett., 97 (2010) 121912, available electronically at [http://apl.aip.org/resource/1/applab/v97/i12/p121912\\_s1](http://apl.aip.org/resource/1/applab/v97/i12/p121912_s1).

## Declaration for Thesis Chapter "Congruent evaporation temperature of GaAs(001) controlled by As flux"

Declaration by candidate  
For this chapter, the nature and extent of my contribution to the work was the following:

Nature of contribution	Extent of contribution(%)
Co-performed the experiments, co-wrote the paper.	25

The following co-authors contributed to the work. Co-authors who are students at Monash University must also indicate the extent of their contribution in percentage terms

Name	Extent of contribution(%)	Nature of contribution
Zhenyu Zhou	60	Designed the experiments, co-performed the experiments, co-developed the model used in the paper, co-wrote the paper.
Wen-XinTang		Helped perform the experiments and provided technical expertise.
David Jesson		Co-wrote the paper, helped developed the model and provided technical expertise.
Jerry Tersoff		Co-wrote the paper, helped developed the model.

Candidate's signature  Date 24-08-12

**Declaration by co-author**

The undersigned hereby certify that:

- (1) they meet the criteria for authorship in that they have participated in the conception, execution, or interpretation, of at least that part of the publication in their field of expertise;
- (2) they take public responsibility for their part of the publication, except for the responsible author who accepts overall responsibility for the publication;
- (3) there are no other authors of the publication according to these criteria;
- (4) potential conflicts of interest have been disclosed to (a) granting bodies, (b) the editor or publisher of journals or other publications, and (c) the head of the responsible academic unit; and
- (5) the original data are stored at the following location(s) and will be held for at least five years from the date indicated below:

Location(s) School of Physics, Monash University, Clayton

Signature 1	<span style="border: 1px solid black; display: inline-block; width: 100%; height: 15px; background-color: black;"></span>	Date <span style="border: 1px solid black; display: inline-block; width: 80%; height: 15px; vertical-align: middle; text-align: center;">24-08-2012</span>
Signature 2	<span style="border: 1px solid black; display: inline-block; width: 100%; height: 15px; background-color: black;"></span>	<span style="border: 1px solid black; display: inline-block; width: 80%; height: 15px; vertical-align: middle; text-align: center;">21-08-12</span>
Signature 3	<span style="border: 1px solid black; display: inline-block; width: 100%; height: 15px; background-color: black;"></span>	<span style="border: 1px solid black; display: inline-block; width: 80%; height: 15px; vertical-align: middle; text-align: center;">21-08-12</span>
Signature 4	<span style="border: 1px solid black; display: inline-block; width: 100%; height: 15px; background-color: black;"></span>	<span style="border: 1px solid black; display: inline-block; width: 80%; height: 15px; vertical-align: middle; text-align: center;">1-08-12</span>

## Congruent Evaporation Temperature of GaAs(001) Controlled by As Flux

Z. Y. Zhou, C. X. Zheng, W. X. Tang, D. E. Jesson<sup>a)</sup>

*School of Physics, Monash University, Victoria 3800,  
Australia*

J. Tersoff

*IBM Research Division, Thomas J. Watson Research Center,  
Yorktown, Heights, New York 10598, USA*

The congruent evaporation temperature  $T_c$  is a fundamental surface characteristic of GaAs and similar compounds. Above  $T_c$  the rate of As evaporation exceeds that of Ga during Langmuir (free) evaporation into a vacuum. However, during molecular beam epitaxy (MBE) there is generally an external As flux  $F$  incident on the surface. Here we show that this flux directly controls  $T_c$ . We introduce a sensitive approach to measure  $T_c$  based on Ga droplet stability, and determine the dependence of  $T_c$  on  $F$ . This dependence is explained by a simple model for evaporation in the presence of external flux. The capability of manipulating  $T_c$  via changing  $F$  offers a means of controlling congruent evaporation with relevance to MBE, surface preparation methods and droplet epitaxy.

---

<sup>a)</sup> 

Langmuir evaporation of GaAs (001), in which the surface freely evaporates into a vacuum, has been widely studied over the years.<sup>1-4</sup> Central to understanding the physics of Langmuir evaporation is the so-called congruent evaporation temperature  $T_c$ . Below  $T_c$ , Ga and As fluxes leaving the surface are equal which preserves compound stoichiometry. However, above  $T_c$ , As preferentially evaporates from the surface leaving behind Ga-rich liquid droplets.<sup>5,6</sup> In addition to being a major characteristic of III-V surfaces,<sup>7</sup>  $T_c$  is technologically important in defining the upper-bound in temperature for MBE growth<sup>4</sup> and surface cleaning.<sup>8</sup> Recently, it has also been shown that  $T_c$  plays a central role in the physics of Ga droplet dynamics on GaAs (001) (Refs. 9 and 10) which has implications for extending the droplet epitaxy technique.<sup>11</sup> It is therefore important to understand how  $T_c$  depends on experimental conditions.

In this paper we demonstrate that one can directly control  $T_c$  by varying As deposition flux. A sensitive approach is presented for the measurement of  $T_c$  based on the stability of Ga droplets. Our results are explained using a simple model for evaporation in the presence of external As flux. The ability to control  $T_c$  via an applied As flux provides a means of investigating the evaporation and decomposition of III-V materials, as well as elucidating the effect of As flux during surface preparation and MBE growth.

The measurement of  $T_c$  in the presence of external As flux presents a significant experimental challenge. Previous studies have measured  $T_c$  in the absence of flux using careful modulated beam measurements and evaporated species identification.<sup>1</sup> However, there is a barrier to the initial nucleation of Ga droplets. This could lead to hysteresis effects, which would explain the large scatter in earlier measurements of  $T_c$ .<sup>1,3</sup> To avoid this, we focus on the stability of droplets that are already present, finding the temperature where they neither shrink nor grow. In this way we can determine  $T_c$  in the presence of an incident As flux  $F$ , as long as the As

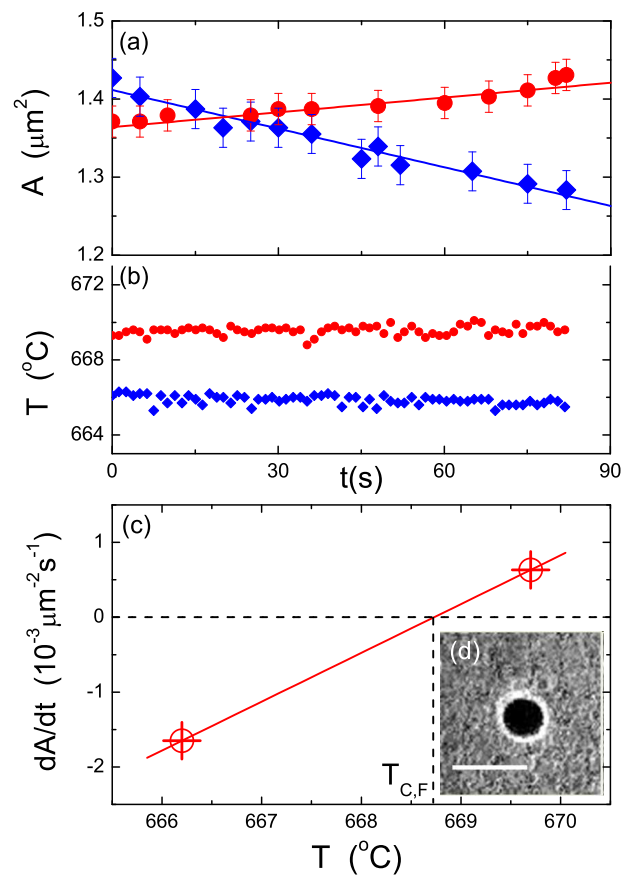


FIG. 1. (Color online)(a) Droplet area  $A$  as a function of time  $t$ . The area is defined as the dark region enclosed within the bright concentric ring in (d). Circles/diamonds in (a) correspond to the respective temperature variation indicated by the circles/diamonds in (b). Temperatures are measured to an accuracy of  $\pm 0.2^\circ\text{C}$ . (c)  $dA/dt$  as a function of temperature  $T$  obtained from the gradients of two lines in (a).  $T_{C,F}$  for the droplets is estimated to occur at the intersection of the straight-line connecting the points with  $dA/dt = 0$ . (d) MEM image of a Ga droplet with the area  $A$  defined as the dark region within the bright concentric ring (scale bar,  $1\mu\text{m}$ ). For this series of measurements  $P_{As} = 4.6 \times 10^{-6}$  Torr.

pressure is not so high as to prevent electron imaging of the droplets.

To create Ga droplets we degassed an undoped GaAs (001)  $\pm 0.1^\circ$  epi-ready wafer at 300 °C under ultra high vacuum for 24 h in an Elmitec low energy electron microscope (LEEM) III system. This was followed by high temperature flashing up to 600 °C and annealing at 580 °C for 2 hours to remove the surface oxide. Well-separated Ga droplets ( $\sim 5\mu\text{m}$ ) were prepared by annealing at 650 °C and were imaged using mirror electron microscopy (MEM),<sup>12-14</sup> in which droplets appear as dark circles surrounded by a bright concentric ring (Fig. 1(d)).<sup>9,14</sup> The droplets were brought into a stable condition by adjusting the temperature so that they neither shrink nor grow. This is the congruent evaporation temperature for zero flux,  $T_{c,0}$ , to which we assign the literature value<sup>4</sup> of 625 °C. All temperatures were measured relative to this value and remained stable to within  $\pm 1^\circ\text{C}$ .

On opening the As shutter, there are transient effects due to changes in surface work function. This occurred over a period of 30 s and care was taken to allow the imaging and As deposition conditions to stabilise before droplet stability measurements commenced. The beam equivalent pressure (BEP) of the  $\text{As}_4$  molecular beam  $P_{\text{As}}$  was determined from the calibrated valve position of the cracker source. Following image stabilisation, we use pattern recognition software to measure and record the droplet area  $A$  as a function of time. The temperature was adjusted to slow the rate of change of droplet size below  $\sim 2 \times 10^{-3} \mu\text{ms}^{-1}$ . The area  $A$  is defined as the dark region enclosed within the bright concentric ring as shown in Fig. 1(d). Note that the droplets appear larger in MEM than their real size,<sup>9,12</sup> but as we are only concerned with nulling the rate of change of droplet size, this does not influence our measurements.

Having obtained a condition where a droplet shrinks (or grows) with a rate  $\leq 2 \times 10^{-3} \mu\text{ms}^{-1}$  the temperature was recorded and then slightly increased (decreased) to produce the opposite behaviour, growth (shrinkage).

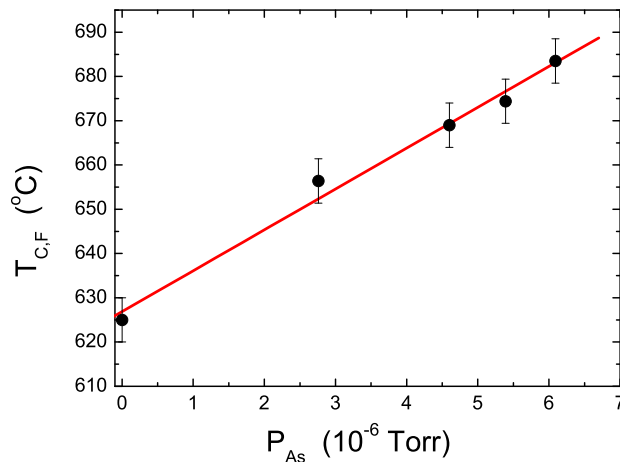


FIG. 2. (Color online) Congruent evaporation temperature  $T_{c,F}$  as a function of  $As_4$  BEP,  $P_{As}$ .

Such a pair of readings is displayed in Fig. 1(a) and (b) for  $P_{As} = 4.6 \times 10^{-6}$  Torr and yields two values of  $dA/dt$  of opposite sign which are plotted against  $T$  in Fig. 1(c). Note that all droplets were observed to shrink (or grow) simultaneously within the field of view ( $50 \mu\text{m}$ ). The method is very sensitive and allows the stability condition to be determined to within a few degrees centigrade. As shown in Fig. 1(c),  $T_{c,F}$  is determined within this narrow temperature range as the intersection point between a straight line connecting the data points and  $dA/dt = 0$ . This procedure was repeated for different values of  $P_{As}$  and the resulting plot of  $T_{c,F}$  versus  $P_{As}$  is shown in Fig. 2. Error bars were estimated as the temperature range spanning the pair of  $dA/dt$  measurements for each value of  $T_{c,F}$  (see, for example, Fig. 1(c)).

Figure 2 shows that  $T_{c,F}$  increases linearly with As flux. We explain this using a standard transition rate model for Ga and As evaporation. Consider a GaAs (001) surface at temperature  $T$  with zero external As

flux. We assume that the surface is in equilibrium with the crystal so that

$$\mu_{Ga} + \mu_{As} = \mu_{GaAs}, \quad (1)$$

where  $\mu_{Ga}$  and  $\mu_{As}$  are the respective Ga and As surface chemical potentials and  $\mu_{GaAs}$  is the chemical potential of the bulk crystal. During congruent evaporation,  $\mu_{Ga}$  attains a steady-state value such that Ga and As evaporate at equal rates. As  $T$  increases,  $\mu_{Ga}$  will increase (thereby equalizing the evaporation rates) until it reaches the liquidus value  $\mu_{Ga,0}$  which defines the upper limit  $T = T_c$  for congruent evaporation. Above  $T_c$ ,  $\mu_{Ga} > \mu_{Ga,0}$  so excess Ga can collect as droplets. These are assumed to remain close to equilibrium with the GaAs substrate at the liquidus composition. The Ga droplets act as sinks for Ga adatoms, which restricts the increase in  $\mu_{Ga}$ . Therefore for  $T > T_c$  As evaporates more rapidly than Ga, and Ga droplets can grow.<sup>4</sup> Below  $T_c$ ,  $\mu_{Ga} < \mu_{Ga,0}$ , so a Ga droplet will lose Ga to the surrounding surface and eventually disappear. At  $T_c$ ,  $\mu_{Ga} = \mu_{Ga,0}$  and the droplet is stable, it neither shrinks nor grows. This stability condition can therefore be used as a sensitive test for measuring  $T_c$ .

Now consider the GaAs crystal under external As flux  $F$ , which changes the steady-state value of  $\mu_{Ga}$  during congruent evaporation. Consequently, the congruent evaporation temperature at which  $\mu_{Ga}$  is at the liquidus value will also change, making  $T_c$  dependent on  $F$ . For clarity, we denote the flux dependent congruent evaporation temperature as  $T_{c,F}$ , and  $T_{c,0}$  is the conventional congruent evaporation temperature in the absence of flux. The bulk liquidus values of the chemical potential are  $\mu_{Ga,F}$  and  $\mu_{Ga,0}$  at  $T_{c,F}$  and  $T_{c,0}$ , respectively. The  $T_{c,F}$  measured by the droplet stability condition thus corresponds to the temperature at which  $\mu_{Ga} = \mu_{Ga,F}$  with the surface under an As flux  $F$ .

The net evaporation rates per unit area are

$$\Phi_{Ga} = r_{Ga} \exp\left(\frac{\mu_{Ga} - E_{Ga}}{kT}\right), \quad (2)$$

$$\Phi_{As} = Nr_{As} \exp\left(\frac{N\mu_{As} - E_{As,N}}{kT}\right) - \alpha F, \quad (3)$$

where  $\alpha$  is the sticking probability of the incident As species and it is assumed that As evaporates as an  $N$ -mer (probably a dimer).  $E_{Ga}$  and  $E_{As,N}$  are the respective transition state energies for Ga adatom and As  $N$ -mer evaporation, with associated rate constants  $r_{Ga}$  and  $r_{As}$  (including the transition state entropy or degeneracy, e.g. number of sites for evaporation per unit area). In Eq. (3),  $\Phi_{As}$  and  $F$  are defined per atom independent of  $N$ , while  $r_{As}$  refers to  $N$ -mer desorption events. For congruent evaporation we have  $\Phi_{Ga} = \Phi_{As}$  and so combining (1) - (3) gives

$$\begin{aligned} Nr_{As} \exp\left(\frac{N\mu_{GaAs} - N\mu_{Ga} - E_{As,N}}{kT}\right) - \alpha F \\ = r_{Ga} \exp\left(\frac{\mu_{Ga} - E_{Ga}}{kT}\right). \end{aligned} \quad (4)$$

$T_{c,F}$  is given by replacing  $\mu_{Ga}$  in Eq. (4) by its liquidus value  $\mu_{Ga,F}$  at  $T_{c,F}$ . Note that the bulk liquidus chemical potential is a basic thermodynamic material property, independent of evaporation. However, it does depend on  $T$ , so from Eq. (4) we obtain an implicit equation for  $T_{c,F}$ . To solve this we expand  $\mu_{Ga,F}$  to first order about  $T_{c,0}$ , the congruent temperature in the absence of flux, giving

$$\mu_{Ga,F} = \mu_{Ga,0} + \mu'_{Ga,0}(T_{c,F} - T_{c,0}). \quad (5)$$

$T_{c,F}$  is then obtained by substituting (5) into (4) for  $\mu_{Ga} = \mu_{Ga,F}$  at  $T = T_{c,F}$ , expanding to first order in  $(T_{c,F} - T_{c,0})$  and rearranging to give

$$T_{c,F} = T_{c,0} + \eta F, \quad (6)$$

where the constant  $\eta$  is given by

$$\begin{aligned} \eta^{-1} = \frac{r_{Ga}}{\alpha k T_{c,0}^2} \exp\left(\frac{\mu_{Ga,0} - E_{Ga}}{k T_{c,0}}\right) [E_{As,N} - E_{Ga} \\ + (N + 1)(\mu_{Ga,0} - \mu'_{Ga,0} T_{c,0}) - N\mu_{GaAs}]. \end{aligned} \quad (7)$$

We note  $P_{As} = \beta F/4$  where the factor of 4 arises because of the incident  $As_4$  species and  $\beta = (2\pi mkT_s)^{1/2}$  with  $m$  the molecular mass and  $T_s$  the temperature of the  $As_4$  gas. Eq. (6) predicts a linear dependence of  $T_{c,F}$  on  $P_{As}$ , as long as the As flux is not too large. This is precisely the behaviour observed in Fig. 2. Unfortunately, the slope  $4\eta/\beta$  is a mix of several unknown parameters, so we cannot compare our measurements with the quantitative value. However, the experimental results of Fig. 2 confirm the behaviour predicted by the theory.

Although it is well appreciated that an external As flux compensates for loss of As by evaporation, the control of  $T_{c,F}$  by varying  $F$  offers important complementary insight into this process. In particular, the results of Fig. 2 provide a quantitative basis for systematic interpolation and extrapolation to different growth conditions. This data also allows a quantitative understanding of the As flux required to avoid decomposition of GaAs during oxide desorption at elevated temperatures.<sup>15</sup> Finally, it is known that  $T_c$  controls the motion of Ga droplets on GaAs.<sup>9</sup> Changing  $T_{c,F}$  by varying As flux will therefore allow the manipulation of droplet motion which may have applications in the positioning of quantum structures formed via droplet epitaxy methods.<sup>11</sup>

## ACKNOWLEDGMENTS

We are grateful to Rod Mackie for technical support and Bruce Joyce for helpful discussions. DEJ and WXT acknowledge support from the ARC, Grant No. DP0985290.

**REFERENCES**

- <sup>1</sup>C. T. Foxon, J. A. Harvey, and B. A. Joyce, *J. Phys. Chem. Solids* **34**, 1693 (1973).
- <sup>2</sup>J. R. Arthur, *J. Phys. Chem. Solids* **28**, 2257 (1967).
- <sup>3</sup>B. Goldstein, D. J. Szostak, and V. S. Ban, *Surf. Sci.* **57**, 733 (1976).
- <sup>4</sup>J. Y. Tsao, *Materials Fundamentals of Molecular Beam Epitaxy*(Academic, San Diego 1993) p. 733 (1993).
- <sup>5</sup>M. Zinke-Allmang, L. Feldman, and W. van Saarloos, *Phys. Rev. Lett.* **68**, 2358 (1992).
- <sup>6</sup>T. D. Lowes and M. Zinke-Allmang, *J. Appl. Phys.* **73**, 4937 (1993).
- <sup>7</sup>C. Chatillon and D. Chatain, *J. Cryst. Growth* **151**, 91 (1995).
- <sup>8</sup>N. Isomura, S. Tsukamoto, K. Iizuka, and Y. Arakawa, *J. Cryst. Growth* **301-302**, 26 (2007).
- <sup>9</sup>J. Tersoff, D. E. Jesson, and W. X. Tang, *Science* **324**, 236 (2009).
- <sup>10</sup>J. Tersoff, D. E. Jesson, and W. X. Tang, *Phys. Rev. Lett.* **105**, 035702 (2010).
- <sup>11</sup>See, for example, T. Mano, T. Kuroda, S. Sanguinetti, T. Ochiai, T. Tateno, J. Kim, T. Noda, M. Kawabe, K. Sakoda, G. Kido, and N. Koguchi, *Nano Lett.* **5**, 425 (2005); M. Yamagiwa, T. Mano, T. Kuroda, T. Tateno, K. Sakoda, G. Kido, N. Koguchi, and F. Minami, *Appl. Phys. Lett.* **89**, 113115 (2006); S. Huang, Z. Niu, Z. Fang, H. Ni, Z. Gong, and J. Xia, *Appl. Phys. Lett.* **89**, 031921 (2006); C. Somaschini, S. Bietti, N. Koguchi, and S. Sanguinetti, *Nano Lett.* **9**, 3419 (2009); J. H. Lee, Z. M. Wang, Z. Y. AbuWaar, and G. J. Salamo, *Cryst. Growth & Design* **9**, 715 (2009) .
- <sup>12</sup>S. A. Nepijko, N. N. Sedov, and G. Schönhense, *J. Microsc* **203**, 269 (2001).
- <sup>13</sup>S. M. Kennedy, D. E. Jesson, M. J. Morgan, A. E. Smith, and P. F.

- Barker, Phys. Rev. A **74**, 044701 (2006).
- <sup>14</sup>S. M. Kennedy, C. X. Zheng, W. X. Tang, D. M. Paganin, and D. E. Jesson, Proc. Roy. Soc. A **466**, 2857 (2010).
- <sup>15</sup>T. Van. Buuren, M. K. Weilmeier, I. Athwal, K. M. Colbow, J. A. Mackenzie, T. Tiedje, P. C. Wong, and K. A. R. Mitchell, Appl. Phys. Lett. **59**, 464 (1991).

---

## Asymmetric coalescence of reactively wetting droplets

This chapter is an author generated post print of the article

C. X. Zheng, W. X. Tang and D. E. Jesson, *Asymmetric coalescence of reactively wetting droplets*, Appl. Phys. Lett., 100 (2012) 071903, available electronically at [http://apl.aip.org/resource/1/applab/v100/i7/p071903\\_s1](http://apl.aip.org/resource/1/applab/v100/i7/p071903_s1).

## Declaration for Thesis Chapter “Asymmetric coalescence of reactively wetting droplets”

Declaration by candidate

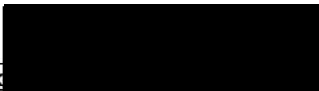
For this chapter, the nature and extent of my contribution to the work was the following:

Nature of contribution	Extent of contribution(%)
Designed and performed the experiments, co-developed the model used in the paper, and co-wrote the paper.	75

The following co-authors contributed to the work. Co-authors who are students at Monash University must also indicate the extent of their contribution in percentage terms

Name	Extent of contribution(%)	Nature of contribution
Wen-XinTang		Provided technical expertise.
David Jesson		Co-wrote the paper, co-developed the model and provided technical expertise.

Candidate's  
signature

	Date <i>24-08-12</i>
---	-------------------------

Declaration by co-authors

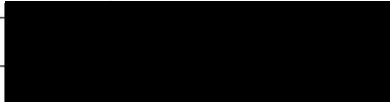
The undersigned hereby certify that:

- (1) they meet the criteria for authorship in that they have participated in the conception, execution, or interpretation, of at least that part of the publication in their field of expertise;
- (2) they take public responsibility for their part of the publication, except for the responsible author who accepts overall responsibility for the publication;
- (3) there are no other authors of the publication according to these criteria;
- (4) potential conflicts of interest have been disclosed to (a) granting bodies, (b) the editor or publisher of journals or other publications, and (c) the head of the responsible academic unit; and
- (5) the original data are stored at the following location(s) and will be held for at least five years from the date indicated below:

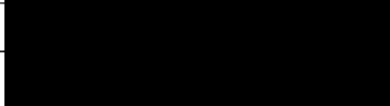
Location(s)

School of Physics, Monash University, Clayton
---

Signature 1

	Date <i>21-08-12</i>
---	-------------------------

Signature 2

	Date <i>21-08-12</i>
---	-------------------------

## Asymmetric Coalescence of Reactively Wetting Droplets

C. X. Zheng, W. X. Tang, and D. E. Jesson<sup>a)</sup>

*School of Physics Monash University, Victoria 3800,  
Australia*

Coalescence of droplets during reactive wetting is investigated for the liquid Ga/GaAs(001) system. *In situ* mirror electron microscopy reveals that coalescence predominantly involves the motion of one reactive droplet relative to the other. This behaviour differs significantly from coalescence in non-reactive systems and is associated with contact line pinning at a ridge/etch pit edge which is identified using atomic force microscopy and selective etching. A simple geometrical model is presented to describe the pinning.

---

a) 

The dynamics of droplet coalescence on surfaces at ambient temperatures is an active area of research.<sup>1-3</sup> Unlike freely suspended droplets, the contact-line at the liquid-solid-gas interface strongly influences the coalescence kinetics of sessile drops. Analysing droplet kinetics is therefore an important means of studying the contact line motion itself. Studies of coalescence have primarily been restricted to non-reactive droplets. However, there is also significant interest in the contact line dynamics of reactive systems<sup>4-8</sup> which are of appreciable technological importance.<sup>9-11</sup> At high temperatures, the spreading of molten metal droplets is accompanied by chemical reactions or interdiffusion at the solid-liquid interface which may deform planar substrates by mass-transport and change the kinetics via ridge formation at the contact-line. Studies of such phenomena have led to important new insights into the kinetics of reactive spreading.<sup>4-11</sup> However, in comparison with liquids at ambient temperatures,<sup>1-3</sup> droplet coalescence in reactive systems is still poorly understood.

Here, we present a study of droplet coalescence in a model reactive system; liquid Ga on GaAs (001). We identify ridge formation at the contact line by selective etching and atomic force microscopy. The dynamics of reactive droplet coalescence is then studied in real-time by mirror electron microscopy (MEM)<sup>12,13</sup> and is found to differ significantly from the behaviour of non-reactive systems, such as low viscosity liquids. A distinctive feature is the motion of one droplet relative to the other. We associate this with enhanced pinning of the contact-line at the ridge/etch pit which subsequently planarises on exposure to vacuum following coalescence.

Ga droplets were formed on undoped, 'epi-ready' grade GaAs (001) wafers with an actual orientational accuracy of  $\pm 0.1^\circ$ . Wafers were out-gassed at 300 °C under ultra-high-vacuum conditions for 24 hours in an Elmitec low energy electron microscope (LEEM) III system. The sample was then flashed up to 600 °C, followed by annealing at 580 °C for 2

hours, to remove the surface oxide. Ga droplets were created by annealing above the planar surface congruent evaporation temperature at 670 °C and were imaged using mirror electron microscopy (MEM).<sup>13-16</sup> Droplet motion was observed<sup>14,15</sup> and movies of coalescence events were recorded. The sample was then quenched to room temperature and droplets were imaged *ex situ* by atomic force microscopy (AFM) in non-contact mode. To characterise the morphology of the liquid-solid interface, the Ga droplets were selectively etched away using 10 mol/L NaOH solution at 50 °C which preserved the GaAs surface. The sample was then reimaged by AFM.

At temperatures of 670 °C, Ga droplets readily etch GaAs<sup>17-19</sup> and also move across the surface driven by a disequilibrium between the droplet and the surface during Langmuir evaporation.<sup>14,15</sup> Fig. 1(a) contains an AFM image of a droplet which has moved across the slightly rough epi-ready surface leaving behind a smooth trail. A line trace of the droplet and trail is contained in panel (b). Panel (c) contains an AFM image of the etch pit geometry underneath a droplet following selective etching of Ga. The line trace shown in panel (d) clearly identifies a ridge (arrowed) which forms a rim around the etch pit. This appears similar in form to the ridge observed by Somaschini *et al.* in droplet epitaxy.<sup>20</sup>

Fig. 2(a) displays an AFM image of droplet A that has undergone a coalescence event with a second droplet which had previously occupied the adjacent etch pit B. A line trace across etch pit B and trail as indicated by the white line is contained in (b). Here, there is an absence of a ridge at the edge of the etch pit (cf. panel 1(d)). An AFM image of a post-coalescence geometry similar to panel 2(a) is shown in panel 2(c) following selective etching of the surface Ga. The line trace corresponding to the horizontal white line is shown in panel (d). Etch pit C clearly contains a ridge similar to that observed in panel 1(d). We can therefore deduce that, since ridges are associated with the etch pits of isolated droplets (Fig. 1(d)) and are

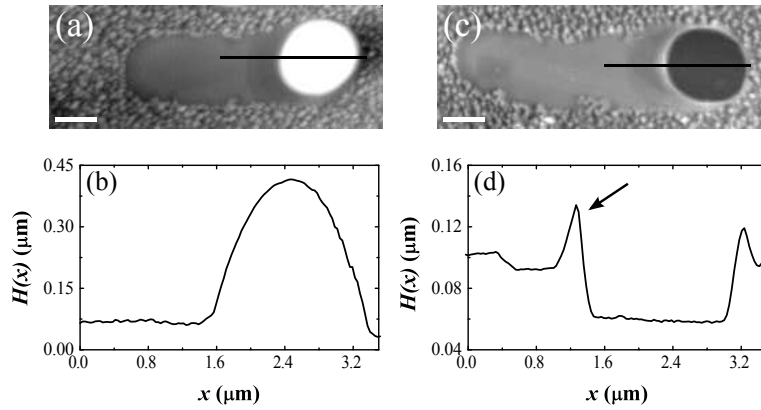


FIG. 1. AFM images of Ga-rich liquid droplets on GaAs (001). (a) A droplet has left behind a smooth trail on the slightly rough epi-ready wafer surface. A line trace corresponding to the line shown is given in (b). (c) AFM image following selective etching of Ga revealing the etch pit geometry beneath a droplet. The line trace corresponding to the horizontal dark line is contained in (d). A ridge (arrowed) forms a rim around the etch pit. Scale markers in (a) and (c) are  $1 \mu\text{m}$  across.

absent from etch pits exposed by droplets which have been displaced by coalescence events (Fig. 2(b)), the droplet which previously occupied etch pit D in Fig. 2(c) was absorbed into a droplet occupying etch pit C by coalescence.

The absence of ridges at the edges of etch pits exposed by coalescence events suggests two possibilities. First, it is possible that the ridge is dragged by the contact line of the coalescing droplet such that it is erased from the surface. Alternatively, if the droplet coalescence is fast on the time scale of ridge formation/dissolution, the ridge may be left exposed to vacuum and subsequently planarise. To further investigate this issue we turn to MEM which is capable of studying coalescence events of reactive droplets in real-time at elevated temperatures. Images taken from a MEM movie of Ga droplet coalescence at  $670 \text{ }^\circ\text{C}$  are contained in Fig. 3. The

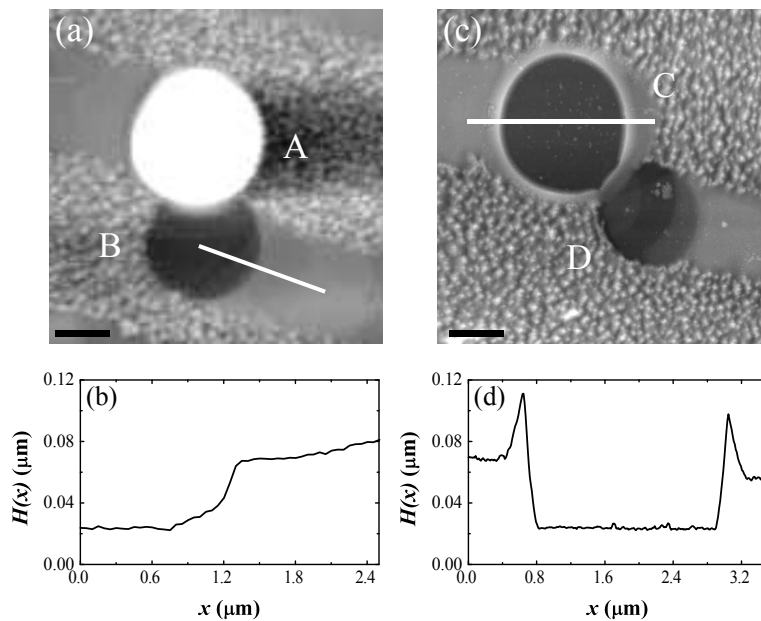


FIG. 2. AFM images of Ga-rich liquid droplet coalescence events on GaAs (001). (a) A droplet previously occupying etch pit B has coalesced with droplet A. (b) Height profile of etch pit B corresponding to the line shown in panel (a). No ridge is present at the edge of the etch pit exposed by coalescence. (c) AFM image of a coalescence event of geometry similar to panel (a) following selective etching of Ga. A line trace of etch pit B is contained in (d) for the line shown in panel (c). Scale markers in (a) and (c) are  $1 \mu\text{m}$  across.

droplets appear as uniform dark discs somewhat larger than the actual droplet, surrounded by a concentric bright halo.<sup>14,15</sup> In panel (a), droplet 1 translates across the substrate and coalesces with droplet 2. The coalescence event is rapid, occurring in less than a movie frame (0.1 s) giving a minimum contact line velocity of  $18 \mu\text{m s}^{-1}$ . It is also highly asymmetric in nature involving the slippage and motion of droplet 1 relative to droplet 2. This exposes the etch pit associated with droplet 1 in panel (b).

To explain the observed coalescence dynamics in reactive systems it is instructive to first consider the coalescence of non-reactive droplets as

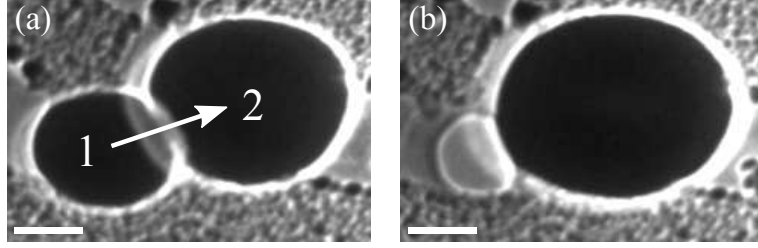


FIG. 3. Images taken from a MEM movie of Ga droplet coalescence at 670 °C. (a) Droplet 1 translates across the surface and coalesces with droplet 2. This occurs in less than 0.1 s and exposes the etch pit beneath the droplet as shown in (b). The coalescence occurs by the motion of droplet 1 relative to droplet 2. Scale markers in (a) and (b) are 1.5  $\mu\text{m}$  across.

schematically depicted in Fig. 4(a). Here the droplets are coalescing via a neck region and in Fig. 4(b) we consider the forces acting at contact line position A. The equilibrium angle of contact  $\theta = \theta_0$  for an isolated droplet is usually related to surface tensions via Young's equation<sup>21</sup>

$$\gamma_{vs} - \gamma_{ls} = \gamma_{vl} \cos \theta_0, \quad (1)$$

where  $\gamma_{vs}$ ,  $\gamma_{ls}$  and  $\gamma_{vl}$  are the respective tensions of the vapour-solid, liquid-solid and vapour-liquid interfaces. This can be simply derived by assuming force equilibrium at the contact line in a direction parallel to the substrate. However, during coalescence the neck region (Fig. 4(a)) will result in a reduction in  $\theta$  such that  $\theta < \theta_0$ . This will unbalance the surface tensions creating a net force on the contact line which will move it to the right (ignoring any pinning due to surface roughness). It is therefore usual to observe both droplets moving during coalescence in non-reactive systems.<sup>1-3</sup>

The lateral force balance, at the heart of Young's equation, leaves an unbalanced vertical component so that Eq. (1) inherently assumes the substrate is perfectly rigid and nonreactive. For our reactive liquid Ga/solid

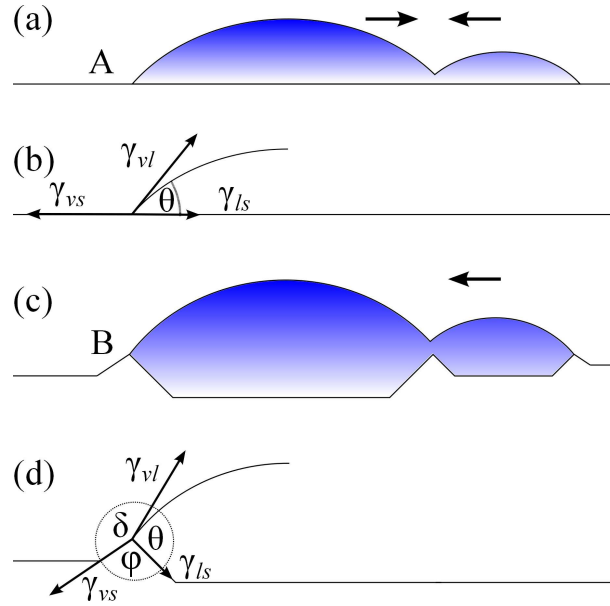


FIG. 4. (a) Schematic representation of droplet coalescence in a non-reactive system. The surface tensions acting at contact line position A are shown in (b). (c) Schematic representation of droplet coalescence in a reactive system. The surface tensions acting at contact line position B are shown in (d).

GaAs system, it is possible to form a ridge at the contact line by mass transport, as shown in Figs. 1(d) and 2(d). This allows the equilibration of the vertical force as shown in Fig. 4(d)<sup>8,22-24</sup> which, for an isolated droplet, gives rise to the relationship

$$\frac{\gamma_{vs}}{\sin\theta_R} = \frac{\gamma_{vl}}{\sin\varphi} = \frac{\gamma_{ls}}{\sin\delta}, \quad (2)$$

as derived from Neumann's triangle of forces. Here,  $\theta = \theta_R$ , which exactly balances the surface tensions. However, Gibbs<sup>25</sup> showed that the contact line remains pinned for a range of contact angles given by the inequality

$$\theta_0 \leq \theta \leq (\pi - \varphi) + \theta_0, \quad (3)$$

which has important implications for coalescence in reactive systems.

In particular, consider the coalescence of two reactive droplets as depicted schematically in Fig. 4 (c). The coalescence events in the MEM movies occur in less than 0.1 sec and so we assume that the ridge geometry is preserved during the process. The surface tensions acting at contact line position B are shown in Fig. 4(d). Following formation of the neck region,  $\theta$  will be reduced away from  $\theta_R$  but, provided  $\theta \geq \theta_0$ , Eq. (3) indicates that the contact line will remain pinned. To unpin the droplet at point B, the applied force per unit length of contact line resulting from a reduction in  $\theta$  needs to be greater than  $f$  where

$$f = \gamma_{vl}(\cos\theta_0 - \cos\theta_R). \quad (4)$$

The magnitude of the total force to overcome the pinning will increase with droplet radius and so large droplets will tend to absorb smaller droplets during coalescence without shifting their centre of mass. This explains the asymmetric nature of the coalescence dynamics in reactive systems.

In summary, we have studied droplet coalescence events in a model reactive wetting system. Ridge formation at the contact line changes the coalescence dynamics so that when two droplets touch they coalesce with the resulting centre of mass located at the projected centre of the larger of the two droplets. Following exposure to vacuum, the ridge planarises due to As evaporation and surface diffusion of Ga.

We thank Jerry Tersoff for helpful discussions and Rod Mackie for technical support. D. E. J and W. X. T. acknowledge support by the Australian Research Council (Grant No. DP0985290).

## REFERENCES

- <sup>1</sup>R. Narhe, D. Beysens, and V. S. Nikolayev, *Langmuir* **20**, 1213 (2004).

- <sup>2</sup>M. Wu, T. Cubaud, and C.-M. Ho, *Phys. Fluids* **16**, L51 (2004).
- <sup>3</sup>W. D. Ristenpart, P. M. McCalla, R. V. Roy, and H. A. Stone, *Phys. Rev. Lett.* **97**, 064501 (2006).
- <sup>4</sup>D. Chatain and W. C. Carter, *Nat. Mater.* **3**, 843 (2004).
- <sup>5</sup>E. Saiz and A. P. Tomsia, *Nat. Mater.* **3**, 903 (2004).
- <sup>6</sup>J. A. Warren, W. J. Boettinger, and A. R. Roosen, *Acta Mater.* **46**, 3247 (1998).
- <sup>7</sup>N. Eustathopoulos, *Acta Mater.* **46**, 2319 (1998).
- <sup>8</sup>E. Saiz, R. M. Cannon, and A. P. Tomsia, *Acta Mater.* **48**, 4449 (2000).
- <sup>9</sup>R. J. Braun, B. T. Murray, W. J. Boettinger, and G. B. McFadden, *Phys. Fluids* **7**, 1797 (1995).
- <sup>10</sup>J. C. Ambrose, M. G. Nicholas, and A. M. Stoneham, *Acta Metal. Mater.* **40**, 2483 (1992).
- <sup>11</sup>J. C. Ambrose, M. G. Nicholas, and A. M. Stoneham, *Acta Metal. Mater.* **41**, 2395 (1993).
- <sup>12</sup>S. A. Nepijko, N. N. Sedov, and G. Schönhense, *J. Microsc.* **203**, 269 (2001).
- <sup>13</sup>S. M. Kennedy, C. X. Zheng, W. X. Tang, D. M. Paganin, and D. E. Jesson, *Ultramicroscopy* **111**, 356 (2011).
- <sup>14</sup>J. Tersoff, D. E. Jesson, and W. X. Tang, *Science* **324**, 236 (2009).
- <sup>15</sup>W. X. Tang, C. X. Zheng, Z. Y. Zhou, D. E. Jesson, and J. Tersoff, *IBM J. Res. Dev.* **55**, 395 (2011).
- <sup>16</sup>J. Tersoff, D. E. Jesson, and W. X. Tang, *Phys. Rev. Lett.* **105**, 035702 (2010).
- <sup>17</sup>C. Chatillon and D. Chatain, *J. Cryst. Growth* **151**, 91 (1995).
- <sup>18</sup>M. Zinke-Allmang, L. C. Feldman, and W. van Saarloos, *Phys. Rev. Lett.* **68**, 2358 (1992).
- <sup>19</sup>T. D. Lowes and M. Zinke-Allmang, *J. Appl. Phys.* **73**, 4937 (1993).
- <sup>20</sup>C. Somaschini, S. Bietti, N. Koguchi, and S. Sanguinetti, *Nano Lett.* **9**,

3419 (2009).

- <sup>21</sup>T. Young, *Phil. Trans. Roy. Soc* **95**, 65 (1805).
- <sup>22</sup>G. R. Lester, *J. Colloid Sci.* **16**, 315 (1961).
- <sup>23</sup>Y. Liu and R. German, *Acta Mater.* **44**, 1657 (1996).
- <sup>24</sup>M. E. R. Shanahan and A. Carré, *Langmuir* **11**, 1396 (1995).
- <sup>25</sup>J. W. Gibbs, *The Scientific Papers of J. Willard Gibbs*, Vol. 1 (Dover, New York, 1961).

---

## Relief of surface stress at steps during displacive adsorption of As on Si(111)

This chapter is an author generated post print of the article

C. X. Zheng, W. X. Tang and D. E. Jesson, *Relief of surface stress at steps during displacive adsorption of As on Si(111)*, Appl. Phys. Lett., 100 (2012) 201602, available electronically at [http://apl.aip.org/resource/1/applab/v100/i20/p201602\\_s1](http://apl.aip.org/resource/1/applab/v100/i20/p201602_s1).

## Declaration for Thesis Chapter "Relief of surface stress at steps during displacive adsorption of As on Si(111)"

Declaration by candidate

For this chapter, the nature and extent of my contribution to the work was the following:

Nature of contribution	Extent of contribution(%)
Designed and performed the experiments, co-developed the model used in the paper, co-wrote the paper.	75

The following co-authors contributed to the work. Co-authors who are students at Monash University must also indicate the extent of their contribution in percentage terms

Name	Extent of contribution(%)	Nature of contribution
Wen-XinTang		Provided technical expertise.
David Jesson		Co-wrote the paper, co-developed the model and provided technical expertise.

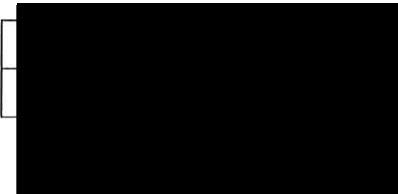
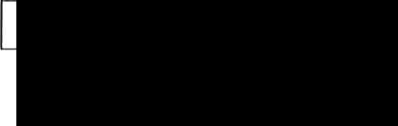
Candidate's signature		Date 24-08-12
-----------------------	---	------------------

**Declaration by co-authors**

The undersigned hereby certify that:

- (1) they meet the criteria for authorship in that they have participated in the conception, execution, or interpretation, of at least that part of the publication in their field of expertise;
- (2) they take public responsibility for their part of the publication, except for the responsible author who accepts overall responsibility for the publication;
- (3) there are no other authors of the publication according to these criteria;
- (4) potential conflicts of interest have been disclosed to (a) granting bodies, (b) the editor or publisher of journals or other publications, and (c) the head of the responsible academic unit; and
- (5) the original data are stored at the following location(s) and will be held for at least five years from the date indicated below:

Location(s)	School of Physics, Monash University, Clayton
-------------	---

Signature 1		Date 21-08-12
Signature 2		21-08-12

## Relief of Surface Stress at Steps during Displacive Adsorption of As on Si(111)

C. X. Zheng, W. X. Tang, and D. E. Jesson<sup>a)</sup>

*School of Physics Monash University, Victoria 3800,  
Australia*

(Dated: 15 August 2012)

The displacive adsorption of As on  $1\times 1$  Si(111) is examined using surface electron microscopy. High temperature adsorption experiments are used to reduce the As chemical potential and identify regions of enhanced As incorporation in the vicinity of steps. This is explained by a reduction in tensile surface stress associated with  $1\times 1$  As:Si(111). Cycling the incident As flux on and off creates surface roughening via respective displacive adsorption and evaporation of As. This roughness facilitates increased  $1\times 1$  As:Si(111) coverage during As deposition due to surface stress relief at steps.

---

a)

It is well known that adsorbates on semiconductor surfaces can radically influence the surface reconstruction and hence its surface stress.<sup>1</sup> Given that surface steps offer potential sites for strain relaxation,<sup>2-5</sup> it would seem natural that they could play an important role in preferential adsorption via the relief of surface stress. However, experimental verification of such behaviour in semiconductor systems is rare. Indeed, an investigation of displacive adsorption of As on Si(001) showed that, contrary to popular belief, surface steps played no role in the observed intermixing.<sup>6</sup>

In this Letter we study the role of surface steps in the adsorption of As on Si(111) which has received considerable attention over the years. From a technological perspective it represents the initial stages of GaAs growth on Si and the resulting As-terminated surface is extremely resistant to surface contamination. This latter property results from the replacement of the outermost Si atoms of the (111) surface by three-fold coordinated As atoms.<sup>7-9</sup> This saturates all surface bonds in the  $1\times 1$  surface. To elucidate the interplay between surface stress and steps we apply surface electron microscopy to study As adsorption on Si(111) in real-time. By studying adsorption at high temperatures, under large As flux, we can identify the relative roles of terraces and steps.  $1\times 1$  As:Si(111) regions form preferentially in the vicinity of steps which we attribute to a reduction in surface stress.

Experiments were performed in an Elmitec LEEM III system adapted for III-V epitaxy.<sup>10</sup> A sulfur doped Si(111) $\pm 1^\circ$  wafer was degassed at 680 °C under ultrahigh vacuum for 24 hours. A clean surface was obtained by heating the surface to 1250 °C for 30 s. To relieve thermal stress, the flashing temperature was approached in several rounds of 50 °C increments. The sample was then cooled to the As adsorption temperature and exposed to As<sub>2</sub> flux from an As cracker source. The beam effective pressure (BEP) of the As<sub>2</sub> molecular beam was determined from the calibrated valve position

of the cracker source.

Images taken from a mirror electron microscopy (MEM)<sup>11? -13</sup> movie of As<sub>2</sub> adsorption at 745 °C are contained in Fig. 1. Panel (a) shows the Si(111) surface consisting of triangular 7×7 domains on 1×1 terraces. After 25 s of exposure to a 3.7 × 10<sup>-6</sup> Torr As<sub>2</sub> molecular beam the break up of the 7×7 domains can be observed in panel (b) and after 40 s the surface is completely covered in 1×1 As:Si(111) (panel (c)). Zinke-Allmang *et al.*<sup>14</sup> established that As desorption follows a second-order kinetic law with As coverage  $\theta$  decaying with time  $t$  as  $\theta = (1 + \kappa(T)t)^{-1}$  from an initial full ML coverage. The desorption rate constant at temperature  $T$  is given by  $\kappa(T) = \kappa_0 \exp(-Q_D/kT)$  with  $\kappa_0 = 10^{18} \text{ ML}^{-1}\text{s}^{-1}$  and  $Q_D = 4.3 \text{ eV}$ . A plot of  $\theta$  is contained in panel (d) for various temperatures showing that As desorption from the surface is negligible at 745 °C. The incident As appears to be incorporated uniformly across the Si surface and there is no direct evidence that steps play a preferential role compared with the terrace.

In order to develop an experimental method to isolate the role of surface steps, we consider a simple model for a Si surface under As flux  $F$ . We assume the system is in equilibrium so that the incident As flux compensates for the flux lost by surface evaporation. We then have

$$\alpha F = N r_{As} \exp\left(\frac{N\mu_{As} - E_{As,N}}{kT}\right), \quad (1)$$

where  $\alpha$  is the sticking probability of the incident As species and As evaporates as an N-mer, most likely a dimer.  $E_{As,N}$  is the transition state energy for As N-mer evaporation, with associated rate constant  $r_{As}$  including the transition state entropy or degeneracy, e.g. number of sites for evaporation per unit area.  $F$  is defined per atom independent of  $N$ , while  $r_{As}$  refers to N-mer desorption events. Rearranging (1) then gives

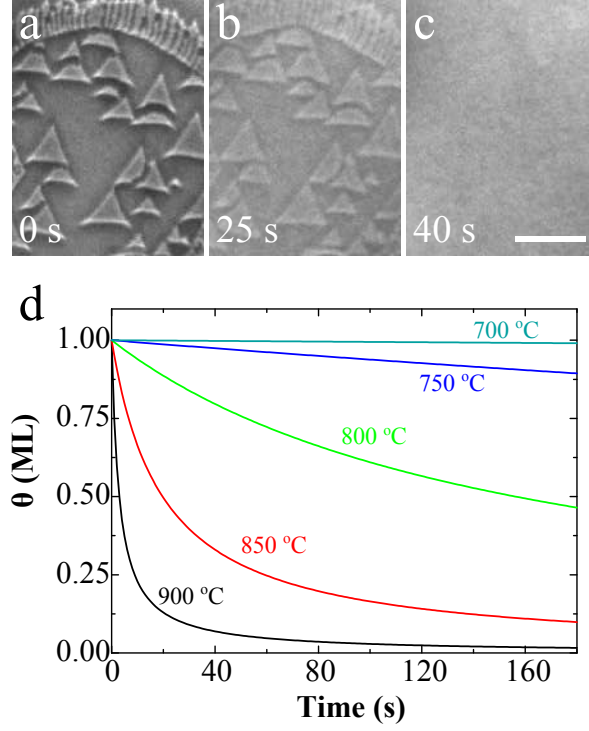


FIG. 1. MEM images of As adsorption (BEP:  $3.7 \times 10^{-6}$  Torr) on Si(111) at 745 °C. (a) Triangular  $7 \times 7$  domains on  $1 \times 1$  terraces. (b) Break up of  $7 \times 7$  domains after 25 s exposure to As flux. (c) Eventually the whole surface is covered by a ML of As and the image contrast is lost. (d) As coverage  $\theta$  as a function of time for various temperatures during desorption. The scale marker in (c) is 2  $\mu\text{m}$  across.

$$N\mu_{As} = E_{As,N} + kT \ln(\alpha F / Nr_{As}). \quad (2)$$

Since the argument of the logarithm is less than unity,  $\mu_{As}$  decreases with temperature  $T$  but increases with  $F$ .

The surface As at chemical potential  $\mu_{As}$  acts as a reservoir for establishing regions of  $1 \times 1$  As:Si(111) surface. However, it is well appreciated that the  $1 \times 1$  As:Si(111) surface is under strong tensile stress.<sup>1</sup> The structure of  $1 \times 1$  Si(111) is unknown but it is thought that a disordered array

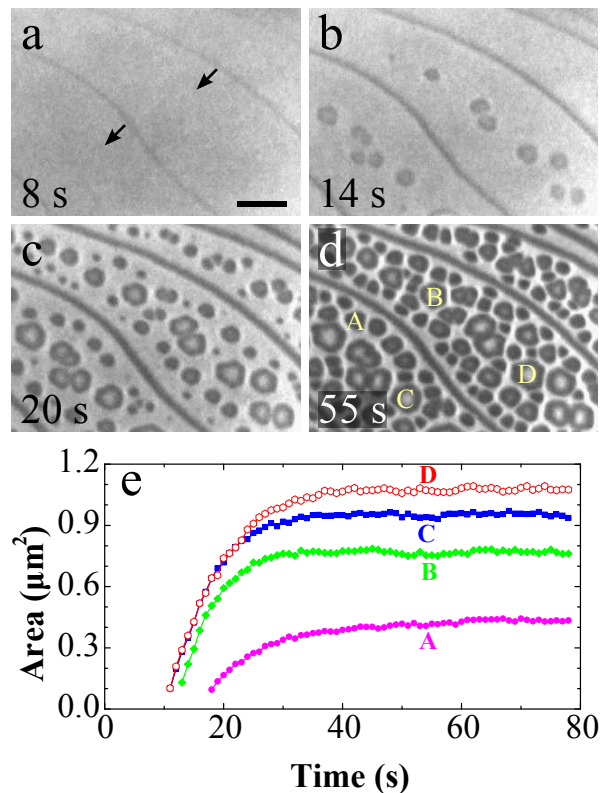


FIG. 2. MEM images of As adsorption on Si(111) at 890 °C. (a)  $1 \times 1$  surface showing dark bands at the positions of surface steps after 8 s of As exposure. Arrows indicate the direction of step movement caused by Si adatom incorporation. (b) Nucleation of 2D Si islands at the centre of terraces. (c) Further nucleation of 2D Si islands after longer As exposure. (d) Saturation of As adsorption on the surface resulting in a stabilised array of 2D islands. (e) Area of several islands denoted in (d) as a function of time. The scale marker in (a) is  $2 \mu\text{m}$  across.

of adatoms is a reasonable approximation.<sup>15,16</sup> Since  $2 \times 2$  and  $\sqrt{3} \times \sqrt{3}$  adatom covered Si give rise to mild tensile surface stress,<sup>1</sup> it is likely that  $1 \times 1$  Si(111) is also associated with tensile surface stress. With increasing coverage, the stress component of the surface free energy will therefore increase and so for a given  $\mu_{As}$  there will be a finite equilibrium coverage

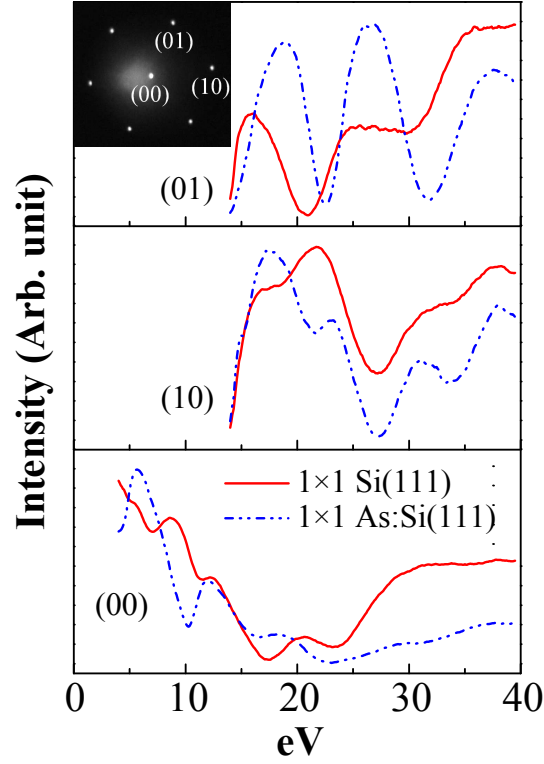


FIG. 3.  $\mu$ LEED I-V curves of (00), (01) and (10) spots obtained on  $1 \times 1$  Si(111) and  $1 \times 1$  As:Si(111) surfaces. Inset shows the  $\mu$ LEED pattern of  $1 \times 1$  As:Si(111) at 16.9 eV.

of  $1 \times 1$  As:Si(111). At low enough temperatures, where As evaporation is low,  $\mu_{As}$  will be sufficiently high to establish near ML coverage as seen in our experiment at 745 °C (Fig. 1(c)).

At higher  $T$  one would expect lower  $\mu_{As}$  (Eq. (2)) and hence a reduced  $1 \times 1$  As:Si(111) terrace coverage for a given  $As_2$  flux. However, surface stress can be relieved at steps at the cost of elastic deformation<sup>2-5</sup> and it would therefore seem feasible that terrace regions adjacent to steps can provide significant potential for strain relaxation and favourable sites for ordered  $1 \times 1$  As:Si(111). To explore this possibility we therefore performed MEM imaging at an increased temperature of 890 °C where the evaporation

rate of As is significantly higher (panel 1(d)). Fig. 2(a) displays the  $1\times 1$  Si surface following 8 s of exposure to  $\text{As}_2$  flux. First, a dark band appears at the positions of surface steps associated with a change in surface work function. The steps are observed to advance across the surface in the direction of the arrows. After 14 s, 2D islands nucleate on terraces between steps (panel (b)) which grow and are accompanied by further 2D island nucleation (panel (c)) until the morphology saturates in panel (d). Pattern recognition software was used to measure and record the area of several 2D islands in panel (d) as a function of time (panel (e)). LEED patterns of the surface before and after As adsorption displayed a  $1\times 1$  geometry (Fig. 3) but the I-V curves provide a different signature. This is consistent with As atoms replacing the outermost Si atoms of the Si(111) surface which preserves the  $(1\times 1)$  symmetry and is the commonly accepted structural model for  $1\times 1$  As:Si(111).<sup>7-9</sup>

These observations at elevated temperatures and reduced  $\mu_{\text{As}}$  are consistent with terrace regions adjacent to steps acting as preferred sites for strain relaxation<sup>2-5</sup> which stabilises regions of  $1\times 1$  As:Si(111). We note that the attachment of As adatoms to step edges offers the possibility of removing Si dangling bonds and reducing step energy.<sup>3</sup> However, the work function contrast observed as a dark band at step edges in Fig. 2(a) is spatially too extensive to be explained alone by such a microscopic, localised effect. Although we are unable to unambiguously identify the precise location of ordered  $1\times 1$  As:Si(111) regions in relation to the step edge, it is likely that preferred adsorption occurs on the terrace on the top of the step edge where one would intuitively expect strain relaxation to be greater.

In addition to preferential intermixing in the vicinity of step edges, Si atoms are also displaced from the terraces where they migrate to the step edges causing them to flow (Fig. 2(a)). Eventually, the Si adatom supersaturation caused by displacive adsorption of As results in the nucleation

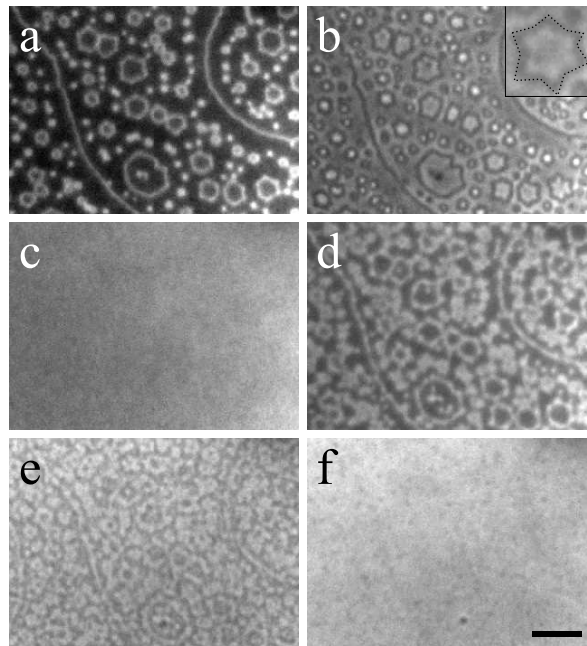


FIG. 4. LEEM images of As adsorption and desorption on  $1 \times 1$  Si(111) at 890 °C. (a) Stabilised surface after 120 s of As exposure. (b) Surface following 60 s of As desorption after turning off the As flux. Inset shows an enlarged star-like island shape caused by desorption. (c) After 170 s of As desorption the image contrast disappears. (d) Readsorption of As on the surface following 180 s of As exposure. (e) Further round of As adsorption following 60 s of As exposure to the surface in (d) after As desorption. (f) Following 260 s of As exposure full As coverage is approached. The scale marker in (f) is  $2 \mu\text{m}$  across. Images were obtained at 5.1 eV.

of Si islands at the centre of terraces, midway between surface steps (Fig. 2(b)). This is consistent with the steps acting as sinks for Si adatoms. Once nucleated, the 2D islands provide new surface steps which are associated with dark regions of well-ordered  $1 \times 1$  As:Si(111) (Fig. 2(b)-(d)) consistent with preferential intermixing.

We note that if small patches of  $1 \times 1$  As:Si(111) form by displacive

adsorption on the terraces then eventually the tensile surface stress will increase as more As is adsorbed. Eventually, the equilibrium concentration will be obtained, explaining the stagnation in growth of the 2D islands observed in panel 2(e). By summing the areas obtained by step advancement and 2D island nucleation using pattern recognition software we estimate a critical As coverage of approximately 0.5 ML for stagnation of displacive adsorption at this temperature. We note that here, intrinsic surface stress associated with the terrace acts to resist intermixing which is opposite to Si(001) in which intrinsic stress favours displacive adsorption.<sup>6</sup>

To further elucidate the role of surface stress in intermixing, regions close to the surface steps were imaged using low energy electron microscopy (LEEM) where the high As content  $1\times 1$  As:Si(111) appeared with bright reflectivity contrast (Fig. 4(a)). The steps associated with the quasi-hexagonal 2D islands are of  $[\bar{1}\bar{1}2]$  and  $[11\bar{2}]$  types.<sup>3</sup> Upon turning off the As<sub>2</sub> flux, the LEEM contrast reverses rapidly as the large transient population of surface As, probably in the form of dimers, evaporates into the vacuum (panel (b)). As can be seen from the inset in panel (b), during evaporation the quasi-hexagonal 2D islands change shape adopting a star-like morphology which may reflect the preference for  $\langle\bar{1}10\rangle$  type steps. The shape change may be associated with a number of factors including the elimination of vacancies within the 2D islands which are left behind by As evaporation from the surface layer. After 170 s the contrast disappears (panel (c)) as the Si(111)  $1\times 1$  surface is restored.

Upon resumption of As deposition the step contrast associated with the 2D islands reappears as As is preferentially incorporated and it can be observed that island coarsening and dissolution into the surrounding step edges is strongly suppressed by the presence of As.<sup>17</sup> The islands grow through attachment of Si atoms displaced from the terraces and after 180 s of As exposure (panel (d)), the island array resembles the arrangement in

panel (a), before the flux is turned off. The steps however appear to have roughened and there is a greater proportion of bright contrast corresponding to larger areas of well-ordered  $1\times 1$  As:Si(111). This is consistent with an increased defect/step density following As evaporation from the surface and a second round of displacive adsorption when the flux is turned on. After a further sequence of evaporation/displacive adsorption the surface has roughened considerably and the  $1\times 1$  As:Si(111) regions have increased in area (panel (e)). Eventually this expands until full As coverage is approached (panel (f)).

Note that in our experiments we are unable to resolve the atomic-scale nature of  $1\times 1$  As:Si(111) intermixing. At less than full ML coverage it is possible that patches of As in terminating  $1\times 1$  positions are surrounded by patches of Si in similar positions. Alternatively, it is conceivable that the intermixing is alloy-like where individual As atoms intermix with Si atoms in the uppermost layer. In either case, the detailed nature of the intermixing does not effect our main conclusions regarding preferential As adsorption in the vicinity of steps.

In summary, by tuning the As chemical potential  $\mu_{As}$  we are able to identify surface steps as preferential sites for displacive adsorption of As on Si(111). We attribute this effect to a relaxation in surface stress on terrace regions adjacent to steps. At lower temperatures where  $\mu_{As}$  is sufficiently large, the effect is masked by displacive adsorption on the terraces.

We thank Rod Mackie for technical support and are grateful to E. Kaxiras and J. Tersoff for helpful discussions. D. E. J. and W. X. T. acknowledge support by the Australian Research Council.

**REFERENCES**

- <sup>1</sup>R. D. Meade and D. Vanderbilt, Phys. Rev. Lett. **63**, 1404 (1989).
- <sup>2</sup>V. I. Marchenko and A. Y. Parshin, Sov. Phys. JETP **52**, 129 (1980).
- <sup>3</sup>A. Antons, R. Berger, K. Schroeder, and B. Voigtländer, Phys. Rev. B **73**, 125327 (2006).
- <sup>4</sup>O. L. Alerhand, J. Wang, J. D. Joannopoulos, and E. Kaxiras, J. Vac. Sci. Tech. B **9**, 2423 (1991).
- <sup>5</sup>S. Kodiyalam, K. E. Khor, N. C. Bartelt, E. D. Williams, and S. Das Sarma, Phys. Rev. B **51**, 5200 (1995).
- <sup>6</sup>R. M. Tromp, A. W. Denier van der Gon, and M. C. Reuter, Phys. Rev. Lett. **68**, 2313 (1992).
- <sup>7</sup>M. Copel, R. M. Tromp, and U. K. Köhler, Phys. Rev. B **37**, 10756 (1988).
- <sup>8</sup>R. S. Becker, B. S. Swartzentruber, J. S. Vickers, M. S. Hybertsen, and S. G. Louie, Phys. Rev. Lett. **60**, 116 (1988).
- <sup>9</sup>M. A. Olmstead, R. D. Bringans, R. I. G. Uhrberg, and R. Z. Bachrach, Phys. Rev. B **34**, 6041 (1986).
- <sup>10</sup>D. E. Jesson and W. X. Tang, *Surface Electron Microscopy of Ga Droplet Dynamics on GaAs (001)*, Vol. 3 (Formatex Research Center, Badajoz, Spain, 2010) pp. 1608–1619.
- <sup>11</sup>S. A. Nepijko, N. N. Sedov, and G. Schönhense, Journal of Microscopy **203**, 269 (2001).
- <sup>12</sup>S. M. Kennedy, C. X. Zheng, W. X. Tang, D. M. Paganin, and D. E. Jesson, Ultramicroscopy **111**, 356 (2011).
- <sup>13</sup>S. M. Kennedy, C. X. Zheng, W. X. Tang, D. M. Paganin, and D. E. Jesson, Proc. R. Soc. A **467**, 3332 (2011); *ibid.* **466**, 2857 (2010).
- <sup>14</sup>M. Zinke-Allmang, L. Feldman, J. Patel, and J. Tully, Surface Science **197**, 1 (1988).

<sup>15</sup>Y.-N. Yang and E. D. Williams, Phys. Rev. Lett. **72**, 1862 (1994).

<sup>16</sup>R. D. Twisten and J. M. Gibson, Phys. Rev. B **50**, 17628 (1994).

<sup>17</sup>B. Voigtländer, A. Zinner, T. Weber, and H. P. Bonzel, Phys. Rev. B **51**, 7583 (1995).

---

## Conclusions and future work

The central aim of this thesis has been to develop a method capable of imaging III-V MBE dynamics in real-time and specifically address the difficulties of imaging under high incident As flux. Further goals were to understand the imaging of 3D objects with a view to studying quantum structure formation and undertake proof-of-principle experiments, combining the advances in instrumentation and imaging.

We have developed and implemented a III-V low energy electron microscope (LEEM) which combines a commercially available LEEM system with In, Ga and As MBE sources and a specially designed cooling shroud to minimise the build up in background As pressure. The design also incorporates a hydrogen atom beam source for surface cleaning, magnetic shielding of the electron beam from MBE sources and an infrared pyrometer for surface temperature measurement.

Utilising Ga droplets and their trails as test-objects, a through focal MEM imaging series was used as the basis for the development of the Laplacian and caustic theories of mirror electron microscopy (MEM) imaging. The Laplacian theory is applicable to cases where surface topography is slowly varying and/or small microscope defocus. Under such circumstances, the image contrast can be interpreted in terms of the Laplacian of a blurred-surface height function which is intuitively linked to surface features. Caustic imaging theory can be used to interpret large variations in surface height, which are interpreted as caustics in the virtual image plane of the objective lens. Caustics are used to determine the droplet contact angle and the result is in excellent agreement with *ex situ* AFM measurements.

As a first application of III-V LEEM we imaged the stability of Ga droplets under As flux which provides a sensitive measure of  $T_c$ . This study showed how  $T_c$  can be directly controlled by As flux, elucidating its role during surface preparation and MBE growth. A second application imaged the coalescence dynamics of Ga-rich droplets during high temperature annealing. The droplets etch the GaAs substrate and represent a model reactive wetting system. The coalescence dynamics is observed to be highly asymmetric, involving the motion of one reactive droplet relative to the other, due to contact line pinning which is described by a simple geometrical model.

Finally, the high As flux capability of the III-V LEEM is used to study As adsorption on Si (111) at high temperature. This facilitated a reduction in As surface chemical potential to identify preferential regions of As incorporation in the vicinity of steps which is attributed to a reduction in surface stress associated with  $(1\times 1)$  As:Si(111) regions.

The development of III-V LEEM now creates wide ranging possibilities for future work in the III-V system. This includes the imaging of surface phase transformations on GaAs surfaces, investigations of surface diffusion and steps in the presence of As flux and mechanisms of homoepitaxy. This can be extended to the study of interface formation during heteroepitaxy, the formation of wetting layers and QDs during InAs growth on GaAs (001) and the basic mechanisms of droplet epitaxy.

---

## Bibliography

- Abbarchi M, Mastrandrea C A, Vinattieri A, Sanguinetti S, Mano T, Kuroda T, Koguchi N, Sakoda K and Gurioli M (2009). Photon antibunching in double quantum ring structures, *Phys. Rev. B* **79**, 085308.  
**URL:** <http://link.aps.org/doi/10.1103/PhysRevB.79.085308>
- Altman M and Bauer E (1996). LEEM/LEED investigation of reconstruction and initial oxidation of the W(001) surface, *Surface Science* **347**(3), 265–279.  
**URL:** <http://www.sciencedirect.com/science/article/pii/0039602895009817>
- Altman M S (2010). Trends in low energy electron microscopy, *Journal of Physics: Condensed Matter* **22**(8), 084017.  
**URL:** <http://stacks.iop.org/0953-8984/22/i=8/a=084017>
- Altman M S, Chung W F, He Z Q, Poon H C and Tong S Y (2001). Quantum size effect in low energy electron diffraction of thin films, *Applied Surface Science* **169-170**, 82–87.  
**URL:** <http://www.sciencedirect.com/science/article/pii/S0169433200006449>
- Altman M S, Chung W F and Liu C H (1998). LEEM Phase Contrast, *Surface Review and Letters* **05**(06), 1129–1141.  
**URL:** <http://www.worldscientific.com/doi/abs/10.1142/S0218625X98001468>
- Ambrose J, Nicholas M and Stoneham A (1992). Dynamics of braze spreading, *Acta Metallurgica et Materialia* **40**(10), 2483–2488.  
**URL:** <http://www.sciencedirect.com/science/article/pii/0956715192903178>
- Ambrose J, Nicholas M and Stoneham A (1993). Dynamics of liquid drop spreading in metal-metal systems, *Acta Metallurgica et Materialia* **41**(8), 2395–2401.  
**URL:** <http://www.sciencedirect.com/science/article/pii/095671519390319N>
- Apostolopoulos G, Herfort J, Däweritz L, Ploog K H and Luysberg M (2000). Reentrant Mound Formation in GaAs(001) Homoepitaxy Observed by *ex situ* Atomic Force Microscopy, *Phys. Rev. Lett.* **84**, 3358–3361.  
**URL:** <http://link.aps.org/doi/10.1103/PhysRevLett.84.3358>
- Arthur J R (1967). Vapor pressures and phase equilibria in the Ga-As system, *Journal of Physics and Chemistry of Solids* **28**(11), 2257 – 2267.  
**URL:** <http://www.sciencedirect.com/science/article/pii/002236976790251X>
- Arthur J R and LePore J J (1969). GaAs, GaP, and GaAs<sub>x</sub>P<sub>1-x</sub> Epitaxial Films Grown by Molecular Beam Deposition, *Journal of Vacuum Science and Technology* **6**(4), 545–548.  
**URL:** [http://avspublications.org/jvst/resource/1/jvst/v6/i4/p545\\_s1](http://avspublications.org/jvst/resource/1/jvst/v6/i4/p545_s1)
- Avery A R, Dobbs H T, Holmes D M, Joyce B A and Vvedensky D D (1997).

- Nucleation and Growth of Islands on GaAs Surfaces, *Phys. Rev. Lett.* **79**, 3938–3941.  
**URL:** <http://link.aps.org/doi/10.1103/PhysRevLett.79.3938>
- Bartelt N C, Tromp R M and Williams E D (1994). Step Capillary Waves and Equilibrium Island Shapes on Si(001), *Phys. Rev. Lett.* **73**, 1656–1659.  
**URL:** <http://link.aps.org/doi/10.1103/PhysRevLett.73.1656>
- Barth J V, Costantini G and Kern K (2005). Engineering atomic and molecular nanostructures at surfaces, *Nature* **437**(7059), 671–679.  
**URL:** <http://www.nature.com/nature/journal/v437/n7059/abs/nature04166.html>
- Bastiman F, Cullis A and Hopkinson M (2009). As-rich reconstruction stability observed by high temperature scanning tunnelling microscopy, *Journal of Crystal Growth* **311**(20), 4478 – 4482.  
**URL:** <http://www.sciencedirect.com/science/article/pii/S0022024809007799>
- Bauer E (1994). Low energy electron microscopy, *Reports on Progress in Physics* **57**(9), 895.  
**URL:** <http://iopscience.iop.org/0034-4885/57/9/002>
- Bauer E (1998). LEEM Basics, *Surface Review and Letters* **05**(06), 1275–1286.  
**URL:** <http://www.worldscientific.com/doi/abs/10.1142/S0218625X98001614>
- Bauer E (2007). LEEM and SPLEEM, in *Science of Microscopy*, P W Hawkes and J C H Spence, eds, Springer New York, pp. 605–656.
- Bayer M, Korkusinski M, Hawrylak P, Gutbrod T, Michel M and Forchel A (2003). Optical Detection of the Aharonov-Bohm Effect on a Charged Particle in a Nanoscale Quantum Ring, *Phys. Rev. Lett.* **90**, 186801.  
**URL:** <http://link.aps.org/doi/10.1103/PhysRevLett.90.186801>
- Becker R S, Swartzentruber B S, Vickers J S, Hybertsen M S and Louie S G (1988). Geometric and Local Electronic Structure of Si(111)-As, *Phys. Rev. Lett.* **60**, 116–119.  
**URL:** <http://link.aps.org/doi/10.1103/PhysRevLett.60.116>
- Biegelsen D K, Bringans R D, Northrup J E and Swartz L E (1990). Surface reconstructions of GaAs(100) observed by scanning tunneling microscopy, *Phys. Rev. B* **41**, 5701–5706.  
**URL:** <http://link.aps.org/doi/10.1103/PhysRevB.41.5701>
- Braun R J, Murray B T, Boettinger W J and McFadden G B (1995). Lubrication theory for reactive spreading of a thin drop, *Physics of Fluids* **7**(8), 1797–1810.  
**URL:** <http://link.aip.org/link/?PHF/7/1797/1>
- Chatain D and Carter W C (2004). Wetting dynamics: Spreading of metallic drops, *Nature Materials* **3**, 843–845.  
**URL:** <http://www.nature.com/nmat/journal/v3/n12/full/nmat1275.html>
- Chen Y and Washburn J (1996). Structural Transition in Large-Lattice-Mismatch Heteroepitaxy, *Phys. Rev. Lett.* **77**, 4046–4049.  
**URL:** <http://link.aps.org/doi/10.1103/PhysRevLett.77.4046>

- Cho A Y (1971). GaAs Epitaxy by a Molecular Beam Method: Observations of Surface Structure on the (001) Face, *Journal of Applied Physics* **42**(5), 2074–2081.  
**URL:** <http://dx.doi.org/10.1063/1.1660490>
- Cho A Y and Arthur J R (1975). Molecular beam epitaxy, *Progress in Solid State Chemistry* **10, Part 3**(0), 157 – 191.  
**URL:** <http://www.sciencedirect.com/science/article/pii/0079678675900059>
- Choquette K, Klem J, Fischer A, Blum O, Allerman A, Fritz I, Kurtz S, Breiland W, Sieg R, Geib K, Scott J and Naone R (2000). Room temperature continuous wave InGaAsN quantum well vertical-cavity lasers emitting at 1.3  $\mu\text{m}$ , *Electronics Letters* **36**(16), 1388–1390.  
**URL:** <http://dx.doi.org/10.1049/el:20000928>
- Chung W F and Altman M S (1998). Step contrast in low energy electron microscopy, *Ultramicroscopy* **74**(4), 237–246.  
**URL:** <http://www.sciencedirect.com/science/article/pii/S0304399198000436>
- Copel M, Tromp R M and Köhler U K (1988). Atomic structure of the arsenic-saturated Si(111) surface, *Phys. Rev. B* **37**, 10756–10763.  
**URL:** <http://link.aps.org/doi/10.1103/PhysRevB.37.10756>
- Davey J E and Pankey T (1968). Epitaxial GaAs Films Deposited by Vacuum Evaporation, *Journal of Applied Physics* **39**(4), 1941–1948.  
**URL:** <http://dx.doi.org/10.1063/1.1656467>
- Dupuy J, Sibai A and Vilotitch B (1984). Mirror Electron Microscopy (MEM): Work function and imaging of an electron beam biased junction of silicon (100), *Surface Science* **147**(1), 191 – 202.  
**URL:** <http://www.sciencedirect.com/science/article/pii/0039602884901754>
- Finley J J, Skalitz M, Arzberger M, Zrenner A, Böhm G and Abstreiter G (1998). Electrical detection of optically induced charge storage in self-assembled InAs quantum dots, *Applied Physics Letters* **73**(18), 2618–2620.  
**URL:** <http://link.aip.org/link/?APL/73/2618/1>
- Fomin V M, Gladilin V N, Klimin S N, Devreese J T, Kleemans N A J M and Koenraad P M (2007). Theory of electron energy spectrum and Aharonov-Bohm effect in self-assembled  $\text{In}_x\text{Ga}_{1-x}\text{As}$  quantum rings in GaAs, *Phys. Rev. B* **76**, 235320.  
**URL:** <http://link.aps.org/doi/10.1103/PhysRevB.76.235320>
- Foxon C T, Harvey J A and Joyce B A (1973). The evaporation of GaAs under equilibrium and non-equilibrium conditions using a modulated beam technique, *Journal of Physics and Chemistry of Solids* **34**(10), 1693–1701.  
**URL:** <http://www.sciencedirect.com/science/article/pii/S0022369773801350>
- Fuhrer A, Luscher S, Ihn T, Heinzl T, Ensslin K, Wegscheider W and Bichler M (2001). Energy spectra of quantum rings, *Nature* **413**, 822–825.  
**URL:** <http://www.nature.com/nature/journal/v413/n6858/full/413822a0.html>
- Gabaly F E, Puerta J M, Klein C, Saa A, Schmid A K, McCarty K F, Cerda J I and de la Figuera J (2007). Structure and morphology of ultrathin Co/Ru(0001) films,

- New Journal of Physics* **9**(3), 80.  
**URL:** <http://stacks.iop.org/1367-2630/9/i=3/a=080>
- Godehardt R (1995). Mirror Electron Microscopy, Vol. 94 of *Advances in Imaging and Electron Physics*, Elsevier, pp. 81 – 150.  
**URL:** <http://www.sciencedirect.com/science/article/pii/S1076567008701447>
- Goldstein B, Szostak D J and Ban V S (1976). Langmuir evaporation from the (100), (111A), and (111B) faces of GaAs, *Surface Science* **57**(2), 733 – 740.  
**URL:** <http://www.sciencedirect.com/science/article/pii/0039602876903587>
- Grundmann M, Christen J, Ledentsov N N, Böhrer J, Bimberg D, Ruvimov S S, Werner P, Richter U, Gösele U, Heydenreich J, Ustinov V M, Egorov A Y, Zhukov A E, Kopev P S and Alferov Z I (1995b). Ultranarrow Luminescence Lines from Single Quantum Dots, *Phys. Rev. Lett.* **74**, 4043–4046.  
**URL:** <http://link.aps.org/doi/10.1103/PhysRevLett.74.4043>
- Grundmann M, Stier O and Bimberg D (1995a). InAs/GaAs pyramidal quantum dots: Strain distribution, optical phonons, and electronic structure, *Phys. Rev. B* **52**, 11969–11981.  
**URL:** <http://link.aps.org/doi/10.1103/PhysRevB.52.11969>
- Hannon J B, Meyer zu Heringdorf F J, Tersoff J and Tromp R M (2001). Phase Coexistence during Surface Phase Transitions, *Phys. Rev. Lett.* **86**, 4871–4874.  
**URL:** <http://link.aps.org/doi/10.1103/PhysRevLett.86.4871>
- Hannon J B, Tersoff J and Tromp R M (2002). Surface Stress and Thermodynamic Nanoscale Size Selection, *Science* **295**(5553), 299–301.  
**URL:** <http://www.sciencemag.org/content/295/5553/299.abstract>
- Hannon J B and Tromp R M (2003). LOW-ENERGY ELECTRON MICROSCOPY OF SURFACE PHASE TRANSITIONS, *Annual Review of Materials Research* **33**(1), 263–288.  
**URL:** <http://www.annualreviews.org/doi/abs/10.1146/annurev.matsci.33.121901.111743>
- Hannon J B and Tromp R M (2008). Pit formation during graphene synthesis on SiC(0001): *In situ* electron microscopy, *Phys. Rev. B* **77**, 241404.  
**URL:** <http://link.aps.org/doi/10.1103/PhysRevB.77.241404>
- Heitz R, Ramachandran T R, Kalburge A, Xie Q, Mukhametzhanov I, Chen P and Madhukar A (1997). Observation of Reentrant 2D to 3D Morphology Transition in Highly Strained Epitaxy: InAs on GaAs, *Phys. Rev. Lett.* **78**, 4071–4074.  
**URL:** <http://link.aps.org/doi/10.1103/PhysRevLett.78.4071>
- Hermans A J and Petterson J A (1970). A quantum mechanical treatment of the mirror electron microscope, *Journal of Engineering Mathematics* **4**, 141–154.  
10.1007/BF01535086.  
**URL:** <http://dx.doi.org/10.1007/BF01535086>
- Hilner E, Zakharov A A, Schulte K, Kratzer P, Andersen J N, Lundgren E and Mikkelsen A (2009). Ordering of the Nanoscale Step Morphology As a Mechanism for Droplet Self-Propulsion, *Nano Letters* **9**(7), 2710–2714. PMID: 19507835.

- URL:** <http://pubs.acs.org/doi/abs/10.1021/nl9011886>
- Horio Y, Hashimoto Y and Ichimiya A (1996). A new type of RHEED apparatus equipped with an energy filter, *Applied Surface Science* **100-101**(0), 292–296.
- URL:** <http://www.sciencedirect.com/science/article/pii/0169433296002292>
- Hove J M V, Lent C S, Pukite P R and Cohen P I (1983). Damped oscillations in reflection high energy electron diffraction during GaAs MBE, *Journal of Vacuum Science & Technology B: Microelectronics and Nanometer Structures* **1**(3), 741–746.
- URL:** <http://link.aip.org/link/?JVb/1/741/1>
- Isomura N, Tsukamoto S, Iizuka K and Arakawa Y (2007). Investigation on GaAs(001) surface treated by As-free high temperature surface cleaning method, *Journal of Crystal Growth* **301-302**(0), 26–29.
- URL:** <http://www.sciencedirect.com/science/article/pii/S0022024806013868>
- Jesson D E, Munt T P and Lou C (2004). Critical Thickness for Nanostructure Self-Assembly During Stranski–Krastanow Growth, *Japanese Journal of Applied Physics* **43**(10), 7230–7231.
- URL:** <http://jjap.jsap.jp/link?JJAP/43/7230/>
- Joyce B A, Dobson P J, Neave J H, Woodbridge K, Zhang J, Larsen P K and B B (1986). RHEED studies of heterojunction and quantum well formation during MBE growth - from multiple scattering to band offsets, *Surface Science* **168**(1), 423–38.
- URL:** <http://www.sciencedirect.com/science/article/pii/0039602886908733>
- Joyce B A and Vvedensky D D (2004). Self-organized growth on GaAs surfaces, *Materials Science and Engineering: R: Reports* **46**(6), 127 – 176.
- URL:** <http://www.sciencedirect.com/science/article/pii/S0927796X04001147>
- Kennedy S M, Jesson D E, Morgan M J, Smith A E and Barker P F (2006). Phase sensitivity of slow electrons to interactions with weak potentials, *Phys. Rev. A* **74**, 044701.
- URL:** <http://link.aps.org/doi/10.1103/PhysRevA.74.044701>
- Kennedy S M, Jesson D E and Paganin D M (2011). Laplacian and caustic imaging theories of MEM work-function contrast, *IBM Journal of Research and Development* **55**(4), 3:1 –3:8.
- URL:** <http://dx.doi.org/10.1147/JRD.2011.2143310>
- Kennedy S M, Schofield N E, Paganin D M and Jesson D E (2009). Wave optical treatment of surface step contrast in low-energy electron microscopy, *Surface Review and Letters* **16**(06), 855–867.
- URL:** <http://www.worldscientific.com/doi/abs/10.1142/S0218625X09013402>
- Kirstaedter N, Ledentsov N, Grundmann M, Bimberg D, Ustinov V, Ruvimov S, Maximov M, Kop'ev P, Alferov Z, Richter U, Werner P, Gosele U and Heydenreich J (1994). Low threshold, large To injection laser emission from (InGa)As quantum dots, *Electronics Letters* **30**(17), 1416–1417.
- Kneedler E M, Jonker B T, Thibado P M, Wagner R J, Shanabrook B V and Whitman

- L J (1997). Influence of substrate surface reconstruction on the growth and magnetic properties of Fe on GaAs(001), *Phys. Rev. B* **56**, 8163–8168.  
**URL:** <http://link.aps.org/doi/10.1103/PhysRevB.56.8163>
- Kolodziej J J, Goryl M, Konior J, Reichling M and Szymonski M (2007). Direct real-space imaging of the  $c(2 \times 8)/(2 \times 4)$  GaAs (001) surface structure, *Phys. Rev. B* **76**, 245314.  
**URL:** <http://link.aps.org/doi/10.1103/PhysRevB.76.245314>
- Kolodziej J J, Such B, Szymonski M and Krok F (2003). Atomic Structure of InSb(001) and GaAs(001) Surfaces Imaged with Noncontact Atomic Force Microscopy, *Phys. Rev. Lett.* **90**, 226101.  
**URL:** <http://link.aps.org/doi/10.1103/PhysRevLett.90.226101>
- Kuan W H, Tang C S and Chang C H (2007). Spectral properties and magneto-optical excitations in semiconductor double rings under Rashba spin-orbit interaction, *Phys. Rev. B* **75**, 155326.  
**URL:** <http://link.aps.org/doi/10.1103/PhysRevB.75.155326>
- Kuroda T, Mano T, Ochiai T, Sanguinetti S, Sakoda K, Kido G and Koguchi N (2005). Optical transitions in quantum ring complexes, *Phys. Rev. B* **72**, 205301.  
**URL:** <http://link.aps.org/doi/10.1103/PhysRevB.72.205301>
- LaBella V P, Krause M R, Ding Z and Thibado P M (2005). Arsenic-rich GaAs(001) surface structure, *Surface Science Reports* **60**, 1 – 53.  
**URL:** <http://www.sciencedirect.com/science/article/pii/S016757290500049X>
- LaBella V P, Yang H, Bullock D W, Thibado P M, Kratzer P and Scheffler M (1999). Atomic Structure of the GaAs(001)-(2×4) Surface Resolved Using Scanning Tunneling Microscopy and First-Principles Theory, *Phys. Rev. Lett.* **83**, 2989–2992.  
**URL:** <http://link.aps.org/doi/10.1103/PhysRevLett.83.2989>
- Landin L, Miller M S, Pistol M E, Pryor C E and Samuelson L (1998). Optical Studies of Individual InAs Quantum Dots in GaAs: Few-Particle Effects, *Science* **280**(5361), 262–264.  
**URL:** <http://www.sciencemag.org/content/280/5361/262.abstract>
- Ledentsov N N, Shchukin V A, Grundmann M, Kirstaedter N, Böhrer J, Schmidt O, Bimberg D, Ustinov V M, Egorov A Y, Zhukov A E, Kop'ev P S, Zaitsev S V, Gordeev N Y, Alferov Z I, Borovkov A I, Kosogov A O, Ruvimov S S, Werner P, Gösele U and Heydenreich J (1996). Direct formation of vertically coupled quantum dots in Stranski-Krastanow growth, *Phys. Rev. B* **54**, 8743–8750.  
**URL:** <http://link.aps.org/doi/10.1103/PhysRevB.54.8743>
- Lee J H, Wang Z M, AbuWaar Z Y and Salamo G J (2009). Design of Nanostructure Complexes by Droplet Epitaxy, *Crystal Growth & Design* **9**(2), 715–721.  
**URL:** <http://pubs.acs.org/doi/abs/10.1021/cg701142d>
- Leonard D, Krishnamurthy M, Reaves C M, Denbaars S P and Petroff P M (1993). Direct formation of quantum-sized dots from uniform coherent islands of InGaAs on GaAs surfaces, *Applied Physics Letters* **63**(23), 3203–3205.

- URL:** <http://link.aip.org/link/?APL/63/3203/1>
- Liu G, Stintz A, Li H, Malloy K and Lester L (1999). Extremely low room-temperature threshold current density diode lasers using InAs dots in  $In_{0.15}Ga_{0.85}As$  quantum well, *Electronics Letters* **35**(14), 1163–1165.
- URL:** [http://ieeexplore.ieee.org/xpls/abs\\_all.jsp?arnumber=788943](http://ieeexplore.ieee.org/xpls/abs_all.jsp?arnumber=788943)
- Loss D and DiVincenzo D P (1998). Quantum computation with quantum dots, *Phys. Rev. A* **57**, 120–126.
- URL:** <http://link.aps.org/doi/10.1103/PhysRevA.57.120>
- Lowes T D and Zinke-Allmang M (1993). Microscopic study of cluster formation in the Ga on GaAs(001) system, *Journal of Applied Physics* **73**(10), 4937–4941.
- URL:** <http://link.aip.org/link/?JAP/73/4937/1>
- Lucignano P, Giuliano D and Tagliacozzo A (2007). Quantum rings with Rashba spin-orbit coupling: A path-integral approach, *Phys. Rev. B* **76**, 045324.
- URL:** <http://link.aps.org/doi/10.1103/PhysRevB.76.045324>
- Luk'yanov A E, Spivak G V and Gvozdover R S (1974). Mirror electron microscopy, *Soviet Physics Uspekhi* **16**(4), 529.
- URL:** <http://stacks.iop.org/0038-5670/16/i=4/a=R06>
- Mano T, Kuroda T, Sanguinetti S, Ochiai T, Tateno T, Kim J, Noda T, Kawabe M, Sakoda K, Kido G and Koguchi N (2005). Self-Assembly of Concentric Quantum Double Rings, *Nano Letters* **5**(3), 425–428.
- URL:** <http://pubs.acs.org/doi/abs/10.1021/nl048192%2B>
- Márquez J, Geelhaar L and Jacobi K (2001). Atomically resolved structure of InAs quantum dots, *Applied Physics Letters* **78**(16), 2309–2311.
- URL:** <http://link.aip.org/link/?APL/78/2309/1>
- Marzin J Y, Gérard J M, Izraël A, Barrier D and Bastard G (1994). Photoluminescence of Single InAs Quantum Dots Obtained by Self-Organized Growth on GaAs, *Phys. Rev. Lett.* **73**, 716–719.
- URL:** <http://link.aps.org/doi/10.1103/PhysRevLett.73.716>
- McCarty K and Bartelt N (2003). The  $1\times 1/1\times 2$  phase transition of the  $TiO_2(110)$  surface-variation of transition temperature with crystal composition, *Surface Science* **527**, L203 – L212.
- URL:** <http://www.sciencedirect.com/science/article/pii/S0039602803000037>
- McCarty K F, Nobel J A and Bartelt N C (2001). Vacancies in solids and the stability of surface morphology, *Nature* **412**, 622–625.
- URL:** <http://www.nature.com/nature/journal/v412/n6847/full/412622a0.html>
- Miller D A B, Chemla D S, Damen T C, Gossard A C, Wiegmann W, Wood T H and Burrus C A (1984). Band-Edge Electroabsorption in Quantum Well Structures: The Quantum-Confined Stark Effect, *Phys. Rev. Lett.* **53**, 2173–2176.
- URL:** <http://link.aps.org/doi/10.1103/PhysRevLett.53.2173>
- Moison J M, Houzay F, Barthe F, Leprince L, André E and Vatel O (1994). Self-organized growth of regular nanometer-scale InAs dots on GaAs, *Applied Physics*

- Letters* **64**(2), 196–198.  
**URL:** <http://link.aip.org/link/?APL/64/196/1>
- Mundschau M, Bauer E, Teliyps W and Swiech W (1989). In situ studies of epitaxial growth in the low energy electron microscope, *Surface Science* **213**(2-3), 381.  
**URL:** <http://www.sciencedirect.com/science/article/pii/0039602889902987>
- Mutaftschiev B (2001). *The Atomistic Nature of Crystal Growth*, Springer.
- Narhe R, Beysens D and Nikolayev V S (2004). Contact Line Dynamics in Drop Coalescence and Spreading, *Langmuir* **20**(4), 1213–1221. PMID: 15803699.  
**URL:** <http://pubs.acs.org/doi/abs/10.1021/la034991g>
- Neave J H, Joyce B A, Dobson P J and Norton N (1983). Dynamics of film growth of GaAs by MBE from Rheed observations, *Applied Physics A: Materials Science & Processing* **31**, 1–8. 10.1007/BF00617180.  
**URL:** <http://dx.doi.org/10.1007/BF00617180>
- Nepijko S A and Schönhense G (2010). Measurement of potential distribution function on object surface by using an electron microscope in the mirror operation mode, *Journal of Microscopy* **238**(1), 90–94.  
**URL:** <http://dx.doi.org/10.1111/j.1365-2818.2009.03340.x>
- Nepijko S A, Sedov N N and Schönhense G (2001a). Peculiarities of imaging one- and two-dimensional structures using an electron microscope in the mirror operation mode, *Journal of Microscopy* **203**(3), 269–276.  
**URL:** <http://dx.doi.org/10.1046/j.1365-2818.2001.00895.x>
- Nepijko S and Sedov N (1997). Aspects of Mirror Electron Microscopy, Vol. 102 of *Advances in Imaging and Electron Physics*, Elsevier, pp. 273 – 323.  
**URL:** <http://www.sciencedirect.com/science/article/pii/S1076567008701253>
- Ohtake A (2008). Surface reconstructions on GaAs(001), *Surface Science Reports* **63**(7), 295 – 327.  
**URL:** <http://www.sciencedirect.com/science/article/pii/S0167572908000198>
- Ohtake A, Nakamura J, Tsukamoto S, Koguchi N and Natori A (2002). New Structure Model for the GaAs(001)c(4×4) Surface, *Phys. Rev. Lett.* **89**, 206102.  
**URL:** <http://link.aps.org/doi/10.1103/PhysRevLett.89.206102>
- Olmstead M A, Bringans R D, Uhrberg R I G and Bachrach R Z (1986). Arsenic overlayer on Si(111): Removal of surface reconstruction, *Phys. Rev. B* **34**, 6041–6044.  
**URL:** <http://link.aps.org/doi/10.1103/PhysRevB.34.6041>
- Ondrejcek M, Rajappan M, Swiech W and Flynn C (2005b). Step fluctuation spectroscopy of Au(111) by LEEM, *Surface Science* **574**(2-3), 111–122.  
**URL:** <http://www.sciencedirect.com/science/article/pii/S0039602804013603>
- Ondrejcek M, Swiech W, Rajappan M and Flynn C P (2005a). Fluctuation spectroscopy of step edges on Pt(111) and Pd(111), *Phys. Rev. B* **72**, 085422.  
**URL:** <http://link.aps.org/doi/10.1103/PhysRevB.72.085422>
- Pashley M D, Haberern K W, Friday W, Woodall J M and Kirchner P D (1988).

- Structure of GaAs(001) ( $2 \times 4$ ) –  $c(2 \times 8)$  Determined by Scanning Tunneling Microscopy, *Phys. Rev. Lett.* **60**, 2176–2179.  
**URL:** <http://link.aps.org/doi/10.1103/PhysRevLett.60.2176>
- Pelhos K, Madey T E, Hannon J B and Kellogg G L (1999). Nucleation and growth during faceting of the platinum-covered W(111) surface, *Surface Review and Letters* **06**(05), 767–774.  
**URL:** <http://www.worldscientific.com/doi/abs/10.1142/S0218625X99000779>
- Phaneuf R J, Hong Y, Horch S and Bennett P A (1997). Two Dimensional Phase Separation for Co Adsorbed on Si(111), *Phys. Rev. Lett.* **78**, 4605–4608.  
**URL:** <http://link.aps.org/doi/10.1103/PhysRevLett.78.4605>
- Phaneuf R J and Schmid A K (2003). Low-Energy Electron Microscopy: Imaging Surface Dynamics, *Physics Today* **56**(3), 50–55.  
**URL:** <http://link.aip.org/link/?PTO/56/50/1>
- Plass R, Last J A, Bartelt N C and Kellogg G L (2001). Nanostructures: Self-assembled domain patterns, *Nature* **412**, 875–876.  
**URL:** <http://www.nature.com/nature/journal/v412/n6850/full/412875a0>
- Priester C and Lannoo M (1995). Origin of Self-Assembled Quantum Dots in Highly Mismatched Heteroepitaxy, *Phys. Rev. Lett.* **75**, 93–96.  
**URL:** <http://link.aps.org/doi/10.1103/PhysRevLett.75.93>
- Rempfer G F and Griffith O H (1992). Emission microscopy and related techniques: Resolution in photoelectron microscopy, low energy electron microscopy and mirror electron microscopy, *Ultramicroscopy* **47**(1-3), 35–54.  
**URL:** <http://www.sciencedirect.com/science/article/pii/030439919290184L>
- Ross F M, Tromp R M and Reuter M C (1999). Transition States Between Pyramids and Domes During Ge/Si Island Growth, *Science* **286**(5446), 1931–1934.  
**URL:** <http://www.sciencemag.org/content/286/5446/1931.abstract>
- Schmidt T, Flege J I, Gangopadhyay S, Clausen T, Locatelli A, Heun S and Falta J (2007). Alignment of Ge Nanoislands on Si(111) by Ga-Induced Substrate Self-Patterning, *Phys. Rev. Lett.* **98**, 066104.  
**URL:** <http://link.aps.org/doi/10.1103/PhysRevLett.98.066104>
- Schmidt T, Schaak A and G S (2000). In situ imaging of structural changes in a chemical wave with low-energy electron microscopy: the system Rh(110)/NO+H<sub>2</sub>, *Chemical Physics Letters* **318**(6), 549–554.  
**URL:** <http://www.sciencedirect.com/science/article/pii/S0009261400000610>
- Shchukin V A and Bimberg D (1999). Spontaneous ordering of nanostructures on crystal surfaces, *Rev. Mod. Phys.* **71**, 1125–1171.  
**URL:** <http://link.aps.org/doi/10.1103/RevModPhys.71.1125>
- Smith G W, Pidduck A J, Whitehouse C R, Glasper J L, Keir A M and Pickering C (1991). Surface topography changes during the growth of GaAs by molecular beam epitaxy, *Applied Physics Letters* **59**(25), 3282–3284.  
**URL:** <http://link.aip.org/link/?APL/59/3282/1>

- Solomon G S, Trezza J A, Marshall A F and Harris, Jr. J S (1996). Vertically Aligned and Electronically Coupled Growth Induced InAs Islands in GaAs, *Phys. Rev. Lett.* **76**, 952–955.  
**URL:** <http://link.aps.org/doi/10.1103/PhysRevLett.76.952>
- Somaschini C, Bietti S, Koguchi N and Sanguinetti S (2009). Fabrication of Multiple Concentric Nanoring Structures, *Nano Letters* **9**(10), 3419–3424.  
**URL:** <http://pubs.acs.org/doi/abs/10.1021/nl901493f>
- Somaschini C, Bietti S, Koguchi N and Sanguinetti S (2011a). Coupled quantum dot-ring structures by droplet epitaxy, *Nanotechnology* **22**(18), 185602.  
**URL:** <http://stacks.iop.org/0957-4484/22/i=18/a=185602>
- Somaschini C, Bietti S, Koguchi N and Sanguinetti S (2011b). Outer zone morphology in GaAs ring/disk nanostructures by droplet epitaxy, *Journal of Crystal Growth* **323**(1), 279 – 281.  
**URL:** <http://www.sciencedirect.com/science/article/pii/S0022024810008791>
- Someya T and Kobayashi J (1974). Quantitative application of electron-mirror microscopy to the determination of pure shear of ferroelectric Gd<sub>2</sub>(MoO<sub>4</sub>)<sub>3</sub>, *physica status solidi (a)* **26**(1), 325–336.  
**URL:** <http://dx.doi.org/10.1002/pssa.2210260134>
- Stroscio J A, Pierce D T and Dragoset R A (1993). Homoepitaxial growth of iron and a real space view of reflection-high-energy-electron diffraction, *Phys. Rev. Lett.* **70**, 3615–3618.  
**URL:** <http://link.aps.org/doi/10.1103/PhysRevLett.70.3615>
- Sugaya T and Kawabe M (1991). Low-Temperature Cleaning of GaAs Substrate by Atomic Hydrogen Irradiation, *Japanese Journal of Applied Physics* **30**(Part 2, No. 3A), L402–L404.  
**URL:** <http://jjap.jsap.jp/link?JJAP/30/L402/>
- Sutter P W, Flege J I and Sutter E A (2008). Epitaxial graphene on ruthenium, *Nature materials* **7**(5), 406–411.  
**URL:** <http://www.nature.com/nmat/journal/v7/n5/full/nmat2166.html>
- Tang W X, Man K L, Huang H, Woo C H and Altman M S (2002). Growth shapes of Ag crystallites on the Si(111) surface, *Papers from the 3rd LEEM/PEEM Workshop* **20**(6), 2492–2495.  
**URL:** <http://link.aip.org/link?JVB/20/2492/1>
- Telieps W and Bauer E (1985). The (7×7)-(1×1) phase transition on Si(111), *Surface Science* **162**, 163 – 168.
- Tersoff J, Jesson D E and Tang W X (2009). Running Droplets of Gallium from Evaporation of Gallium Arsenide, *Science* **324**(5924), 236–238.  
**URL:** <http://www.sciencemag.org/content/324/5924/236.abstract>
- Tersoff J, Jesson D E and Tang W X (2010). Decomposition Controlled by Surface Morphology during Langmuir Evaporation of GaAs, *Phys. Rev. Lett.* **105**, 035702.  
**URL:** <http://link.aps.org/doi/10.1103/PhysRevLett.105.035702>

- Tersoff J, Johnson M D and Orr B G (1997). Adatom Densities on GaAs: Evidence for Near-Equilibrium Growth, *Phys. Rev. Lett.* **78**, 282–285.  
**URL:** <http://link.aps.org/doi/10.1103/PhysRevLett.78.282>
- Tersoff J, Teichert C and Lagally M G (1996). Self-Organization in Growth of Quantum Dot Superlattices, *Phys. Rev. Lett.* **76**, 1675–1678.  
**URL:** <http://link.aps.org/doi/10.1103/PhysRevLett.76.1675>
- Theis W, Bartelt N C and Tromp R M (1995). Chemical Potential Maps and Spatial Correlations in 2D-Island Ripening on Si(001), *Phys. Rev. Lett.* **75**, 3328–3331.  
**URL:** <http://link.aps.org/doi/10.1103/PhysRevLett.75.3328>
- Tromp R M and Hannon J B (2002). Thermodynamics of Nucleation and Growth, *Surface Review and Letters* **9**, 1565–1593.  
**URL:** <http://www.worldscientific.com/doi/abs/10.1142/S0218625X02003846>
- Tromp R M and Mankos M (1998). Thermal Adatoms on Si(001), *Phys. Rev. Lett.* **81**, 1050–1053.  
**URL:** <http://link.aps.org/doi/10.1103/PhysRevLett.81.1050>
- Tromp R M and Reuter M C (1992). Local dimer exchange in surfactant-mediated epitaxial growth, *Phys. Rev. Lett.* **68**, 954–957.  
**URL:** <http://link.aps.org/doi/10.1103/PhysRevLett.68.954>
- Tsao J Y (1993). *Materials Fundamentals of Molecular Beam Epitaxy*, Academic.
- Tschersich K G, Fleischhauer J P and Schuler H (2008). Design and characterization of a thermal hydrogen atom source, *Journal of Applied Physics* **104**(3), 034908.  
**URL:** <http://link.aip.org/link/?JAP/104/034908/1>
- Tu Y and Tersoff J (2004). Origin of Apparent Critical Thickness for Island Formation in Heteroepitaxy, *Phys. Rev. Lett.* **93**, 216101.  
**URL:** <http://link.aps.org/doi/10.1103/PhysRevLett.93.216101>
- Voigtländer B (2001). Fundamental processes in Si/Si and Ge/Si epitaxy studied by scanning tunneling microscopy during growth, *Surface Science Reports* **43**(5), 127–254.  
**URL:** <http://www.sciencedirect.com/science/article/pii/S0167572901000127>
- Wang Z, Holmes K, Mazur Y, Ramsey K and Salamo G (2006). Self-organization of quantum-dot pairs by high-temperature droplet epitaxy, *Nanoscale Research Letters* **1**, 57–61. 10.1007/s11671-006-9002-z.  
**URL:** <http://dx.doi.org/10.1007/s11671-006-9002-z>
- Wang Z M, Liang B L, Sablon K A and Salamo G J (2007). Nanoholes fabricated by self-assembled gallium nanodrill on GaAs(100), *Applied Physics Letters* **90**(11), 113120.  
**URL:** <http://link.aip.org/link/?APL/90/113120/1>
- Warren J, Boettinger W and Roosen A (1998). Modeling reactive wetting, *Acta Materialia* **46**(9), 3247–3264.  
**URL:** <http://www.sciencedirect.com/science/article/pii/S1359645497004874>
- Watanabe K, Koguchi N and Gotoh Y (2000). Fabrication of GaAs Quantum Dots

- by Modified Droplet Epitaxy, *Japanese Journal of Applied Physics* **39**(Part 2, No. 2A), L79–L81.  
**URL:** <http://jjap.jsap.jp/link?JJAP/39/L79/>
- Xie Q, Madhukar A, Chen P and Kobayashi N P (1995). Vertically Self-Organized InAs Quantum Box Islands on GaAs(100), *Phys. Rev. Lett.* **75**, 2542–2545.  
**URL:** <http://link.aps.org/doi/10.1103/PhysRevLett.75.2542>
- Xue Q K, Hashizume T and Sakurai T (1997). Scanning tunneling microscopy of III-V compound semiconductor (001) surfaces, *Progress in Surface Science* **56**, 1–131.  
**URL:** <http://www.sciencedirect.com/science/article/pii/S0079681697000336>
- Xue Q K, Hashizume T, Zhou J M, Sakata T, Ohno T and Sakurai T (1995). Structures of the Ga-Rich  $4\times 2$  and  $4\times 6$  Reconstructions of the GaAs(001) Surface, *Phys. Rev. Lett.* **74**, 3177h–3180.  
**URL:** <http://link.aps.org/doi/10.1103/PhysRevLett.74.3177>
- Yamaguchi K, Yujobo K and Kaizu T (2000). Stranski-Krastanov Growth of InAs Quantum Dots with Narrow Size Distribution, *Japanese Journal of Applied Physics* **39**(Part 2, No. 12A), L1245–L1248.  
**URL:** <http://jjap.jsap.jp/link?JJAP/39/L1245/>
- Zinke-Allmang M, Feldman L C and van Saarloos W (1992). Experimental study of self-similarity in the coalescence growth regime, *Phys. Rev. Lett.* **68**, 2358–2361.  
**URL:** <http://link.aps.org/doi/10.1103/PhysRevLett.68.2358>
- Zinke-Allmang M, Feldman L, Patel J and Tully J (1988). The morphology of As terminated Si(111) from desorption kinetics, *Surface Science* **197**(1-2), 1–10.  
**URL:** <http://www.sciencedirect.com/science/article/pii/0039602888905687>